Crustal transect from the Knipovich Ridge to Bear Island across the western Barents Sea margin

Christian Haug Eide

Master Thesis

Department of Earth Science

University of Bergen

June 2010

Abstract

A crustal model of a 322 km long transect from the Knipovich Ridge to Bear Island (Bjørnøya) has been obtained by use of reflection seismic data and wide angle Ocean Bottom Seismometer (OBS) data. Further constraints of the model have been provided by gravity modeling. The study is part of the IPY (International Polar Year) consortium "Plate Tectonics and Polar Gateways in Earth History". The primary objective is to gain detailed insights into the structure of oceanic crust created by the slow to ultraslow spreading Knipovich Ridge. A secondary objective is to investigate the southern part of the sheared Hornsund margin segment of the Western Barents Sea. The thickness of oceanic crust varies greatly along the profile, from 4 to 8 km. The youngest part of the oceanic crustal layer 2 is dominated by relatively low p-wave velocities of 4.4 km/s, while the older parts with a thicker sedimentary overburden have velocities varying from 5.2 to 6.2 km/s. These variations appear to be correlated to variations in the total crustal thickness. The continent ocean boundary (COB) has been located to a 15 km wide zone, and a new location of the COB is proposed for the area around the line. East of the COB, a downfaulted terrace is identified between the Hornsund Fault Zone and the Knølegga Fault. The Knipovich Escarpment is a prominent feature on this profile, marking a 3 km rise in the oceanic basement over 20 km. It is associated with a shallowing of the Moho, and is interpreted to mark the location of a detachment fault which developed around 10 Ma or later.

Acknowledgements

First of all, I would like to thank my supervisor, Professor Rolf Mjelde, for an interesting project, good supervision, and helpful input. I would also like to thank Audun Libak for teaching me how to use the programs, for valuable discussions and for the countless hours he spent helping me. I am also grateful to Bent Ole Ruud for processing the multi channel seismic data, Arne Gidskehaug for processing the gravity data, and Berit Oline Hjelstuen for tips regarding the sedimentology on the Barents Sea margin.

Thanks to my fellow students and to my friends for making these five years so memorable. Thank you for the lunches, the stressful days before exams, the parties after the exams, the field trips, and all the other moments we shared.

I would also like to express my gratitude for my family for supporting me all these years.

Finally, to Heidi; your support, encouragement and patience during this time have meant the world to me.

_____

Christian Haug Eide

Bergen, June 2010

Table of Contents

1 Introduction

The study area of this thesis is the Norwegian-Greenland Sea and the Western Barents Sea margin (Figure 1.1). This area has been the subject of several studies the last decades. However, the magnetic anomalies of the oceanic crust are diffuse and difficult to identify, and the spreading history of the ridge is therefore poorly understood. Suggestions for the spreading history has ranged from strongly asymmetric spreading (Crane 1991), a ridge jump (Sundvor and Eldholm, 1979; Eldholm et al., 1990), or continuous, symmetric spreading on the same ridge with minor adjustments (Engen et al., 2008).

In order to understand the spreading history in absence of magnetic anomalies, studies of the crustal structure and composition using refraction seismic methods with ocean bottom seismometers (OBS) are perhaps the best way to gain more knowledge. Only a few OBS studies have been conducted in this area to this date (Breivik and Mjelde, 2001; Ritzmann et al., 2002; Breivik et al., 2003; Ljones et al., 2004; Kandilarov et al., 2008; Czuba et al., 2010). This thesis presents the results from an OBS refraction experiment conducted in 2008, complemented by gravity measurements performed simultaneously to the refraction experiment and a multi channel data (MCS) line collected in 2006 (Figure 1.1). The OBS spacing in this experiment is 16 km, making this the closest spaced OBS line in the area to date.

The main purpose of this thesis is to construct a crustal scale P-wave velocity and density model for the area covered by this line, and interpret the model in order to better understand the geology of the area. Using this model, the geolocial evolution of the area, the nature of the Knipovich Escarpment and the location of the continent-ocean boundary (COB) at the Barents Sea margin will be discussed.
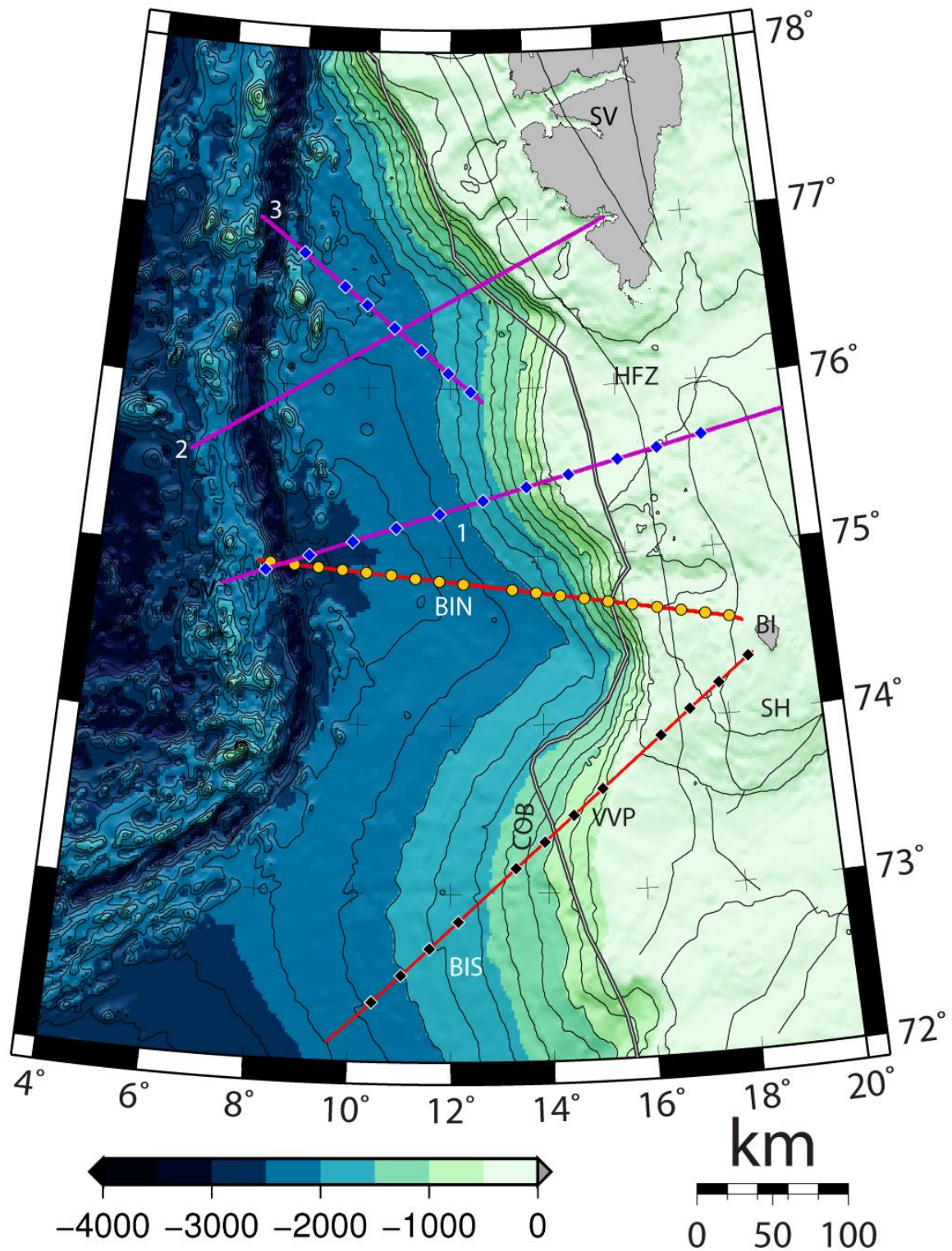
**Figure 1.1:** Map of the study area with nearby OBS survey lines. 1, Breivik and Mjelde (2001) and Breivik et al. (2003); 2, Ljones et al. (2004); 3, Kandilarov et al. (2008); BI, Bear Island; BIN, Bear Island North profile - this thesis; BIS, Bear Island South profile - Czuba et al. (2010); COB, Continent-Ocean Boundary; HFZ, Hornsund Fracture Zone; SH, Stappen High; SV, Svalbard, VVP, Vestbakken Volcanic Province.

2. Geological Background

2.1. Spreading ridges

Spreading ridges are constructive plate boundaries where new oceanic crust is generated. The crests of ocean ridges are commonly 2-3 km shallower than their nearby ocean basins (Keary and Vine, 1996). The morphology of spreading ridges appear to be controlled by spreading rate (Macdonald, 1982). Macdonald (1982) recognized three categories of ocean ridges; slow spreading, intermediate spreading and fast spreading (Figure 2.1).
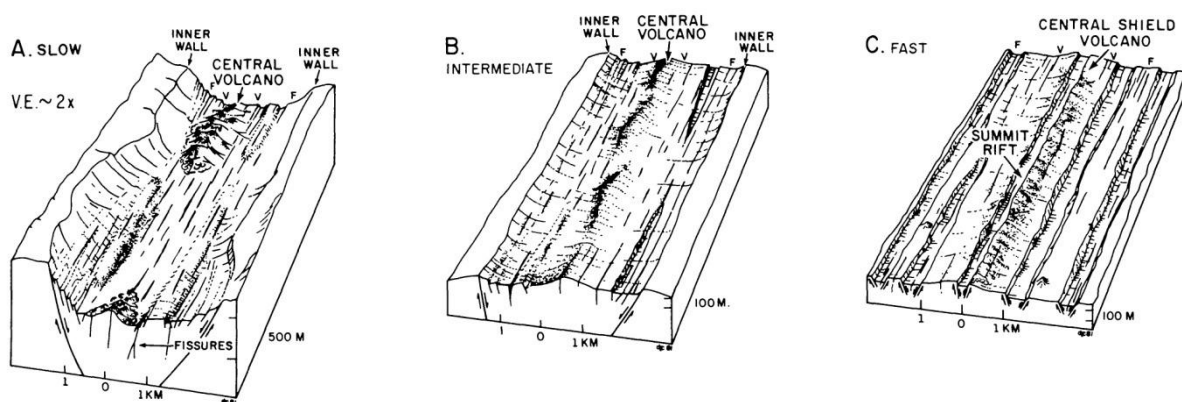
Figure 2.1: Schematic illustrations of the axial zone of mid-ocean ridges at different spreading rates. Note the highly discontinuous volcanic zone in A, the moderately continuous volcanic zone in B, and very continuous volcanic zone in C (MacDonald, 1982).

The slow spreading ridges, such as the Mid-Atlantic and Atlantic-Indian ridges, are characterized by a spreading rate of 10-50 mm/a, rugged topography and a prominent median rift 30-50 km wide and 1.5-3 km deep. Ridges spreading at intermediate rates of 50-90 mm/a, such as the most northerly East Pacific Rise, have a median valley only 50-200 m deep, and a relatively smooth topography. Ridges spreading at fast rates, faster than 90 mm/a , such as the East Pacific Rise, have a smooth topography and no median valley, resembling Hawaiian shield volcanoes (Macdonald, 1982).

These three classes of oceanic ridges show a hierarchy of segmentation, from large, long lived segments to smaller, more transitory segments (Macdonald et al, 1991). The first order segmentation is marked by rigid plate transform faults, offsetting the ridge axis from tens to hundreds of kilometers. These transform faults commonly continue as oceanic fracture zones, parallel to the spreading direction. The higher order segments occur between the transform faults.

3

Dick et al. (2004) also described a fourth type of oceanic ridge, the ultra slow class of spreading ridges, based on studies of the Southwest Indian and Arctic ridges. Ultra slow spreading ridges form at spreading rates less than 12 mm/a, but their characteristics are commonly found at ridges with rates up to 20 mm/a. Ultra slow spreading ridges are characterized by intermittent volcanism, lack of transform faults and often have linked magmatic and amagmatic segments. The magmatic segments form sub-perpendicular to the least principal compressive stress, and take the shape of linear axial highs or troughs. Amagmatic, or tectonic, segments are formed in any direction relative to the spreading direction, and are marked by linear troughs often less than 1 km deep which may extend to over 50 km. They have only scattered volcanics, virtually no oceanic layer 3, often expose mantle peridotite, and have weak magnetic anomalies. The primary unit of accretion seem to be mantle horst blocks rising up through the rift valley floor.

2.2. Oceanic crust

Oceanic crust is created at mid-oceanic ridges by solidifying of upwelling magma in a narrow zone. The large scale structure of oceanic crust has primarily investigated by seismic refraction- and reflection profiling, but results from drilling, dredging and studies of ophiolites have also provided important insights (Fowler, 1990). It can be divided into three main layers, with further possible subdivision (figure 2.2).
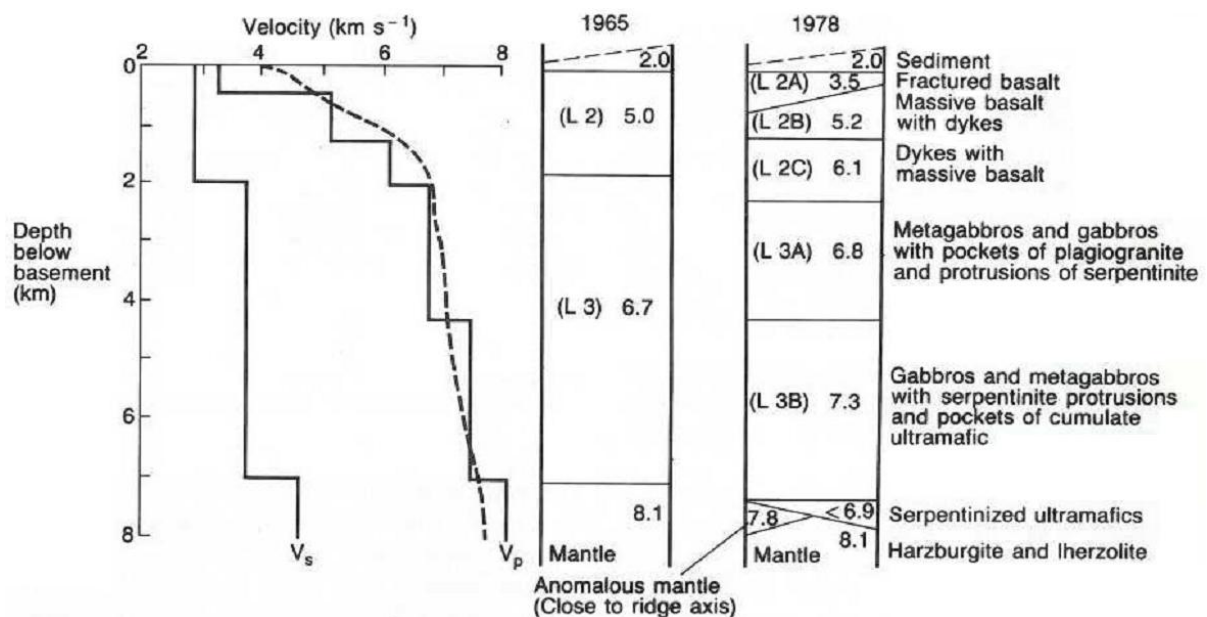
Figure 2.2: P- and S-wave velocity structure of the oceanic crust, and interpretations presented in 1965 and 1978. Numbers refer to acoustic velocity in km/s. The stippled line is a gradational velocity model deduced by more sophisticated measurements (Spudich and Orcutt, 1980; Harrison and Bonatti, 1981; Kearey and Vine, 1996).

Oceanic layer 1 consists of sediments, and is on average 0.4 km thick. Sedimentary cover progressively thickens as distance to the ridge increases, since older crust have more time to accumulate sediments. The velocity at the top of the layer is generally close to 1.5 km/s, but increase downwards as the sediments consolidate (Fowler, 1990).

Oceanic layer 2 is composed of basalt, and the interface between oceanic layers 1 and 2 marks the top oceanic basement. It has a variable thickness of 1-2.5 km and seismic velocities of 3.4-6.2 km/s (Keary and Vine, 1996). A subdivision into layers 2A, 2B and 2C have been proposed, but oceanic layer 2 is probably best described as a region of oceanic crust where velocity is rapidly increasing with depth (Fowler, 1990). Drilling has shown the oceanic layer 2 to be composed of extrusive pillow lavas in the upper part, more consolidated basalt further down, and sheeted dykes near the base, grading into oceanic layer 3 (Fowler, 1990). The velocity of oceanic layer 2 may increase with time, due to infilling of pores and cracks by infilling of secondary minerals (Jacobson, 1992).

Oceanic layer 3 makes up the majority of oceanic crust, with an average thickness of 5 km. Typical P-wave velocities are 6.5 -7.2 km/s, with gradients of 0.1-0.2 s^{-1} (Fowler, 1990). Layer 3 is thought to consist of gabbro formed by crystallization of magma in a magma chamber. Hess (1962) proposed that oceanic layer 3 forms by serpentinization, a process where olivine in mantle material react with water to produce serpentinized peridote, and therefore consists of peridote. S-wave studies performed in the 1970's showed that the Poisson's ratio of oceanic layer 3 is more in accord with a gabbroic composition (Keary and Vine, 1996). However, it is possible that serpentinized upper mantle may occur in areas with very thin crust, such as near oceanic fracture zones and/or at crust formed at very slow spreading ridges (Fowler 1990).

Away from anomalous zones in the oceanic crust, such as fracture zones and areas near hot spots, the oceanic crust has an average thickness of 7.1±0.8 km (White et al., 1994). It was noted by Reid and Jackson (1981) that the thickness of oceanic crust is not influenced by spreading rate as long as the spreading rate is greater than 20 mm/a. At lower spreading rates, the oceanic crust generated is significantly thinner than at higher rates. This effect is attributed to conductive heat loss allowing the mantle to cool as it rises, thereby decreasing melt production.

2.3. Evolution of the Norwegian-Greenland Sea

The Norwegian-Greenland Sea is the ocean between Europe and Greenland, constrained to the south by the Greenland-Iceland-Faeroe ridge, and by the Spitsbergen Fracture Zone to the north (Eldholm et al., 1990). Important structural elements are the Kolbeinsey Ridge, the now extinct Aegir Ridge, the obliquely spreading Mohns Ridge, the Knipovich Ridge, the Molloy Ridge and the Jan Mayen Fracture Zone linking the Kolbeinsey Ridge and the Mohns ridge (Talwani and Eldholm, 1977). This ridge system forms the Arctic Ridge system together with the Gakkel Ridge, and forms the boundary between the North American and Eurasian plates (Figure 2.3).
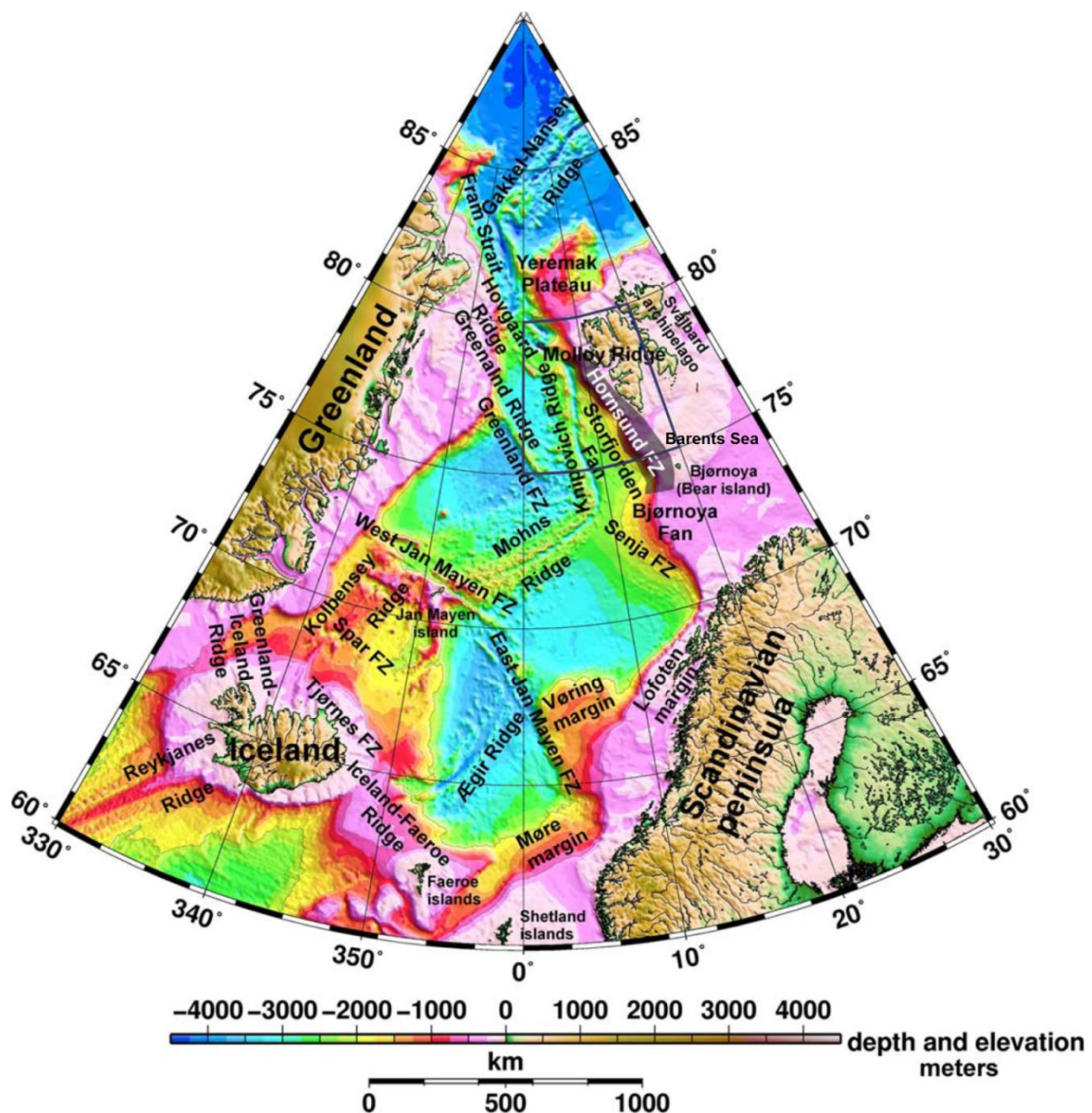

Figure 2.3: Bathymetric map of the North Atlantic with the most important features. FZ, Fracture Zone. Modified from Kandilarov et al. (2008).

Before the formation of a deep ocean in early Cenozoic time, the area between Fennoscandia, Greenland and Svalbard was a shallow, epicontinental sea, connecting the North Sea and the Barents Sea (Eldholm et al., 1990). The structural framework before break-up is dominated by post-Caledonian extension, forming basins at the continental margins off Norway, Greenland and the Western Barents Sea (Faleide et al., 2008).

As the breakup of Pangea progressed northwards, sea-floor spreading was present as early as anomaly 34 (84 Ma) in the Labrador Sea (Roest and Srivastava, 1989).The oldest magnetic anomaly in the Norwegian-Greenland sea is anomaly 24B (53.7 Ma), which marks the initiation of seafloor spreading in early Eocene (Talwani and Eldholm,1977; Lundin and Doré, 2002). From Chron 24B (53.7 Ma) to Chron 13 (35.5 Ma), seafloor spreading in the Norwegian-Greenland sea occurred on the Aegir and Mohns ridges (Figure 2.4a). Spreading on these ridges was coupled to the Gakkel Ridge along a continental transform boundary called the De Geer zone, comprising the Senja, Greenland and Hornsund fracture zones (Faleide et al., 2008).

At chron 13 time (35.5 Ma), spreading in the Labrador Sea ceased and a major reorganization of plate boundaries occurred (Kristoffersen and Talwani, 1977). Greenland became part of the North American plate, and the opening direction of the Norwegian-Greenland-sea changed 30° from NNW-SSE to WNW-ESE (Talwani and Eldholm, 1977). The transform motion along the Senja, Greenland and Hornsund fracture zones turned to extension, ending the West Spitsbergen Orogeny (Steel et al. 1985), initiated spreading on the Knipovich Ridge and turned the Mohns ridge into an obliquely spreading ridge (Figure 2.4b) (Talwani and Eldholm, 1977).

The Iceland plume was located below Greenland during the first phase of spreading in the Greenland-Norwegian Sea (Mjelde et al., 2008). From 42.5 Ma, spreading rates on the Aegir Ridge diminished as the spreading occurred simultaneously with continental extension in East Greenland, where the crust was heated and weakened by the underlying plume (Mjelde et al., 2008). This continued until continental breakup was achieved when the Kolbeinsey Ridge propagated northwards from the Reykjanes Ridge and rifted off the Jan Mayen microcontinent at 25 Ma (Figure 2.4c) (Mjelde et al., 2008). This configuration, with seafloor spreading on the Kolbeinsey, Mohns and Knipovich ridges have continued into the present (figure 2.4d).
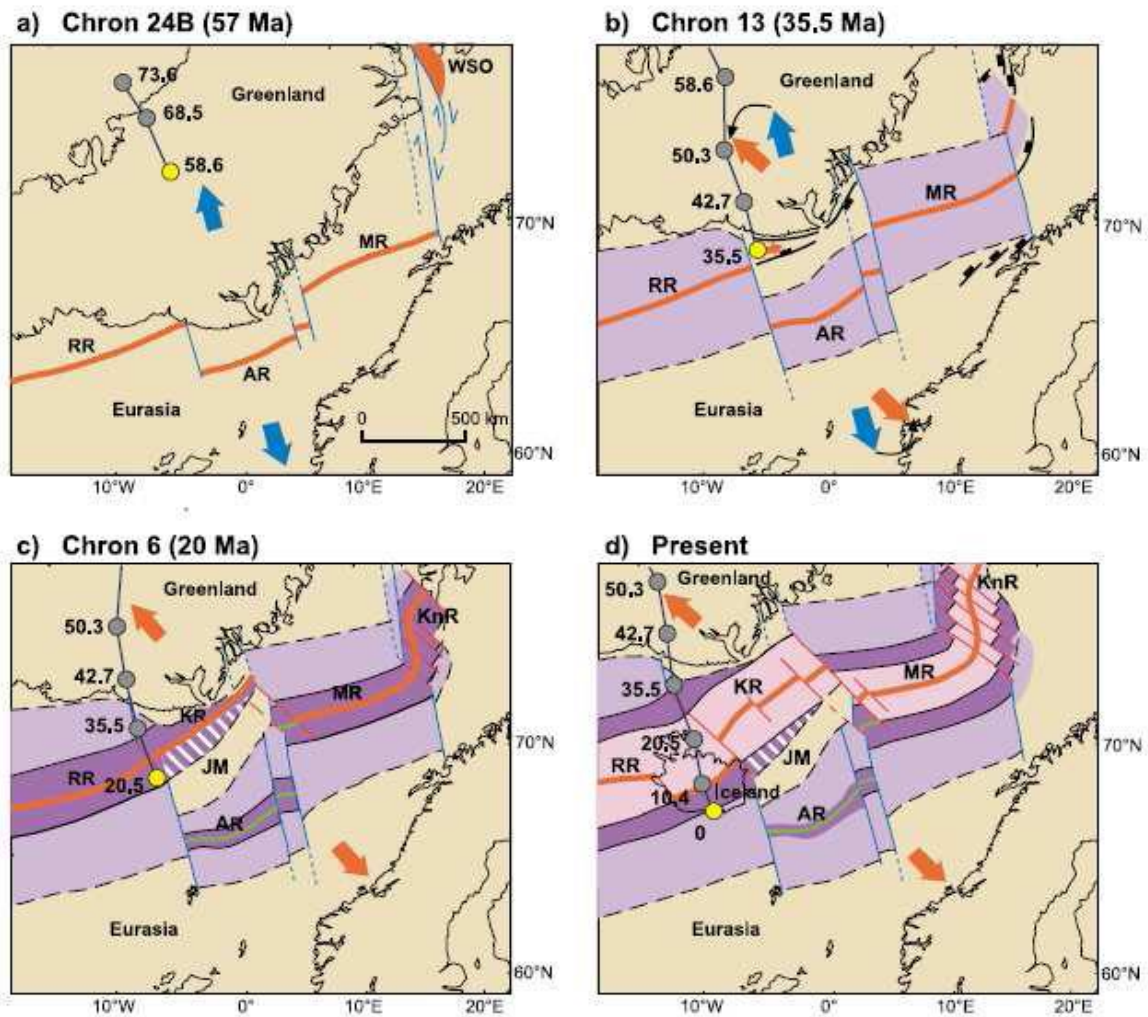
Figure 2.4: Plate tectonic evolution of the Norwegian-Greenland Sea. Grey and yellow dots mark the location of the Iceland Plume center at previous (grey) and the current reconstruction (yellow). Location of plume from Torsvik et al. (2001). Spreading direction before 35.5 ma given by blue arrows, after 35.5 ma by orange arrows. AR, Aegir Ridge; JM, Jan Mayen; KnR, Knipovich Ridge; KR, Kolbeinsey Ridge; MR, Mohns Ridge; RR, Reykjanes Ridge; WSO, West Spitsbergen Orogeny. From Lundin and Doré (2002).

2.4. The Knipovich Ridge

The Knipovich Ride is a spreading centre running from the Mohns-Knipovich bend at 73°45' to the Molloy Fracture Zone at 78°35' (Figure 2.3). The full spreading rate from global plate tectonic modeling is 14.6 mm/a (Dick et al., 2003) making this a slow to ultra-slow spreading ridge. The spreading direction is highly oblique, with an obliquity of 41-55° to the trend of the ridge axis (Dick et al., 2003) with a greater obliquity south of 75° 50' than to the north of this latitude (Okino et al., 2002).

Magnetic anomalies are poorly developed around the Knipovich ridge, making spreading rates and history difficult to determine (Talwani and Eldholm, 1977). Thermal modeling

performed by Crane et al. (1991) gives strongly asymmetric spreading at a rate of 7 mm/a at the western flank, and 1 mm/a at the eastern flank. However, interpretation of magnetic anomalies have been performed by Engen et al., (2008), which found anomalies until anomaly 6 east of the ridge, and anomaly 18 west of the ridge. Results from this study show no indications of asymmetric spreading.

The axial valley is characterized by long, deep and heavily segmented troughs, interrupted by shorter axial highs rising several hundreds of meters above the general bathymetry in the axial valley. The axial highs are of volcanic origin, and the largest anchor seamount belts with a trend parallel to the spreading direction (Okino et al., 2002). The seamount belts show that volcanic activity is persistent at these areas. The large highs are also accompanied by short wavelength mantle Bouguer lows. Thus, the larger of the axial highs may be the surface representation of relatively stable mantle upwelling centers (Okino et al., 2002). The deeper segments are believed to represent segments where amagmatic spreading is the dominant extensional process.

Studies of oceanic crust generated at the Knipovich Ridge have shown that there are large variations in crustal thickness. Kandilarov et al. (2008) interpreted OBS data along a profile oriented parallel to the spreading direction, and the crustal thickness along this profile varied from 3.5 km to 7 km. These variations were attributed to variations in spreading rate. Ljones et al. (2004) interpreted OBS data along a profile crossing three seamount belts, and found the thickness of oceanic crust to vary from 5.6 to 8.1 km, with thick crust within the seamount belts, and thinner crust between the seamount belts, where amagmatic extension is assumed. Farther north on the Knipovich ridge, Ritzmann et al. (2002) found a very thin crust, with a thickness of 3.5 km, which was attributed to slow spreading.

The western side of the Knipovich Ridge is less studied than eastern flank, and no OBS profiles image this area adequately. However, it has been studied by reflection seismic experiments (e.g. Talwani and Eldholm, 1977; Bruvoll et al., 2009). The results from these studies show that the sediments are much thicker on the eastern side of the ridge, and that the basement lies much deeper on the eastern side, also when the isostatic effect of sediments is corrected for (Vogt et al., 1982).

2. Geological Background

Master thesis – Christian Haug Eide - 2010

2.5. The Barents Sea margin and adjacent continental shelf

The Barents Sea margin runs from the Lofoten archipelago to Sørkapp, the southern point of Spitsbergen (Figure 1.1 and 2.3). It developed along the De Geer Zone, the dextral mega shear zone linking spreading on the Gakkel Ridge in the Arctic basin to the Mohns Ridge in the Norwegian-Greenland Sea (Faleide et al., 2008). The shear movement changed to rifting after the major plate reorganization at chron 13 time (35.5 Ma) which changed the spreading direction of the Arctic ridges by 30° to the west (Talwani and Eldholm, 1977). The margin consists of three segments (Figure 2.3), the sheared Senja and Hornsund Margins, linked by the rifted Vestbakken Volcanic Province (Eldholm et al., 1987).

The sheared Senja margin is the southernmost margin segment, where the continent ocean-transition (COT) is confined to a narrow zone within 10-20 km (Breivik et al., 1999).

The Vestbakken Volcanic Province is located southwest of Bjørnøya, and is characterized by rifting. This is due to an east-stepping of the dextral shear zone, creating a releasing bend, which led to basin formation and later breakup. Volcanoes, sill intrusions and possibly a lower crustal high-velocity body have been identified (Faleide et al., 1988; Faleide et al., 2008). The volcanism at this margin segment is mainly associated with breakup in the Early Tertiary, but some mid-tertiary volcanism is also observed (Faleide 1988).

The Hornsund Margin makes up the northwestern boundary of the Barents Sea. It is a sheared margin, with a narrow COT which can be confined to a 5 km wide zone (Breivik, 2003). The margin is characterized by a downfaulted marginal terrace, consisting of rotated fault blocks, formed during the margin development (Breivik, 2003). The fault blocks subsided along the Hornsund Fault Zone and the Knølegga fault.

Landward of the COT, the continental shelf can be divided into two units. The Barents Sea sedimentary basin province is present south of 74°N, a region characterized by a number of sub-basins and highs, created by Late Paleozoic to early Tertiary extensional events (Faleide et al., 2008). North of 74°N lies the Svalbard platform, a region mainly unaffected by the late Mesozoic extension, probably shielded by the transform system to

the west (Faleide et al., 1991). However, the region is deeply eroded, leading to high P-wave velocities near the sea floor (Hjelstuen et al., 1996, Breivik et al., 2003).

2.6. Cenozoic sedimentation

Two large trough mouth fans, the Storfjorden and Bjørnøya fans, lie adjacent to the Barents Sea margin (figure 2.3). The fans are depocenters for sediments eroded from the Barents Sea, transported to the margin by glacio-fluvial drainage systems and ice streams (Butt et al., 2000; Ottesen et al., 2005).

The sediments on the Barents Sea-Svalbard margin have been divided into four sequences, G0 to GIII, based on seven regional reflectors, R7 to R1 (Figure 2.5). G0 is composed of Early-Mid Tertiary pre-glacial sediments, and is bounded by the oceanic basement and the reflector R7. The sequences GI-GIII represent the Late Cenozoic (Plio-Pleistocene) glacial sequences. GI is bounded by R7 and R5, and corresponds to initial glacial growth, with dominantly glaciofluvial sedimentation along the shelf edge and subsequent remobilization as debris flows in 2.3-1.6 Ma (R7-R6), and glaciers reaching the shelf edge at 1.5-1.3 Ma (R6-R5) (Butt et al., 2000). Unit GII is bounded by R5 and R1, and represents several episodes of glacial advance and retreat across the margin (Butt et al., 2000). GIII marks a prominent decrease in glacial activity, and the end of the outbuilding of the fan system (Hjelstuen et al, 1996).

The drainage area of the Storfjorden fan is assumed to correspond to the present day watershed on the Svalbard archipelago, and comprises the eastern part of Spitsbergen, major parts of Barentsøya and Edgeøya. The easternmost and westernmost parts of this drainage area is defined by Hopen and the Hornsund Fault Zone. Erosion estimates indicate approximately 3300 m of erosion since breakup in this area, and 1700 m of the erosion occurred during the late Pliocene and Pleistocene (Hjelstuen et al., 1996).

The distal parts of the Storfjorden and Bjørnøya fans reach the Knipovich Ridge. The periodicity and high rate of sedimentation provides a way of dating tectonic events on the ridge by looking at the interaction between dated sedimentary units and tectonic processes (Bruvoll et al., 2009).
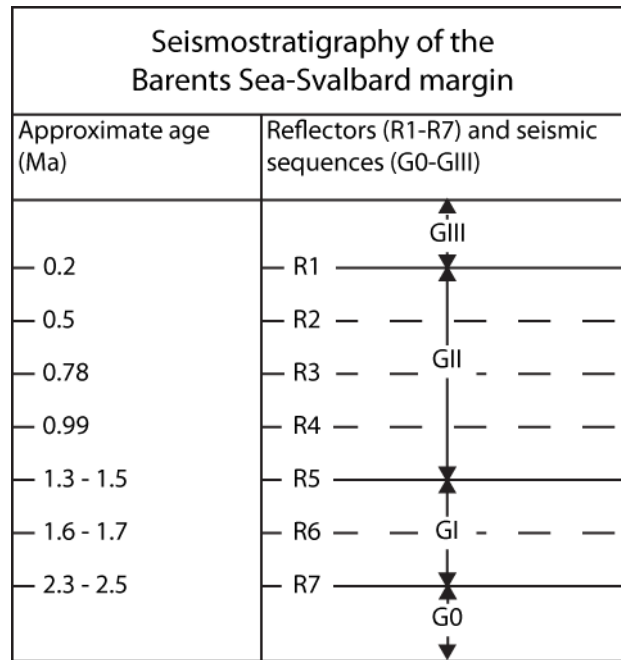
Figure 2.5: Seismostratigraphy of the western Barents Sea-Svalbard margin with ages from Butt et al. (2000) (modified from Faleide et al., 1996).

3. Acquisition and processing of geophysical data

3. Acquisition and processing of geophysical data

3.1. Acquisition

Two lines of ocean bottom seismometer (OBS) data were collected west of Bear Island by use of the R/V Håkon Mosby in summer 2008 (Figure 3.1) (Kandilarov and Mjelde, 2008). The lines were named Bear Island North (BIN) and Bear Island South (BIS). BIN is 322 km long, starts west of the Knipovich Ridge at 74°56'51.7''N, 7°37'8.04''E, and ends at 74°32'32.99''N, 18°29'13.1''E, northwest of Bear Island (Figure 3.1). The BIN profile will be described in this thesis.

The BIS profile runs from 72°6'50''N, 9°36'00''E to 74°27'36''N, 19°15'47''E, and uses both OBSs and land stations. The profile starts at oceanic crust created by the Mohns ridge, runs across the Vestbakken Volcanic Province, and ends west of Bear Island. This profile has been described in Czuba et al. (2010).

Gravimetric and magnetic measurements were also conducted along the lines, with a Lacoste-Romberg gravity meter, and a marine proton magnetometer.

3.1.1. Multi Channel Seismic Data

Multi channel seismic (MCS) data for the BIN profile were collected in 2006 by use of the R/V Håkon Mosby (Johnsen, 2006). The MCS line is plotted as a purple line on figure 3.1, and it is almost overlapping the BIN line, with a deviation of about 2 km in the western end of the profile and about 1 km in the eastern end. The line is 365 km long and crosses the Knipovich Ridge at approximately 75°N. It runs from Bear Island to about 70 km past the Knipovich Ridge.

The seismic source was a tuned air gun array, consisting of six air guns with volumes of 9.5 L (580 in^3), 4.9 L (300 in^3), 3.9 L (240 in^3), 2.2 L (136 in^3), 1.5 L (90 in^3), and 1 L (60 in^3), giving a total volume of 23 L (1406 in^3) (Johnsen, 2006). Using air guns of different volumes will increase the signal-to-bubble pulse-ratio, because the bubble period is dependent on the volume of the air gun. Since the shot time is equal on all air guns, and the bubble period is different for all air guns, this will cause constructive interference for the primary pulse, and destructive interference for the bubble pulse.
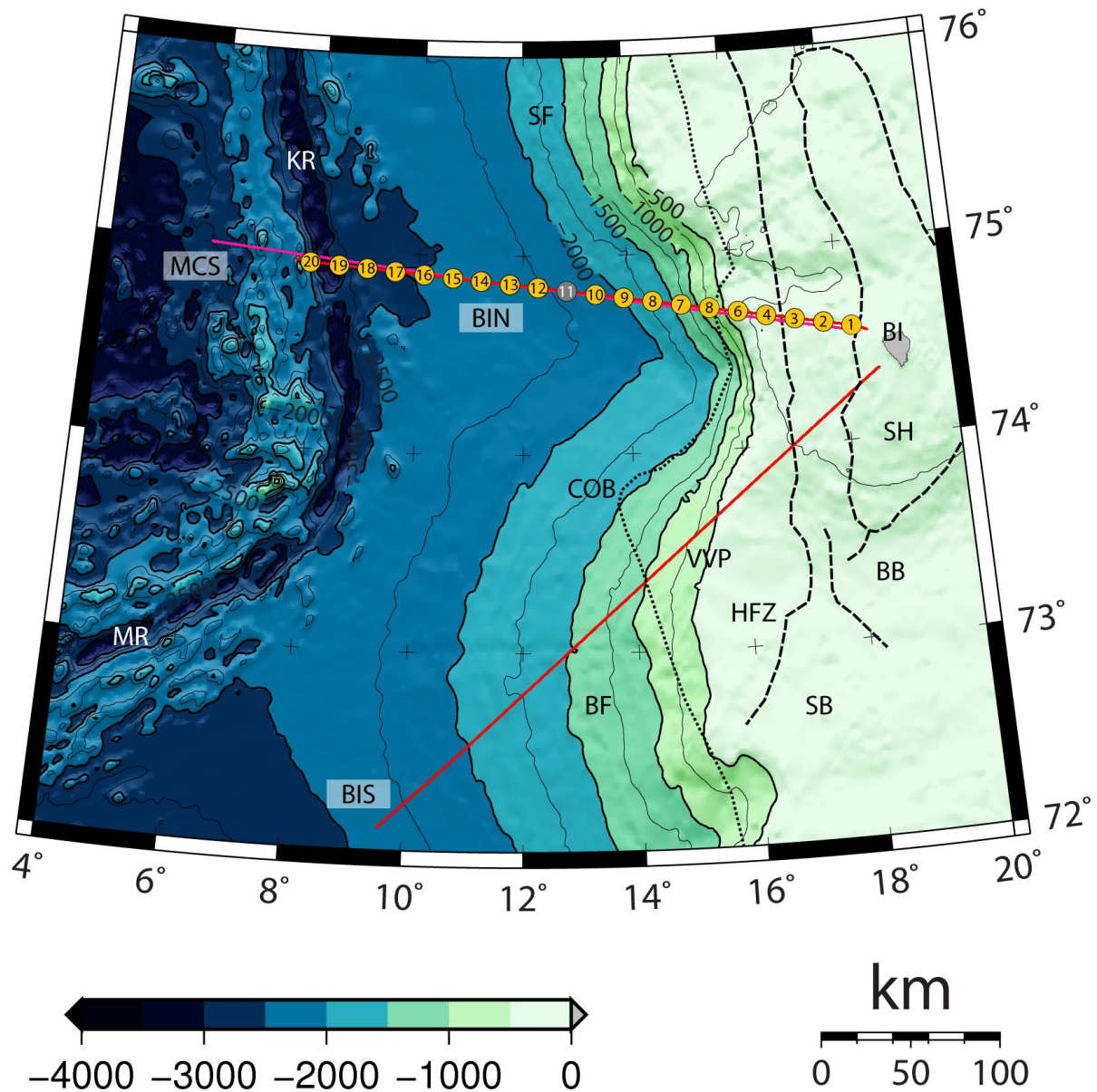
Figure 3.1: Overview map of the study area with the continent-ocean boundary (dotted line), most important faults (dashed lines) and other elements. Numbered circles are positions of OBSs. BF, Bear Island Fan; BI, Bear Island; BIN, Bear Island North seismic line; BIS, Bear Island South seismic line; COB, Continent-ocean boundary; HFZ, Hornsund Fault Zone; KR, Knipovich Ridge; MCS, Multi Channel Seismic line; MR, Mohns Ridge; SB, Sørvestnaget Basin; SF, Storfjorden Fan; SH, Stappen High; VVP, Vestbakken Volcanic Province. Locations and extent of structural elements from Ritzmann and Faleide (2007).

The vessel speed was kept at 5 knots, and the shot spacing was 50 m. The air guns were fired at 5 meters depth. The streamer used was a 3 km long WesternGeco Nessie3 streamer with 240 channels and 12.5 m group length, kept at a depth of 6m. The recording length was 12 seconds.

The quality of the MCS data acquired on the lower continental slope, deep ocean and the Knipovich ridge is very good, but the data from the upper continental slope and continental shelf is of poor quality, mainly due to multiples and limited penetration.

3.1.2. Ocean Bottom Seismometer Data

The seismic source for the OBS survey consisted of an array of four air guns with a volume of 20 L (1200 in^3) each, giving a total volume of 80 L (4800 in^3) (Kandilarov and Mjelde, 2008). The air guns are of the same size, because it is not as important to attenuate the bubble pulse in regional OBS surveys as when acquiring MCS data. Shots were fired every 200 m, triggered by the navigational computer. The OBSs contains two horizontally oriented geophones, one vertically oriented geophone and one hydrophone. The geophones are orthogonally and gimbal mounted to make sure the geophones are oriented correctly regardless of the inclination of the OBS itself.

20 seismometers were deployed, but OBS 11 did not record useful data. The data quality is moderate based on signal range and noise (Minakov, 2008). The data were preprocessed at IFM-GEOMAR in Germany.

3.2. Data Processing

3.2.1. Processing of multi channel reflection data

Processing of the multi channel seismic (MCS) data were conducted by Bent Ole Ruud at the University of Bergen. The focus of the processing was to enhance the basement reflector, and attenuate multiples at the part of the profile imaging the shelf and upper slope.

The processing consisted of these steps, in the following order:

1. SEG-D to SEG-Y conversion
2. Anti-aliasing filter (100 Hz lowpass)
3. Resample from 2 ms to 4 ms
4. Spatial amplitude smoothing
5. Incoherent noise attenuation
6. Spiking deconvolution to remove bubble pulses
7. fk-filter to remove streamer noise
8. Sort from shot gather to CMP (Common Mid Point) gather

9. Spherical spreading correction

10. Mute

11. Least squares multiple removal

12. Velocity analysis on DMO (Dip moveout) corrected CMP gathers

13. Pre-stack Kirchhoff time migration

14. Stacking

In the following section, short descriptions of the processing steps will be given:

Anti-alias filter and resampling: To avoid aliasing of high frequencies in a dataset, the highest frequency in the dataset must be lower than the Nyquist frequency. The Nyquist frequency, f_N is given by this equation,

$$f_N = \frac{1}{2\Delta t}$$

where Δt is the sampling interval (Keary et al., 2002). The Nyquist frequency is 125 Hz when sampling at a rate of 4 ms. In order to resample from 2 ms with a Nyquist frequency of 250 Hz, a lowpass filter must be applied. In this dataset, a lowpass-filter with cutoff frequency at 100 Hz and a steep slope was used to remove the frequencies lower than the Nyquist frequency

Spatial amplitude smoothing: Spatial amplitude smoothing corrects variations in source strength and receiver sensitivity by comparing single traces to nearby traces.

Incoherent noise attenuation: Incoherent noise is removed by comparing shots and traces, keeping coherent events while removing incoherent events. This assumes noise to be incoherent while arrivals are assumed to be coherent.

Spiking deconvolution: Spiking deconvolution is performed to replace the relatively long-period recorded wavelet, which include bubble pulses, with a wavelet that is as short as possible, a spike.

fk-filtering: In fk-filtering, the seismic data is plotted with frequency against apparent wavenumber k_a, where the relation between frequency and apparent wavenumber is given by this equation,

$$f = v_a k_a$$

16

where f is frequency, k_a is the apparent wavenumber and v_a is the apparent velocity of arrivals along the streamer. This means that arrivals can be filtered out on basis of their apparent along-streamer velocity. Deeper arrivals will have very high apparent velocities, since the angle between the wavefront and the streamer will be small. Disturbances propagating along the streamer will have low apparent velocities, because their wavefronts will be almost perpendicular to the streamer (Keary et al., 2002).

Sort from shot gather to CMP gather: In order to more conveniently process the dataset, the seismic traces are sorted in such a way that all traces that have been reflected at the same point are placed in one group. Assuming horizontal layers, this point is the mid-point between source and receiver. Sort to CMP gather must be performed before stacking.

Spherical spreading correction: As a seismic disturbance is spreading in the subsurface, the wavefront will resemble the shell of a sphere. As time passes, the spherical shell will expand, and the energy per unit surface area will diminish. This is corrected for by multiplying the amplitude of the traces with a factor that increases with increasing travel time.

Mute: Far-offset arrivals on the shallow sections are muted in order to remove the direct wave and parts most affected by NMO stretch (Figure 3.2).

Least squares multiple removal: Least squares multiple removal is a way of removing multiples by predicting the arrival time of the multiple by using information about the water layer. The predicted multiples are subsequently subtracted from the seismic data.

Velocity analysis and NMO correction: Velocity analysis is performed on the CMP gathers in order to find the velocity-depth function that will correctly stack the data. A correct velocity-depth function will remove the moveout and place primary reflection events on a straight line (Figure 3.2). The velocity analysis is carried out on dip moveout corrected CMP gathers, but the dip moveout correction is only applied for the velocity analysis, it is not carried on into the migration.
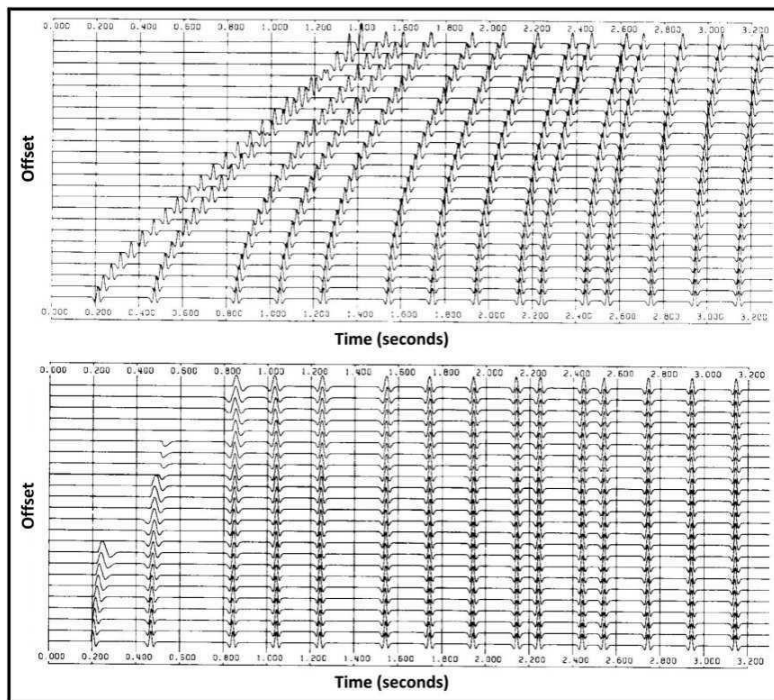
Figure 3.2: Synthetic seismogram before (above) and after (below) NMO correction and muting. Note the slight NMO stretch on the far-offset parts of the two upper reflectors (From Dunkin and Levin, 1973).

Pre-stack Kirchhoff time migration: When a seismic signal encounters a sharp edge or a point reflector, it will be diffracted. In the presence of a dipping layer, the reflection is displaced up-dip. Migration is the process of reconstructing a seismic section by using the velocity model in such a way that reflection events are placed at their correct location both in space and time. Migration also improves the resolution of seismic sections by focusing the energy spread over a Fresnel zone, and by collapsing diffractions. However, migration of 2D-seismic data is not as accurate as migration of 3D data, because there is no information about the off-line geometry, and therefore offline effects cannot be corrected (Keary et al., 2002). Pre-stack time migration is performed prior to stacking, and gives better results than post-stack migration, but is also much more time consuming.

Stacking: When velocity analysis is complete, the traces in each CMP gather can be summed, increasing the signal-to-noise ratio by a factor of $\sqrt{n}$, where n is the number of traces.

3.2.2. Processing of Ocean Bottom Seismometer Data

The OBS data were subject to standard OBS data processing in Seismic Unix. The five steps performed were velocity reduction, bandpass filtering, automatic gain control, debiasing and predictive deconvolution. Examples of the processing steps are given in figure 3.3.

Velocity reduction decreases the space needed to display the seismograms by removing areas without arrivals. This is done by converting the time axis to $time - \frac{offset}{v_{red}}$, where v_{red} is the reduction velocity, and deleting the portions of the traces that have reduced time below zero. Since the highest commonly encountered velocity of propagation in crustal scale refraction studies is the P-wave velocity in the upper mantle, the reduction velocity is chosen to be 8 km/s. This has the added benefit that it makes arrivals from the upper mantle easier to identify, because they will be displayed as horizontal arrivals. Slower arrivals will be displayed as dipping lines, and slower arrivals will dip more steeply. This processing step was performed as part of the preprocessing at IFM-GEOMAR in Germany.

Most seismograms in this study show considerable amounts of low frequency noise (figure 3.3a). The seismic signal has most of its power in the 2-20 Hz frequency band. A Fourier transform of the data show that most of the noise is in the 0-0.8 Hz frequency band. Because the signal and most of the noise are present in separate frequency bands, noise can be removed by filtering out undesired frequencies (Figure 3.3b). A bandpass filter with trapezoid shape, sine tapered edges and the parameters 2, 5, 15 and 20 Hz was constructed. The trapezoid shape and tapered edges is used to minimize ringing caused by sharp corners in the filter (Gibbs phenomenon).

Automatic gain control works by finding the mean of all amplitudes in a given time window, and multiplying the interval with the number that raises the mean to a pre-determined value. This is performed to enhance late low amplitude arrivals. A time window of 2 seconds was found to give good results, and subsequently used on these data (Figure 3.3c).
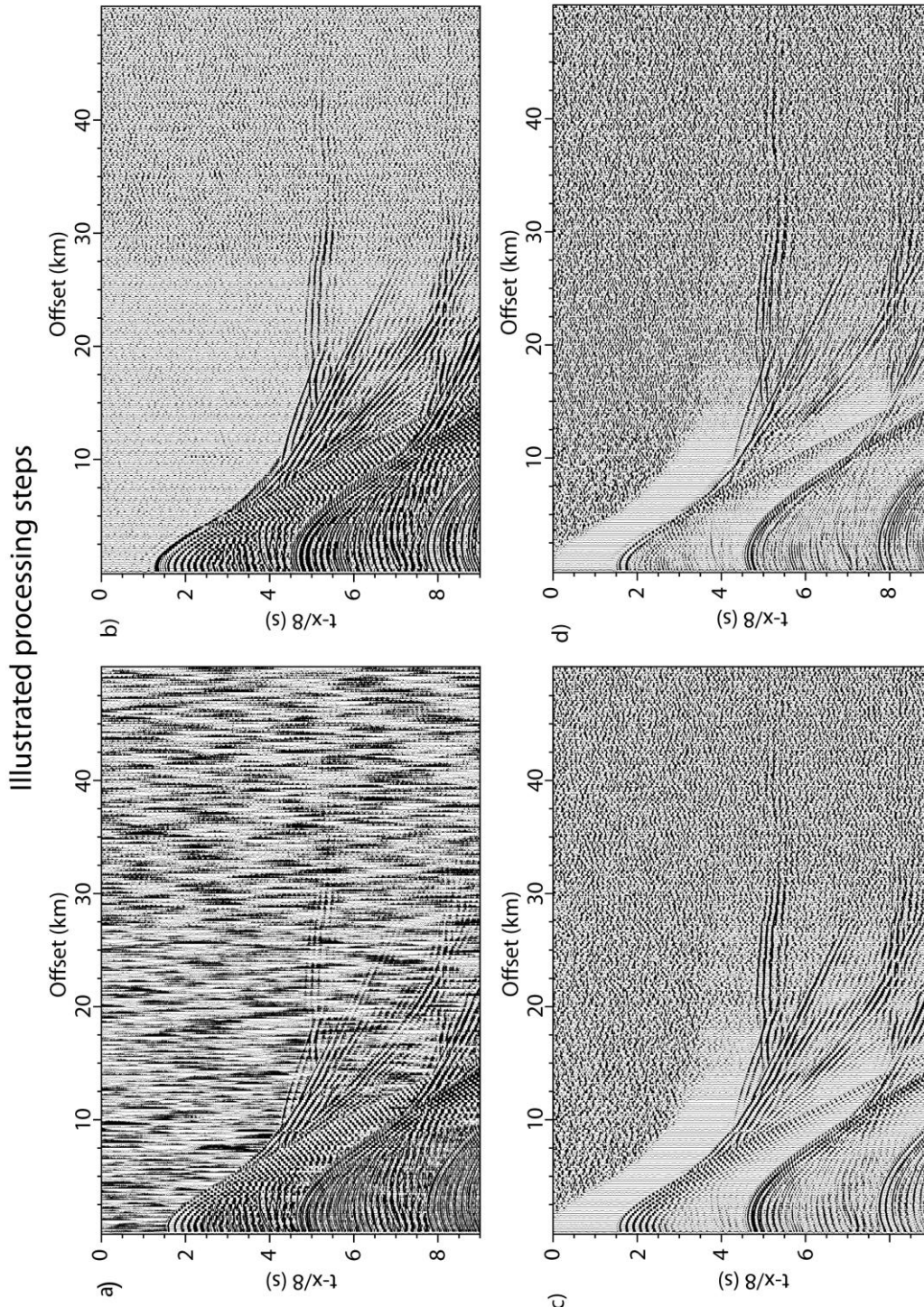
Figure 3.3: Seismograms from OBS 12 illustrating different processing steps. a) Velocity reduction only. Note the low frequency noise present everywhere except for the very strongest arrivals near zero offset. b) Bandpass filtering with the parameters 2, 5, 15, 20 Hz performed in addition to steps in a. Weaker arrivals are much easier to identify. c) AGC and debiasing performed. AGC did not lead to significant improvements of this dataset. Note the artifact related to the 2 second boundary of the AGC boundary starting at 0 seconds at 2 km offset, running to 3 seconds at 12 km offset. d) Deconvolution with 11 second correlation window applied. Note the decreased ringing, especially after the arrival at 4 seconds and 10 km offset.

Debiasing is performed to display zero amplitude crossings correctly in the data. Ideally, the average of a trace will be zero, but traces can be shifted by different reasons, so that an amplitude is recorded without a disturbance of the seismometer. The process works by subtracting the mean amplitude for every single trace.

Deconvolution is used to decrease ringing which may mask later arrivals. Several methods were tried, but spiking deconvolution with a correlation window of 11 seconds gave best results (Figure 3.3d).

3.2.3. Processing of gravity data

In order to use measured gravity anomalies to investigate the structure of the crust and upper mantle, certain corrections must be made. The processing of the acquired gravity data were performed at the University of Bergen by Arne Gidskehaug at the University of Bergen. The basic processing steps are described in the following sections:

The earth is not a perfect sphere, but rather flattened at the poles. Because the magnitude of the gravitational force varies with the square of the distance between two bodies, the magnitude of gravity is therefore dependent on the latitude, with a minimum on the equator. The earth is also rotating, causing a centrifugal force to act on all bodies on its surface. The centrifugal force is dependent on latitude, with maximum effect on the equator, and no effect on the poles. The centrifugal force will also diminish the measured gravity.

The first step of gravity processing is to correct for these two effects, by subtracting the gravity for a rotating oblate spheroid from each gravity measurement. This value is given by the *reference gravity formula* (Fowler, 1990).

The second step is to correct for instrumental drift. This consists of comparing the installed sea gravimeter to the known gravity measured at land surveying base stations by use of land gravimeters before and after the survey, and applying a linear correction function.

When a vessel is moving eastwards, it will increase the centrifugal force in the same way as increasing the rotation rate of the earth, and travelling westwards will make the apparent rotation rate smaller. This effect is countered by Eötvös correction (Glicken, 1962).

21

When these corrections are applied, resulting gravity measurement is the *free air anomaly.* The measured free air anomaly is shown in figure 3.4.
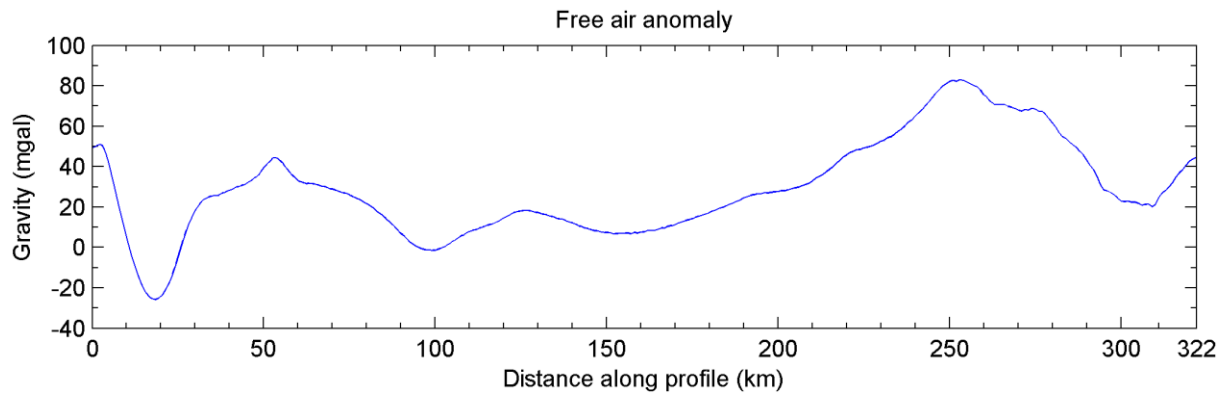
Figure 3.4: Observed gravity anomaly along the profile.

4. Interpretation and modeling procedures

4.1 Multi channel seismic data

The multi channel seismic (MCS) data has much higher resolution than the OBS data, but only images the sediments and the top of oceanic basement because of limited penetration. Interpreting the MCS data was the initial step when working with this dataset, because having constraints in the upper layers is a major advantage when doing OBS modeling. Interpretation of MCS data was performed in Petrel.

Four sedimentary units were defined, based on seismic facies (Figure 4.1a). Unit 1 is the lowermost unit, characterized by low amplitude, moderate frequency, relatively continuous reflectors (Figure 4.1b). Unit 2 is characterized by slightly disturbed, low amplitude, low frequency, relatively discontinuous reflectors (Figure 4.1b). Unit 3 is is a thick package characterized by chaotic appearance with a few, disturbed, moderate amplitude reflectors and abundant diffraction hyperbolas (Figure 4.1.b). Unit 4 is characterized by high amplitude, high frequency, sub-parallel reflectors with scattered chaotic packages (Figure 4.1b). Top oceanic basement was also interpreted, and interpolations were made in areas with poor data quality. Correlation to the Bjørnøya Fan seismic stratigraphic network (Faleide et al., 1996) will be discussed in chapter 6.

The interpreted horizons were depth converted with the velocities 1.48, 2.2, 2.7, 3.5 and 4.5 km/s, in the water layer, unit 1, unit 2, unit 3 and 4, respectively. The velocities are approximated from profile 3 in the OBS98 survey (Breivik and Mjelde, 2001). After preliminary OBS modeling of the sediments using OBSs 12, 13, 14, 15 and the east side of OBS 16, the horizons were depth converted again with the new velocities in the sediments, to account for lateral variations in P-wave velocities.

a)

b)
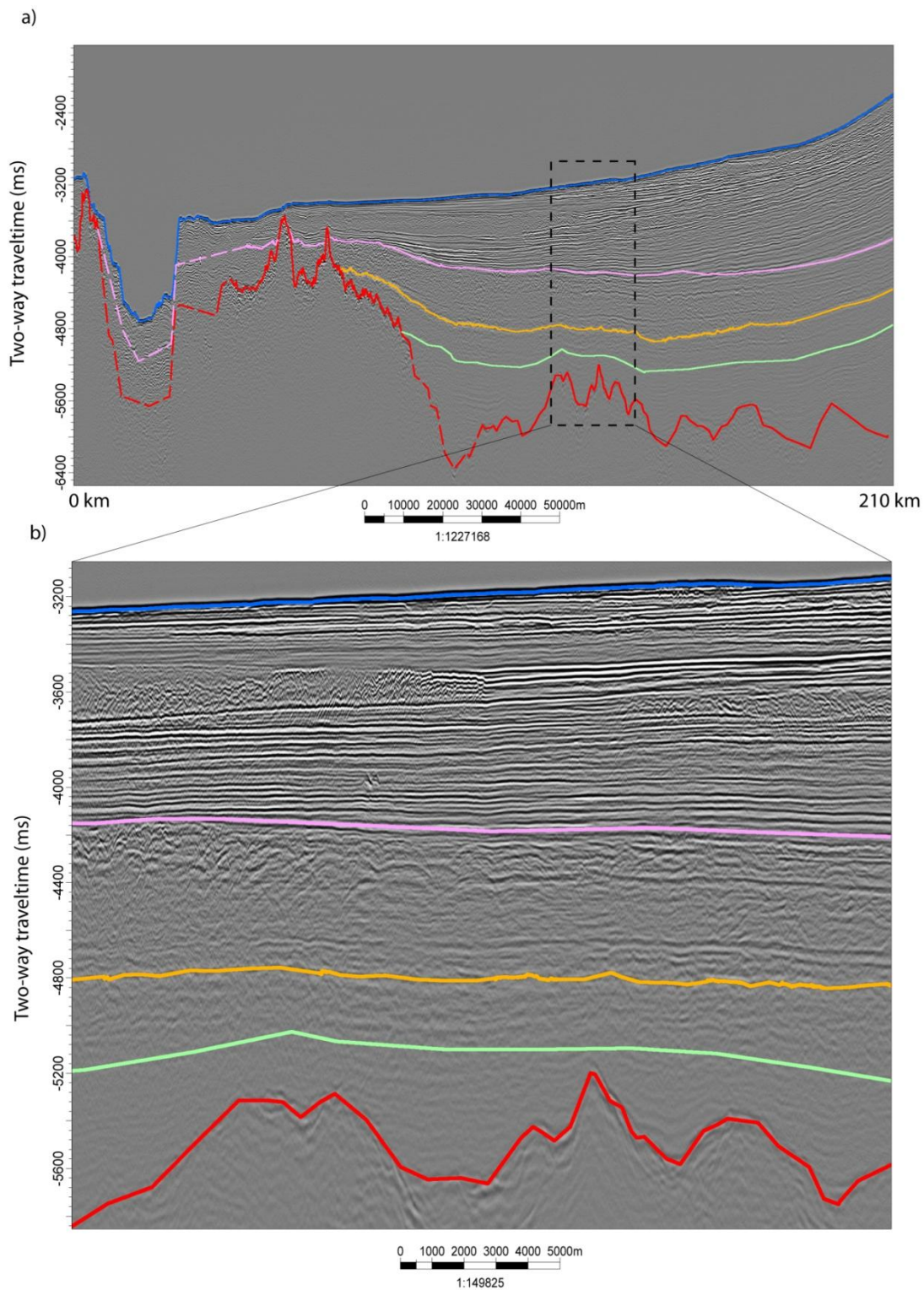
Figure 4.1: a) Interpreted seismic horizons used to make the starting model for the velocity model. Top oceanic basement (red, stippled line where interpretation is uncertain), top unit 1 (light green), top unit 2 (orange), top unit 3 (pink), seabed (blue). b) Close-up. Note the chaotic unit at -3600 ms, and the hummocky appearance of unit 2 (orange to pink).

24

4.2 Ocean bottom seismometer data

4.2.1. Interpretation of OBS seismograms

Seismograms containing data from the vertical geophones and hydrophones were interpreted using the seismic interpretation software GeoGraphix by Landmark. The arrivals recorded by the vertical geophone and hydrophone are assumed to represent P-wave arrivals. Interpretation of S-waves falls beyond the scope of this thesis.

Because frequency filtering and deconvolution causes a slight ringing around the arrivals in the data, as much as possible of the interpretations were performed on seismograms with only traveltime reduction applied. Hence, most of the first-arrival parts of the sediment phases were picked prior to further processing. Most of the further interpretation was performed on seismograms with all processing steps applied, except for deconvolution. Deconvolution had the added benefit that the decreased ringing increased the definition of the far-offset (more than 50 km) arrivals, so most of the far offset arrivals and secondary arrivals were interpreted on the deconvoluted seismograms.

At this stage, arrivals were interpreted to belong to five different phases: The direct wave, refracted waves from the sediments, refracted waves from upper crystalline crust, refracted waves from deeper interfaces, and reflections. Each category was recognized from shape of the arrival, travel time, and dip (apparent velocity). The appearance of most of the phases is demonstrated in figure 4.2. Uncertainties of the picks were set to 30 ms for the direct wave, 50 ms for the sediments, 75 ms for the upper crystalline crust, and 100 ms for arrivals from the lower crust and mantle.

4.2.2. OBS modeling

The picks were imported into Rayinvr, a 2D raytracing forward modeling and inversion software package (Zelt and Ellis, 1988; Zelt and Smith, 1992).

In order to create a starting model for the OBS modeling, bathymetry from echo sounder data and depth converted horizons from the MCS data were sampled at a 2 km interval and imported. Since there are no reliable interpreted reflectors east of 200 km, the layers were simply extrapolated from 200 to 322 km. In the areas where the top oceanic basement is poorly imaged by the multi channel seismic data, an interpretation connecting the strongest reflectors were used. Horizons corresponding to top oceanic

25

layer 3 and the Moho were also added, mimicking the overall trend of the oceanic basement, at depths of 3 and 7 km below the top oceanic basement. In order to avoid unnecessary detail, a minimum number of depth nodes are used in areas without good quality MCS data.
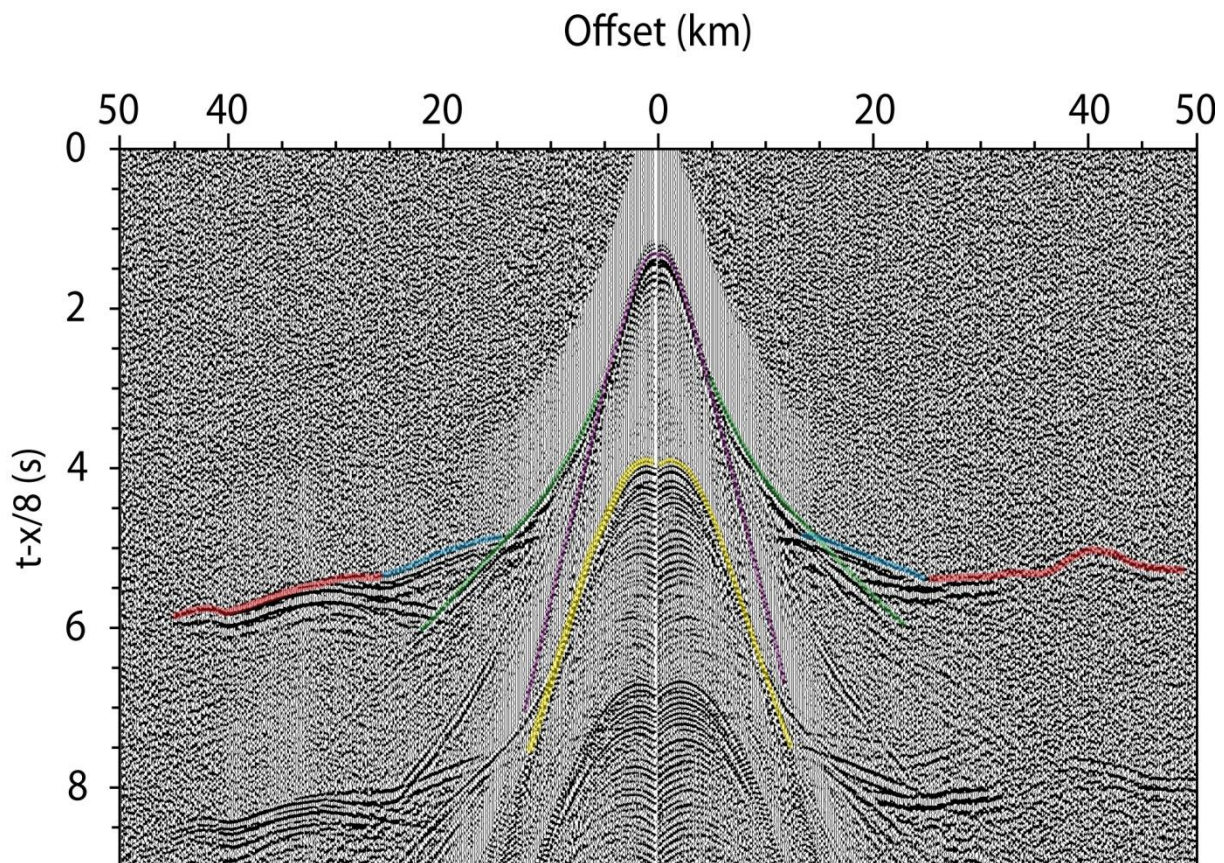
Figure 4.2: Picked phases on OBS 9, deconvoluted seismogram. Four of the interpreted phases are shown on this figure. The direct wave (purple) has a characteristic hyperbolic shape. The refracted wave from the sediments (green) shows a relatively low apparent velocity (steep dip) and gradual increase in velocity with depth. The direct wave from oceanic layer 2 (blue) generally shows a much higher apparent velocity than the wave from the sediment, and has a straight to very irregular shape. The deeper arrivals (red) generally show an apparent velocity, close to 8 km/s (almost horizontal), and generally little variability. The first waterlayer multiple is marked in yellow.

Velocity nodes were created at the location of each OBS (including the non-functional OBS11), with a spacing of 16 km. In areas with complex geology, additional nodes were created when needed. Velocity nodes are defined for each layer, and each node contains information about the P-wave velocity at the top and bottom of the layer. Velocities are linearly interpolated between neighboring nodes, making velocity gradients possible both laterally and vertically.
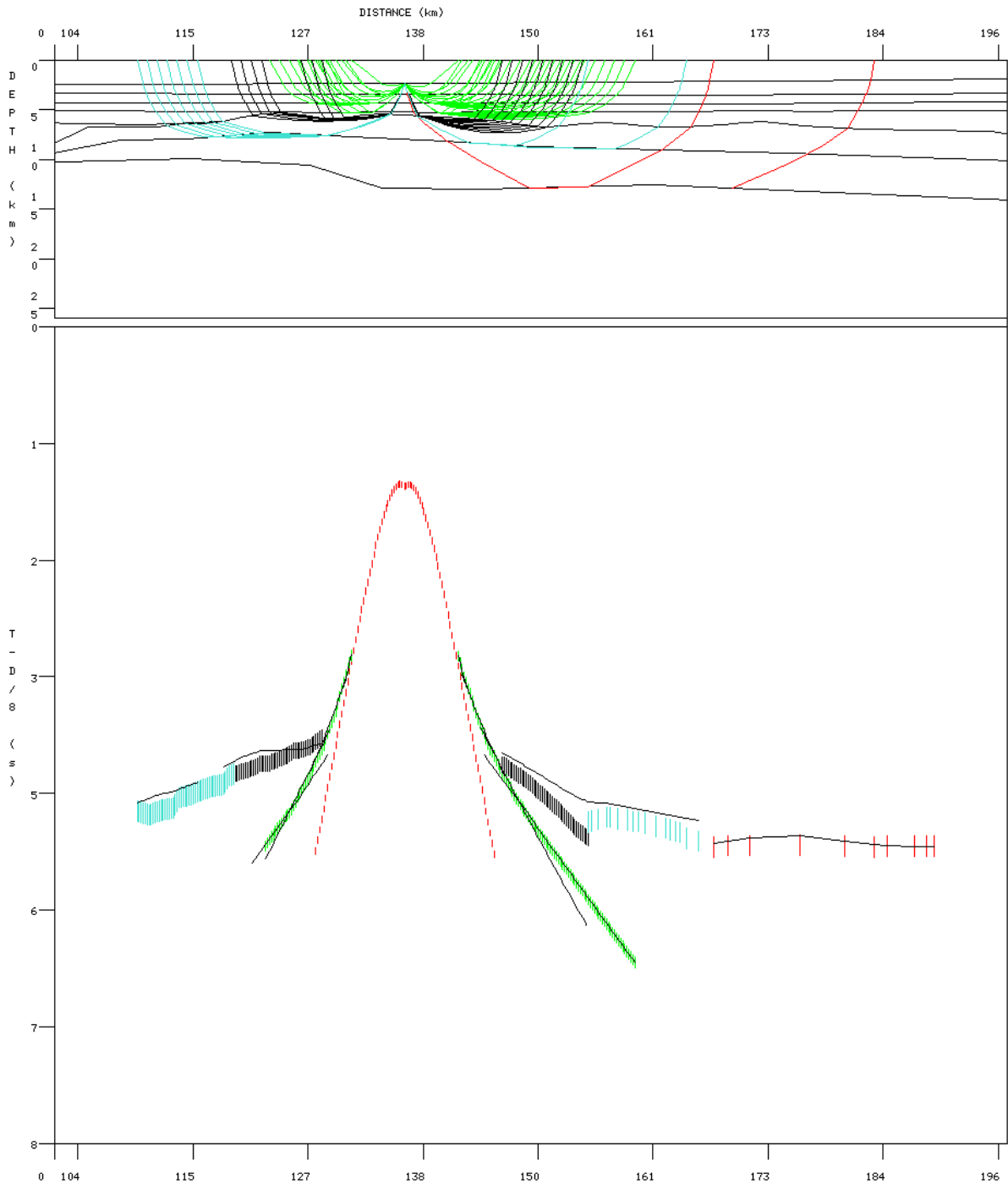
Figure 4.3: Traced rays for OBS 12. The upper plot shows the path of the rays through the subsurface, and the lower plot shows how the calculated rays (thin, black lines) fit the picks (short, colored, vertical lines; uncertainty bars). This figure shows a good fit for the sediments (green picks), and a poor fit for the oceanic basement (black picks), and oceanic layer 3 (light blue). This figure is plotted with a velocity in oceanic layer 2 0.5 km/s too high. The calculated arrival from the Moho (red) fit despite an error in the overlying velocity model. When the velocities in the oceanic layer is correct, the calculated rays will fit within the uncertainty bars (figure A.12).

Rayinvr traces rays through the model, and calculates and displays how well the calculated arrivals fit the picks. The calculated rays are plotted over the picks (Figure 4.3), so the user can see how the model must be changed in order to achieve a better fit. In the areas with good quality interpretations from the reflection seismic data, only the velocities were changed. In areas without good quality reflection data (see figure 4.1a, red stippled lines), both the velocity and the depth of the nodes were changed.

As suggested by Zelt (1999) the modeling procedure was carried out in a layer stripping way, modelling one layer at a time. The upper layer is modeled first, and when the velocity and depth structure makes the calculated rays fit the picks sufficiently, the next layer is modeled. In practice, the nodes for one layer were adjusted manually until a reasonable fit between calculated arrivals and picks was achieved. The *damped least-squares* program in the Rayinvr software was then used to fine-tune the parameters by inversion. This procedure is continued until all layers are resolved.

4.3 Gravity modeling procedure

After construction of a velocity model, the gravity data were modeled using GRAVMAG (Pedley, 1993), a 2.5D gravity and magnetic modeling program. The program works by calculating the gravity of a number of constant density polygons, and it assumes that the modeled profile is continuous in the crossline-direction. The line is extended 300 km at each end by extrapolating the endpoints horizontally to avoid edge effects.

The layers in the velocity model were divided into enough polygons to capture the velocity variations in each layer. The average velocity in each polygon was calculated by finding the average velocity of the four corner nodes in each polygon. The P-wave velocity-density relationship for oceanic layers 2 and 3 were taken from Carlson and Raskin (1984). For the remaining lithologies, the P-wave velocity-density relationship was taken for the Nafe-Drake curve (Ludwig et al., 1970) (figure 4.4).
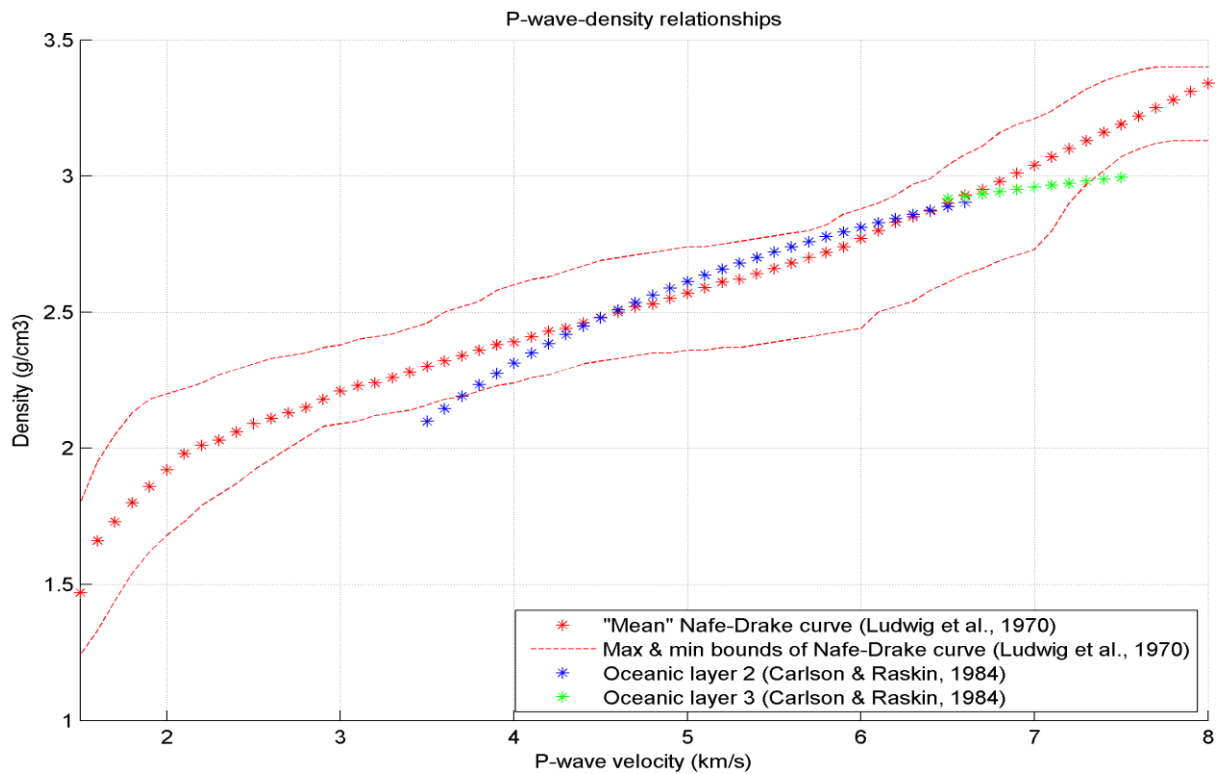
Figure 4.4: P-wave-density relationships. From Ludwig et al. (1970) and Carlson and Raskin (1984).

If the P-wave model is correct, it should be possible to achieve a fit between the calculated gravity and the observed gravity by doing reasonable adjustments of the density of the upper mantle and crustal rocks within the bounds given by the Nafe-Drake curve. If it is not possible to obtain such a fit, the P-wave model should be reevaluated.

4.4. Uncertainties

Models obtained by forward modeling of seismic traveltimes should not be assumed to represent unique solutions (Zelt, 1999). The quality of the model depends on the quality of the MCS and OBS data, the quality of interpretation of the data and the ray coverage. However, several properties can be measured to investigate the resolution and fit of calculated rays with the observed picks. These metods will not give a picture of how unique a solution is, but it will give an impression of how well a particular model is in accordance with the data, which parts of the model is better adjusted to the data, and which parts are more resolved.

29

In Rayinvr, the main method of expressing the goodness of fit between the calculated rays and the observed picks in relation to the pick uncertainty is the χ^2 (chi-squared) value (Zelt and Forsyth, 1994). χ^2 is defined as

$$\chi^2 = \frac{1}{n} \sum_{i=1}^{n} \left(\frac{T_{0_i} - T_{c_i}}{U_i} \right)^2$$

where T_0 is the observed arrival time, T_C is the calculated arrival time, U_i is the uncertainty and n is the number of picks. It follows from this equation that the χ^2 is weighting the mismatch between calculated and observed arrival time in such a way that a value of $\chi^2 \leq 1$ is a fit. χ^2-values closer to zero than one signifies that the model is over-parameterized.

Misfit between picks and calculated rays can be expressed by using root mean square (RMS) time values. Expressed as a formula, the root mean square-time is given by this formula,

$$T_{rms} = \sqrt{\frac{\Sigma (T_{0_i} - T_{0_c})^2}{n}}$$

where the variables are as the formula for χ^2 (above). The RMS time shows how large the travel time misfit between calculated and picked arrivals is. Since the unit for RMS time is seconds, the RMS misfit is easy to visualize. χ^2- and RMS for the model is presented in table 4.1.

Table 4.1: RMS- and χ^2-values by ray type.

Layer	Wave type	Number of picks	T_{RMS}	χ^2
Sediments	Diving wave	1752	0,049	0,946
Layer X	Diving wave	50	0,053	1,132
Oceanic layer 2	Diving wave	1236	0,062	0,693
Oceanic layer 2	Head wave	23	0,114	2,406
Oceanic layer 3	Diving wave	1799	0,098	0,959
Upper mantle	Head wave	1309	0,097	0,939
Upper mantle	Diving wave	143	0,079	0,624
Upper continental crust	Diving wave	344	0,051	0,458
Lower continental crust	Diving wave	481	0,068	0,461
Lower continental crust	Head wave	307	0,120	1,454
All picks		**7444**	**0,080**	**0,871**

In order to estimate the sensitivity of the model to changes in the properties of the layers, each layer had the velocity and depth of interfaces raised and lowered until the calculated rays did not fit into the uncertainty bars. The sedimentary layers are sensitive to changes larger than ±0.3 km in depth and ±0.1 km/s in velocity. The deeper layers have a lower degree of sensitivity, at about ±1 km in depth and ±0.2 km/s in velocity.

A way to evaluate where the model is more and less resolved, is to look at the rayhit density of different areas. The model was divided into cells of 10 km length and 1 km depth. The cells were colored according to the percentage of the total amounts of hits each cell received (Figure 4.5). A cell is considered to be fairly well-constrained if it contains more than 0.25% of the total ray hits (Kandilarov et al., 2008). Bright colored cells show well-illuminated areas of the model with more than 0.25% of the total rayhits, while darker cells show less illuminated areas. The completely black cells have no rayhits at all. From this figure it follows that the sediments, and oceanic crust west of 70 km, are well illuminated, while the remaining crust is less well constrained. The edges of the model and the deep parts are not well resolved.
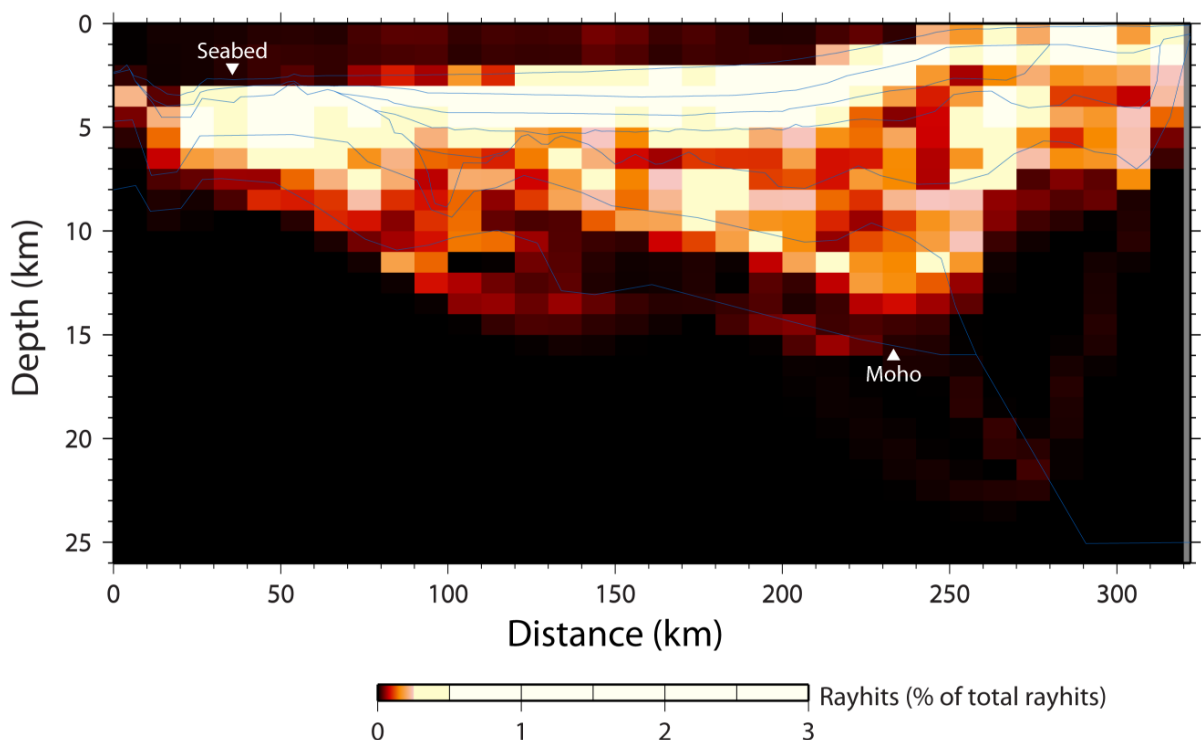
Figure 4.5: Illumination of the model. The model has been divided into cells 10 km long and 1 km deep, and cells are colored according to the number of rayhits. Cells with bright colors have more than 0.25% of the rayhits, and are properly resolved. Cells with orange and red cells are poorly resolved, while black cells have no rayhits at all. The direct wave is not included in this plot.

31

5. Results

5.1. Multi channel seismic data

The multi channel seismic (MCS) profile (Figure 5.1) starts 45 km west of the start of the OBS profile. The quality of the MCS data below the first water layer multiple is very poor. Since the shallow sediments are not the subject of this thesis, the MCS profile will not be described east of the point where the oceanic basement and most of the sediments is obscured by the multiple. This occurs at 200 km along the profile, at a water depth of 1300 m.

The MCS profile can be divided into four parts. The first part is the area west of the Knipovich Ridge, spanning -45 to 5 km on the profile. The area is characterized by rotated basement blocks, delimiting pockets of sediments. The second part comprises the sediment filled axial graben, and runs from 5 km to 25 km. The third part runs from 25 to 80 km, and is characterized by a relatively flat and shallow oceanic basement overlain by sediments. The fourth part starts at the Knipovich Escarpment, a prominent basement escarpment at 80 km, and runs to the end of the interpreted part of the profile at 200 km. The depth to basement is much larger on this part, and the sedimentary package is much thicker.

As a first step of interpretation, the sediments were divided into four units as described in chapter 4 (Figure 4.1).
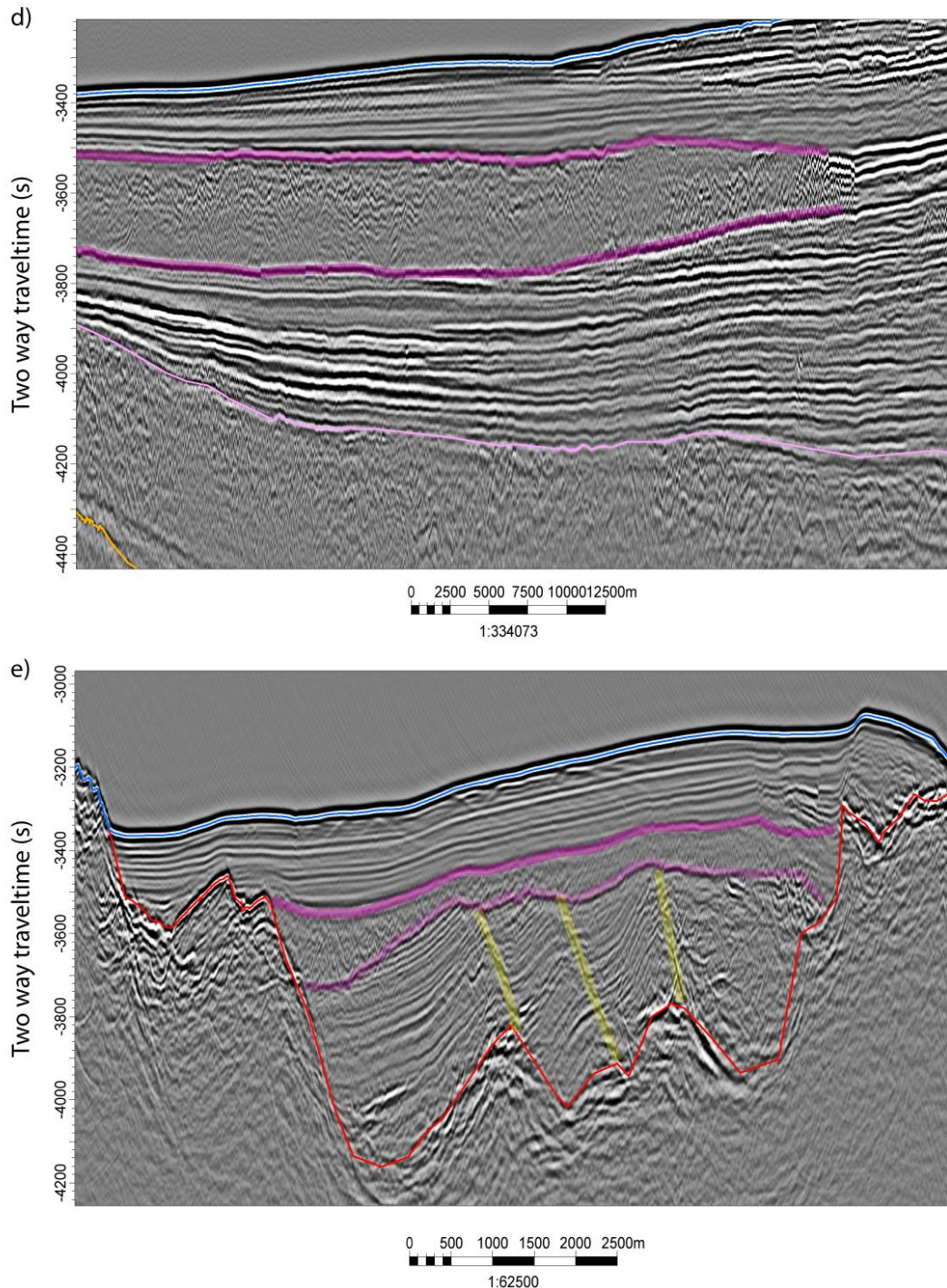
5.1.1. Sediments

When looking at the sediments from east to west, units 1 and 2 appears to be dammed by the Knipovich Escarpment (see figure 5.1a), rising up from 90 to 70 km. Unit 1 lies on the oceanic basement, and thickness variations in this unit appears to be controlled by variations in basement topography. Unit 2 onlaps the oceanic basement at 80 km, and has quite uniform thickness. Unit 3 onlaps the oceanic basement at 70 km, and thins from 90 to 70 km. The unit can be followed to 50 km based on seismic signature, where unit 3 and the lower part of unit 4 are eroded. Unit 4 is thickest near the continent at 200 km, and decreases in thickness westwards. It is continuous all the way to the west edge of the axial graben. Internal reflectors in this package are downlapping the underlying unit 2 from 200 to 85 km.
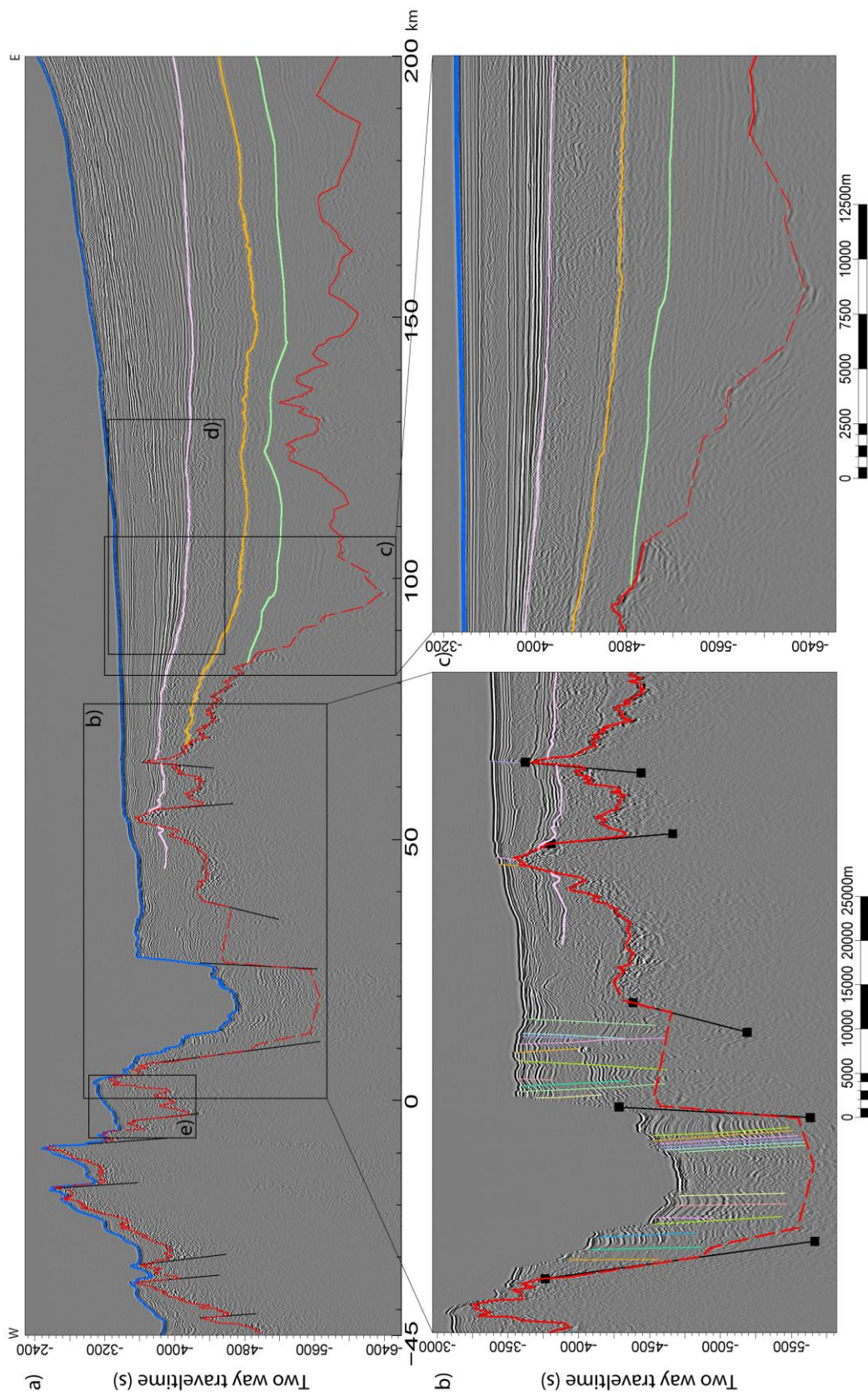
Figure 5.1: Multi channel seisimc data. Horizonz are, from top to bottom, seabed (blue), top unit 3 (pink), top unit 2 (orange), top unit 1 (light green), oceanic basement (red, solid lines represent an obvious acoustic basement, while stippled lines are inferred with support from the OBS modeling). Black lines are faults in the oceanic basement, colored lines are faults in the sediments. a) Entire MCS line. b) Axial graben and basement highs. c) Knipovich Escarpment and overlying sediments.

33

Figure 5.1 (continued): d) Mass flow unit, note the chaotic interval encased in acoustically laminated sediments (dark purple lines). e) The easternmost of the fault bounded basins west of the axial graben. The lowermost sediments (below deepest purple line) are rotated and faulted with the oceanic basement. A chaotic package overlies the rotated sediments (between purple lines), infilling topographic lows and having a relatively flat top. The uppermost laminated package show little deformation.

A chaotic package is observed in unit 4 from 125 km to the west flank of the ridge axis (Figure 5.1d). It has been interpreted as a mass flow deposit. The mass flow deposit is

34

easy to identify from its characteristic chaotic seismic signature, distinguishing it from the acoustically laminated sediments above and below.

The axial graben (5-25 km) and the adjacent area from 25 to 40 km show 1 km thick deposits of sediments with a laminated signature in the bottom, a chaotic signature in the middle, and a laminated signature on top. The sediments therefore probably belong to unit 4 (figure 5.1b). The sediments from 25 to 40 km are faulted by normal faults which dip both east and west, leading to a horst-and-graben-signature, with dips of 45°, offsets of approximately 30 m, and an average fault spacing of 900m. The sediments in the east side of the axial graben are faulted by eastward dipping normal faults with dips of 50°, average fault spacing of 400 m and a throw of 35 m. Directly east of these faults the sediments appear to be folded, and the eastward dipping faults seem to accommodate the folding. The sediments in the west side of the axial graben are faulted by normal faults dipping to the east with typical dips of 43°, very variable offset and average fault spacing of 1.2 km. All these faults intersect the seabed. From this it can be inferred that they have been active recently or are active today.

Two basement highs are present at 55 km 65 km (figure 5.1b). The sediments surrounding these highs show little interaction with the underlying highs, except from small faults directly above the high. From this it can be inferred that the highs were in place before deposition of the sediments. The faults are probably caused by differential subsidence. The western, largest high marks a change from the undeformed sediments east of the high, to the more deformed sediments west of the high. The seabed on the eastern side is also smoother, and at a higher level than the seabed on the west side. It seems that the high have shielded the sediments east of it from deformation due to extension near the axial graben.

West of the axial graben, from -45 to 5 km, sediments lie in four fault bounded basins between rotated fault blocks (figure 5.1a and e). A chaotic unit encased in acoustically laminated sediments, similar to the one observed east of the ridge, is observed in the easternmost sedimentary pocket. The sediments below the chaotic unit appear to be rotated and faulted with fault blocks. The chaotic unit itself appears to fill in the topography of the underlying sediments, while having a relatively flat top. The uppermost laminated unit show little interaction with the underlying rotation. The thickness of the sediments in the pockets are 700 m, 250 m, 150 m and 700 m, from

west to east, assuming the same velocities in the sediments on both sides of the ridge axis.

5.1.2. Oceanic basement

The basement reflector appears as a high amplitude reflector with chaotic signature (see figure 5.1e). From -45 to 5 km, the oceanic basement appears as four rotated fault blocks. The average fault spacing here is 13 km, and the dip is 40° to the east. Beneath the thick, faulted sediments in the axial graben and east flank, it is not possible to identify the top basement reflector. From 35 to 85 km, the basement reflector is clearly visible, and the basement is rough with abundant internal reflections. Two basement highs are present at 55 and 65 km (figure 5.1b), protruding about 940 m over the average basement level in the area. On the same distance from the spreading axis on echo sounder data from the BIN OBS line, which runs approximately 2 km south of the MCS line, a similar high rises to 100 m over the seabed. Thus, it appears that the high is part of a ridge running parallel to the spreading axis.

Eastwards of the Knipovich Escarpment at 85 km, the basement deepens, and the data quality declines (figure 5.1c). From 85 to 110 km, the interpretation is drawn between a few strong reflections. This interpretation is in general in good agreement with top of layer X from the OBS modeling.

In the interval from 110 to 145 km, the basement reflector is clearly identifiable. The reflector appears as series of narrow peaks. Few internal reflectors from the basement are identified. At 145 km the reflector signature changes to a series of broader peaks with abundant internal reflectors. The reflector weakens at 185 km, and is not observed east of 200 km.

5.2 Ocean bottom seismometer data

5.2.1. Velocity model

The final velocity model obtained in the OBS modeling is presented in figure 5.2.
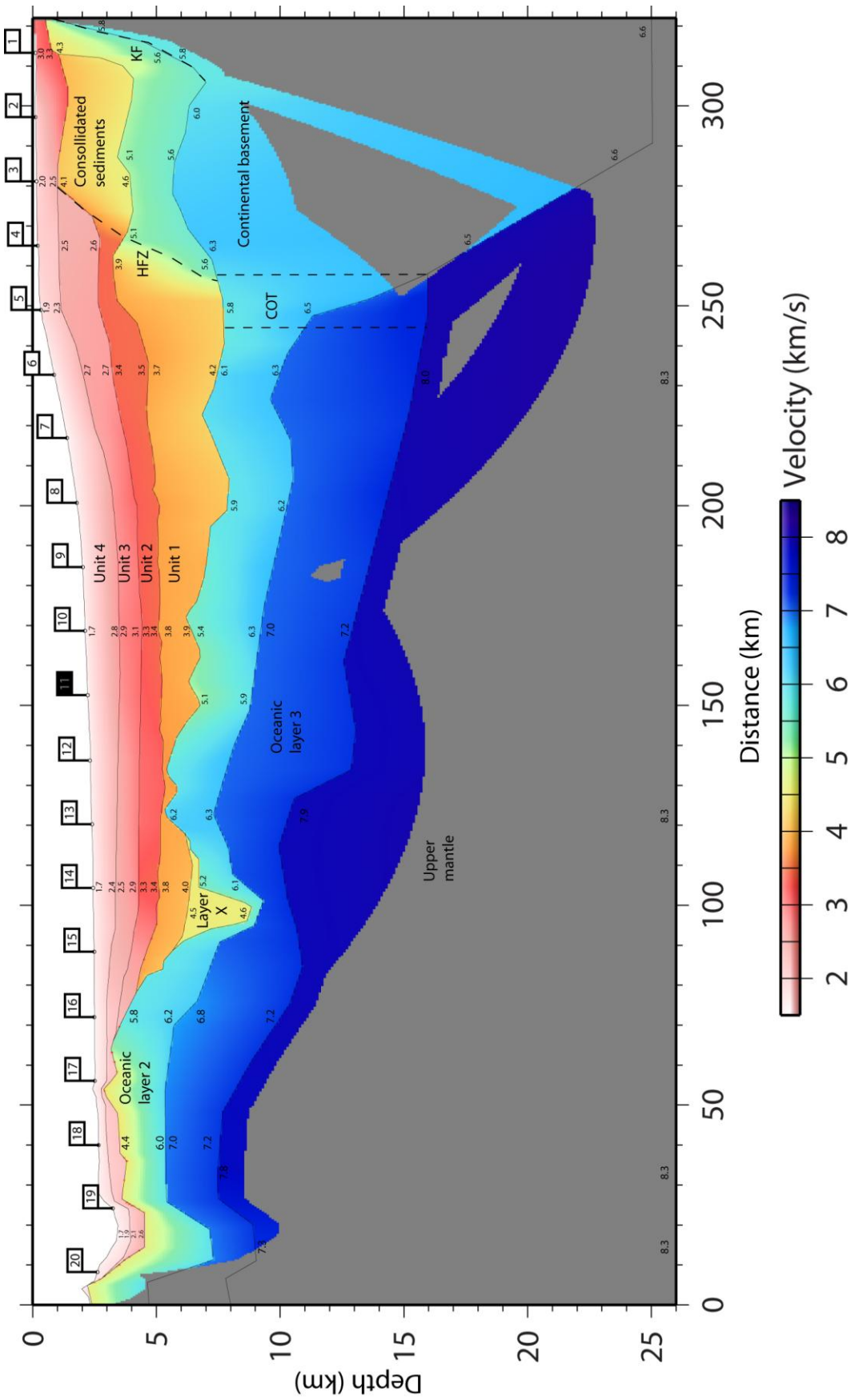
Figure 5.2. Final velocity model. Velocities are given by white flags. OBS positions given by small, black numbers, OBS positions given by white flags. OBS 11 did not acquire useful data, and is drawn as a black flag. Areas without ray coverage are greyed out. HFZ, Hornsund Fault Zone; KF, Knølegga Fault;, COT, continent-ocean transition.

5.2.2. Sediments on oceanic crust, west of the Hornsund Fault Zone

The P-wave velocities in the sediments is well constrained, with arrivals from the sediments on all OBSs from 5 to the east side of OBS 16. Arrivals from the sediments on the westernmost OBSs are masked by earlier arrivals from the oceanic basement. The velocities in this area are therefore extrapolated from sediments of similar depth in the area from 70 to 100 km. Conversion of the velocity model into two-way travel time show a good fit between the observed and modeled oceanic top basement. The velocities in the sediments in this area are therefore believed to be reasonably correct.

The velocity in the sediments directly below seabed is around 1.7 km/s in the deep ocean and continental slope areas. On the continental shelf from 250 to 280 km, the velocities in the seabed are about 2 to 2.1 km/s. On the oceanic to continental slope parts of the profile, the sediments are divided into four units. The two uppermost units have a strong velocity gradient of about 0.8 s^{-1}. The two lower sedimentary units show lesser gradients, 0.2 s^{-1} for unit 2 and less than 0.1 s^{-1} for unit 1. Average velocities in the layers are 3.9, 3.4, 2.8 and 2.1 km/s for units 1, 2, 3 and 4, respectively. The sediment thickness increases landwards, and reaches a maximum of almost 8 km at 250 km.

5.2.3. Oceanic crust

The crystalline crust in the oceanic domain of the model has been divided into oceanic layers 2 and 3. No evidence of further partitioning of layer 2 into layers 2A, 2B and 2C and layer 3 into layers 3A and 3B was found in the data. However, an additional layer was introduced to explain arrivals in the area between 90 and 105 km, east of the Knipovich Escarpment. This layer is needed to explain an arrival with high apparent velocity and high traveltime on OBS 14, and a long, straight arrival with intermediate apparent velocity on OBS 15 (Figure 5.3). The velocity in the top and bottom of this layer is 4.5 and 4.6 km/s, and the velocity gradient is 0,3 s^{-1}. This layer is assumed to be a part of the oceanic layer 2 in this chapter, because the velocities are more in accord with the observed velocities of oceanic layer 2, and because of the relatively clear reflectors defining the top of this layer in the MCS data is at the same level as the surrounding oceanic basement. This layer will be referred to as layer X., and the origin of the layer will be discussed in the next chapter.

The depth, thickness and top layer velocity of each layer has been plotted in figure 5.4, along with the total thickness of oceanic crystalline crust. Oceanic layer 2 has a near

constant thickness of 2 km along most of the profile, with an increased thickness from 10 to 20 km near the ridge axis, east of the Knipovich Escarpment from 95 to 105 km, and with gradually increasing thickness from 2 to 3 km from 110 km to 170 km offset.
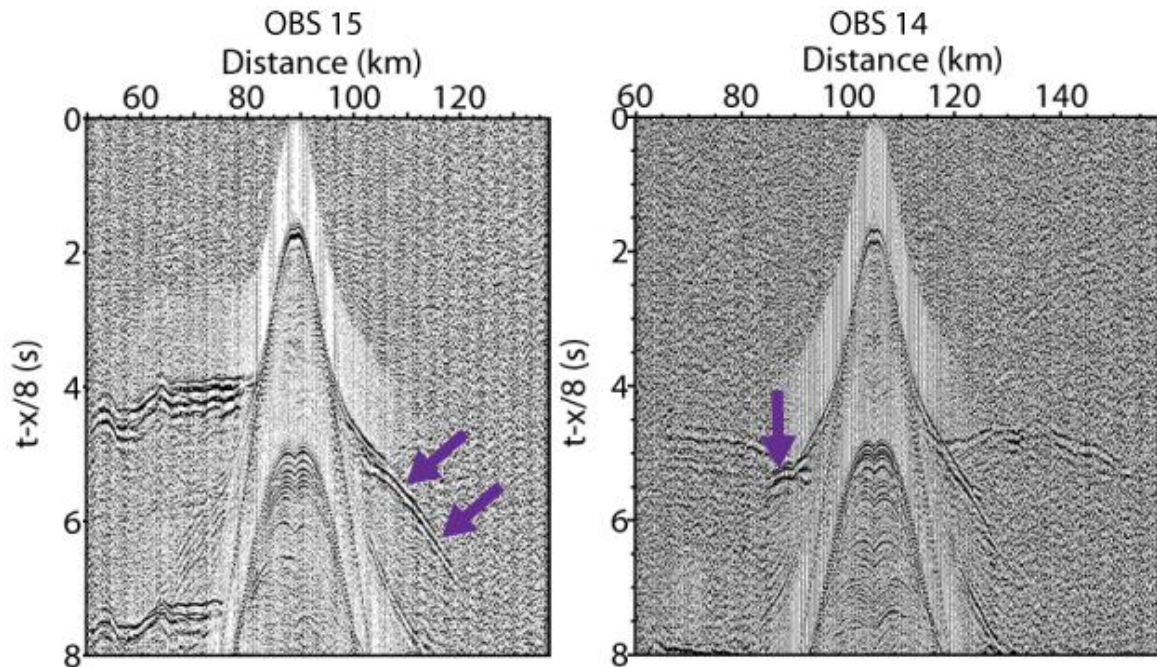

Figure 5.3. OBSs 14 and 15. The low-velocity layer from 90 to 110 km is required to explain the two arrivals marked with purple arrows.

The thickness of oceanic layer 3 is more variable than for oceanic layer 2, and it can be divided into six domains. The first domain goes from 0 to 50 km, and has a thickness of 2 km. In the next domain, from 50 to 90 km, the thickness increases to about 4 km. The increase in thickness is accommodated by a deepening of the Moho. The third domain, from 90 km to 120 km, is characterized by a dramatic thinning of oceanic layer 3. The thickness decreases rapidly from near 4 km to below 2 km. In the end of the domain, the thickness increases to slightly more than 2 km. The fourth domain runs from 120 km to 150 km and contains a dramatic increase in thickness from about 3 km to 5 km. The fifth domain, from 150 km to 210 km, has a relatively stable thickness of around 4 km. The final domain, from 210 km to the COT at 250 km, is similar to domain 4, with a thickness that reaches almost 6 km.

The total thickness of the crystalline oceanic crust is about 4 km from the axial graben to 50 km, 6 km from 50 km to 80 km, 4 km from 90 to 120 km, peaks at 7.5 km at 130 km

before it decreases to 7 km from 160 km to 210 km. From 230 to 250 km, the thickness of oceanic crust is at a maximum of 8 km. The thickness is primarily controlled by variations in oceanic layer 3.
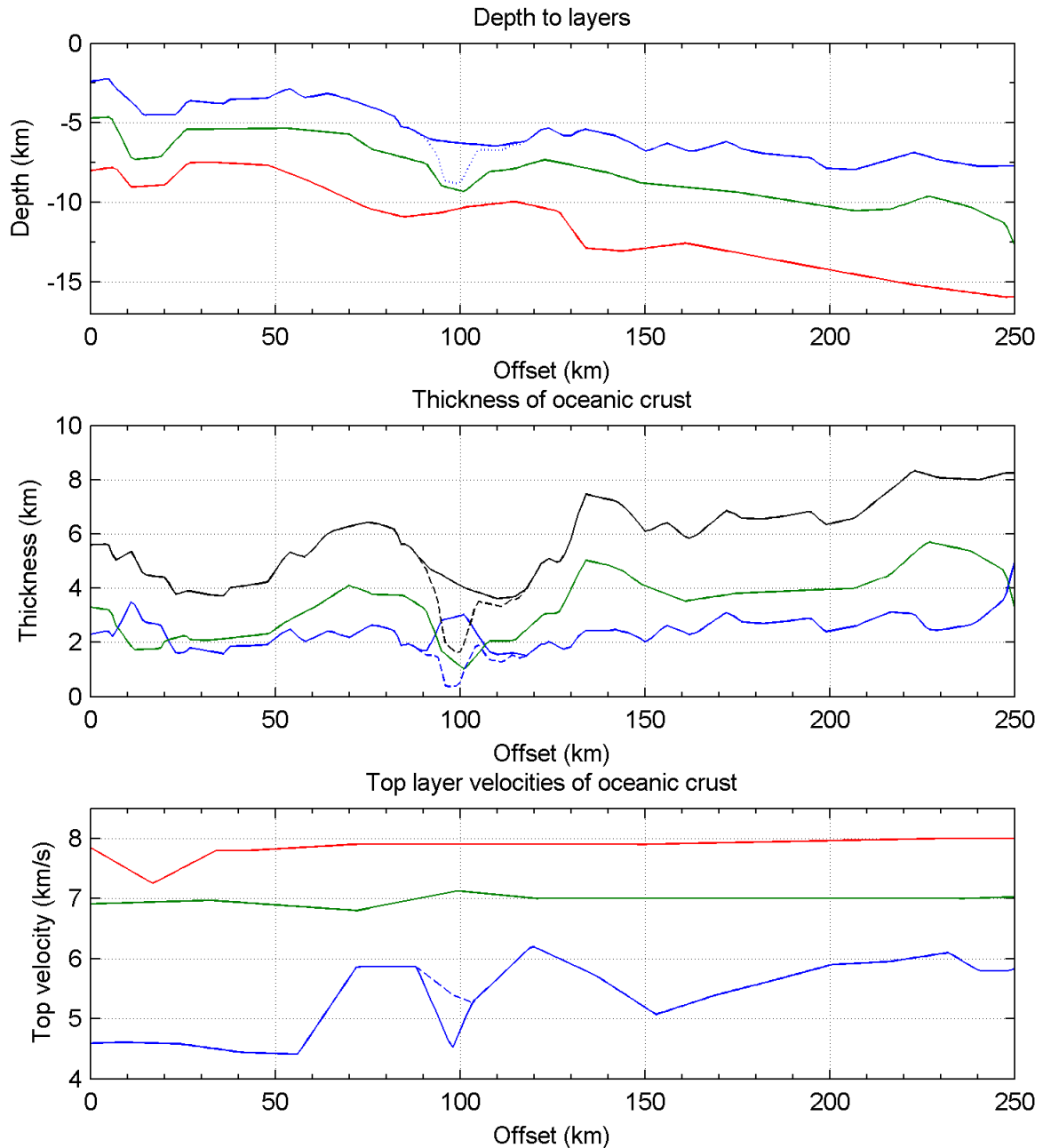
Figure 5.4: Properties of oceanic crustal layers and upper mantle. Plots of depth to interfaces (upper), thickness of crustal layer (middle), and top layer velocities (lower). Blue line is oceanic layer 2, green is oceanic layer 3, red is upper mantle and black is the total oceanic crystalline crust. Solid lines assume layer X as a part of the oceanic layer 2, stippled lines assume layer X as part of the sediments.

The velocity of oceanic layer 2 appears to approximately follow the same domains as the thickness of oceanic layer 3. From 0 to 60 km, the velocity is around 4.4 km/s, with a strong velocity gradient of 0.85 s^{-1}. From 60 to 70 km, the velocity increases drastically from 4,4 km/s to 5.9 km/s. This high velocity is continued until 90 km. This interval has a much lower velocity gradient of 0.1 s^{-1}. The area around 100 km is characterized by a dramatic drop in velocity to 4.5 km/s. From 105 to 120 km, the velocity increases rapidly to 6.2 km. The high velocity-interval has a velocity gradient of 0,02 s^{-1}. After this peak, the velocity decreases westwards to 5.1 km/s at 155 km. From 155 km, the velocity rises steadily towards a value around 6 km/s at the COT. The velocity gradient is ca 0.4 s^{-1} from 150 to 190 km, and 0.1 s^{-1} from 190 to 250 km.

The velocity of oceanic layer 3 shows very small variations, mostly within the sensitivity of the model. For the majority of the model, the best fit for oceanic layer 3 was acquired using a velocity of 7.0 km/s in the top, and a velocity of 7.2 km/s in the bottom. Around 70 km, a slight decrease in the velocity on top of layer 3 to 6.8 km/s gave best fit to the observed arrivals.

5.2.4. Continental crust
From the Hornsund Fault Zone at 280 to 300 km, the velocity in the sediments directly below the seabed is 2 km/s. Velocities as high as 3 km/s have been recorded close to the seabed On OBS 1, and the velocity in the bottom of the uppermost sedimentary layer is 3.3 km/s here (Figure 5.2).

A strong velocity discontinuity is observed from 1 km depth at 280 km to 7.5 km depth at 250 km. It lies where the Hornsund Fault Zone is expected (Gabrielsen et al., 1990), and the velocity discontinuity is probably a manifestation of this fault zone (see figure 3.1). The increase in velocity is at least 1 km/s from west to east. It seems that the sedimentary units 1-4 terminate against this discontinuity.

From 1 km depth at 322 km offset, to 7 km depth at 305 km, another velocity discontinuity has been observed. The discontinuity is observed on OBSs 2-4 as arrivals having apparent velocities relatively close to 6 km/s when propagating eastwards, then changing apparent velocity to well above 8 km/s at around 310 km offset. This has been modeled as head waves propagating up a shallowing of the basement. The discontinuity

appears where the Knølegga Fault is expected (Gabrielsen et al., 1990), and is therefore inferred to represent this fault (see figure 3.1).

Beneath the upper sedimentary layer, the area between the two fault zones has been modeled as two layers. The upper layer is 2.5 km thick, and has top and bottom velocities of 4.1 and 4.6 km/s, giving a velocity gradient of 0.2 s^{-1}. The lower layer is 2.5 km thick, and has top and bottom velocities of 5.1 and 5.6 km/s, giving a velocity gradient of 0.2 s^{-1}. The velocity gradient increases eastwards of 310 km, especially in the upper layer.

The continental basement is represented by the layer directly above the mantle from 250 km to the end of the profile. This layer is not very well constrained by the OBS modeling (Figure 4.5). Rays from OBS 1, 2, 3 and 4 are traced through the upper few kilometers, but the lower part is only illuminated by a few rays from OBS 1. It has been modeled with velocities around 6 km/s from 250 km to the Knølegga Fault at 310 km. The velocity in the bottom is set to 6.6 km/s, giving a velocity gradient of 0.03 s^{-1}. Where the layer shallows due to the Knølegga fault, the top layer velocity has been decreased to 5.8 km/s. A slight increase in top layer velocity to 6.3 km/s has been observed around 265, which may be related to intrusions under breakup.

5.2.5. Upper mantle

The upper mantle is not sampled by rays at all beneath the continental part of the profile. Therefore, the depth to Moho east of 260 is entirely based on earlier studies (Czuba et al., 2010; Ebbing et al., 2007; Ritzmann et al., 2007) and the shape is defined by gravity modeling. West of 260 km, the top of the mantle is constrained by diving waves modeled from observations on OBS 1 and OBS 16, and head waves from most OBSs except from OBS 1 to OBS 7. No top mantle reflections were found in the data.

The velocity in the top of the mantle was found to be 7.25 km/s below the axial graben, increasing to 7.8 km/s at 34 km. From 34 km to 230 km, the velocity increases gradually from 7.8 km/s to 8 km/s. From 230 to 275, a velocity of 8 km/s in the top of the mantle fits the data well. No rays are traced in the mantle east of 275 km.

5.2.6. Continent-Ocean boundary

The continent ocean transition (COT) has been defined as an area of rapid crustal thinning out to undisputable oceanic crust (e.g. Breivik et al., 2003). From the OBS

model, the COT is located between 245 and 260 km, where the oceanic layer 3 terminates against continental crust. The seismogram from OBS 5 shows a clear difference between the east and west side (figure A.5), where the western side shows an arrival similar to the other arrivals on the oceanic crust, while the arrivals on the eastern side show that higher velocities must be located much shallower.
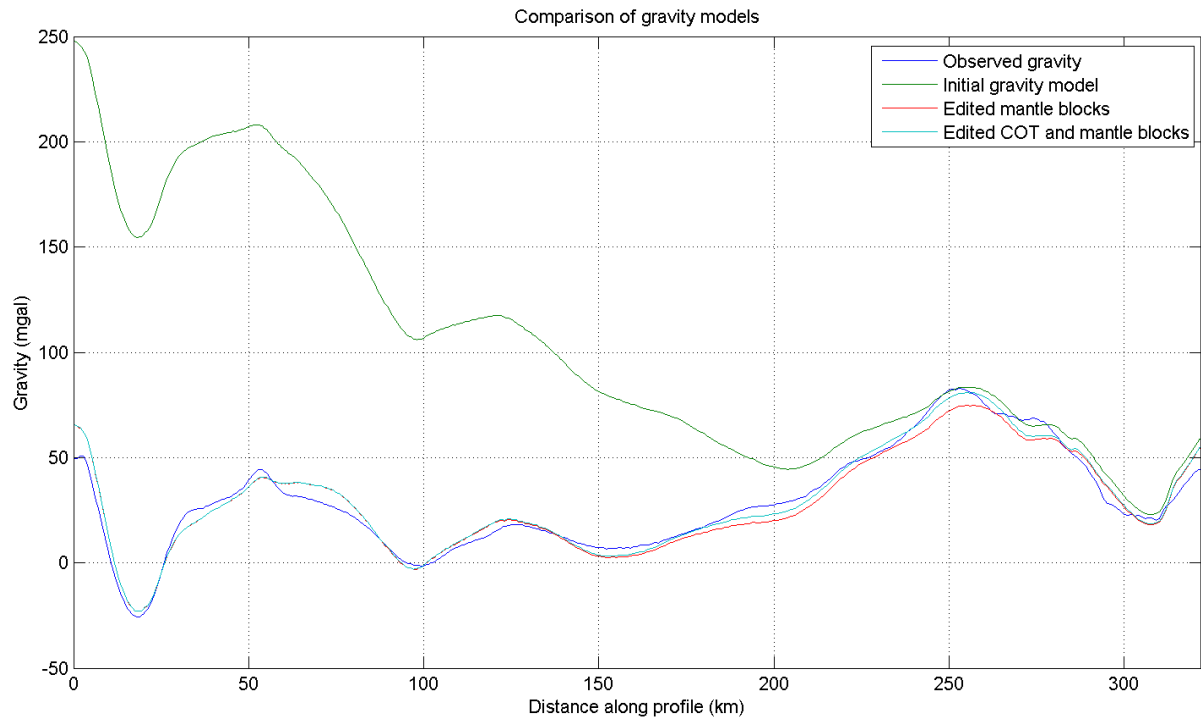
5.3. Gravity modeling

The final density model is presented in figure 5.5.

An initial gravity model with densities in the crustal parts as given by Carlson and Raskin (1984) and the Nafe-Drake curve (Ludwig et al., 1970) was created as described in chapter 4. Densities in the mantle were set to 3.33 g/cm^3, corresponding to the density of rock with a P-wave velocity of 8 km/s (Ludwig et al., 1970). The calculated gravity was then anchored to the observed gravity over the continental part of the crust. It was not possible to obtain a fit between calculated and observed gravity without decreasing the density in the mantle beneath the oceanic crust, so the mantle was divided into three blocks, in which the densities were adjusted until a reasonable fit was obtained. The density of the mantle blocks is set to 3.07, 3.17 and 3.33 g/cm^3 from west to east. The fit between calculated and observed gravity was further improved by raising the density of the block in the lower continental crust at the COB (240 to 265 km) from 2.85 to 2.89 g/cm^3. The fit of these three steps in the gravity modeling is presented in figure 5.6.
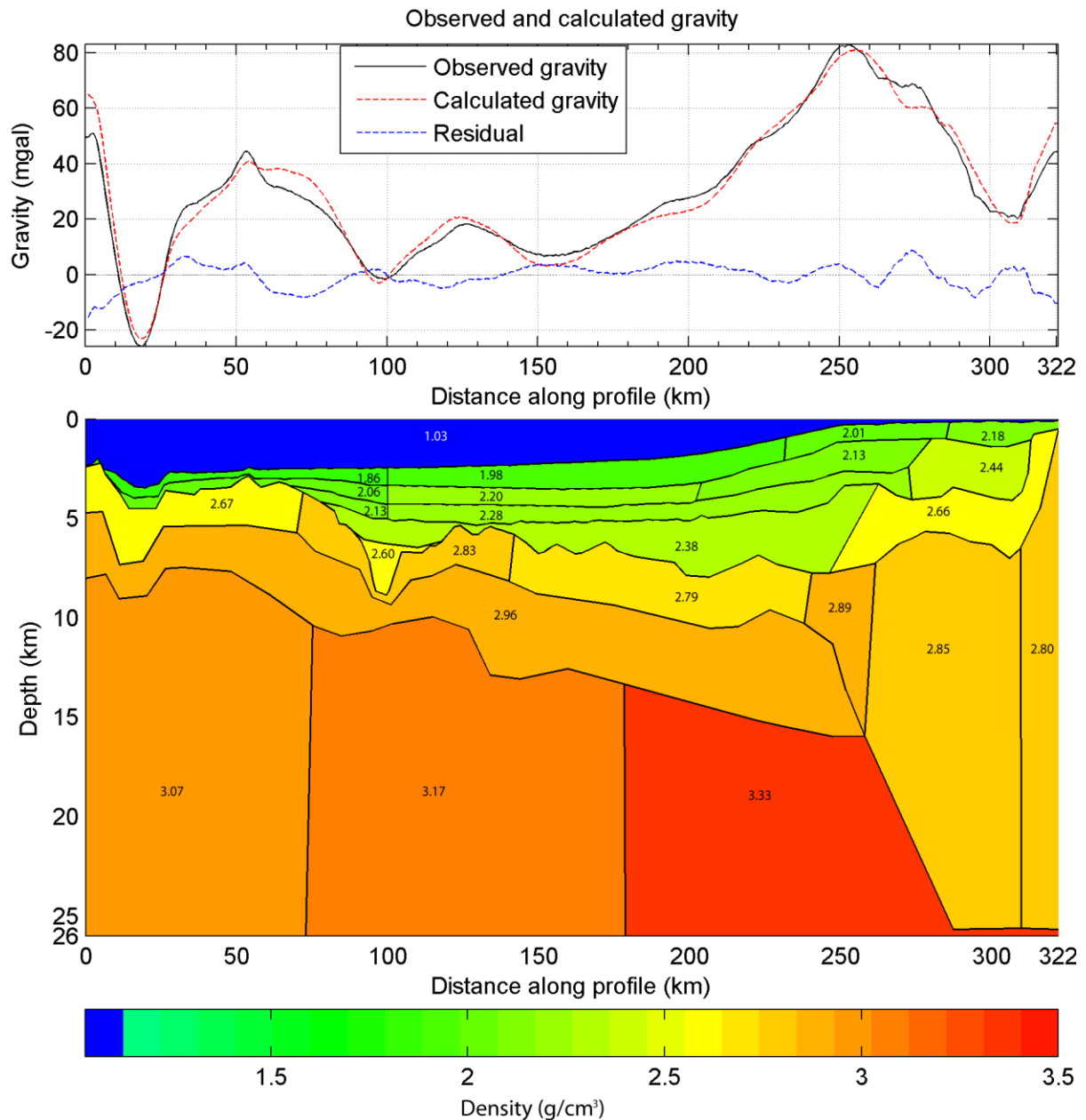
Figure 5.5: Final gravity model for the BIN profile. Observed gravity (black), calculated gravity from the gravity model (red stippled line) and residuals (blue stippled line) in upper plot; density model in lower plot. Density values in g/cm³.

The values of the density in the mantle blocks should not be taken as literal values of density in the upper mantle, but rather as an indication of the relative density of the mantle blocks. This will be discussed further in the next chapter.

44

Figure 5.6: Comparison of gravity models. Observed free air anomaly (black), initial gravity model with density of 3.33 g/cm³ in all upper mantle blocks (purple), gravity model with adjusted mantle blocks (blue), gravity model with adjusted mantle blocks and increased density in lower crust at COT (blue).

6. Discussion

6.1. Post-opening sediments

6.1.1. Correlation to established stratigraphic network

Access to good quality seismic data crossing the OBS and MCS profile was not acquired when working on this thesis. For this reason, correlation to the established seismic stratigraphic network by Faleide et al. (1996) will be performed by distinguishing seismic facies.

Sequence G0 is characterized by discontinuous parallel to sub-parallel reflectors, and is bounded by the basement and reflector R7. In the middle part of the Storfjorden Fan, sequence GI is dominated by hummocky reflectors up to 3 km wide and 300 m thick separated by continuous reflectors between R7 and R6, while it is characterized by continuous and parallel reflectors on the distal fan from R6 to R5. Sequences GII and GIII are characterized by continuous reflectors on the distal fan, and a discontinuous and chaotic configuration within the upper slope (Hjelstuen et al. 1996).

In this thesis, the sediments were divided into four units, units 1-4. The two lowermost units are characterized by parallel to subparallel, moderately continuous to discontinuous reflectors. This is similar to the description of G0. Units 1 and 2 therefore probably belong to the preglacial sequence G0.

Unit 3 is characterized by a chaotic to hummocky appearance with moderate amplitude discontinuous reflectors. The lower boundary is defined by a strong, continuous reflector, and the upper boundary is defined as a transition to parallel continuous reflectors. This is similar to the interval from R7 to R6 in GI, and the bottom and top of unit 3 therefore defines reflectors R7 and R6.

Unit 1 is composed of parallel continuous reflectors with local chaotic packages. No obvious candidate for the reflector R5 is observed, and it is concluded that unit 1 consists of sediments younger than R6.

East of 200 km the boundaries between sedimentary units are based on the OBS modeling alone. It is likely that the stratigraphic boundaries are somewhat independent from the velocity boundaries found in the OBS modeling, and the correlation to the

stratigraphic network from Faleide et al. (1996) is therefore not necessary valid east of 200 km. However, converting the velocity model into two way traveltime and comparing it with the seismic line F-F' from Faleide et al. (1993) shows relatively good agreement with the MCS data from 200 km to 250 km (Figure 6.1). The boundary found in OBS modeling does not shallow east of the shelf edge, but remains at an almost constant depth. This indicates that the velocity structure of the sediments is not a function of stratigraphy, but rather a function of depth.
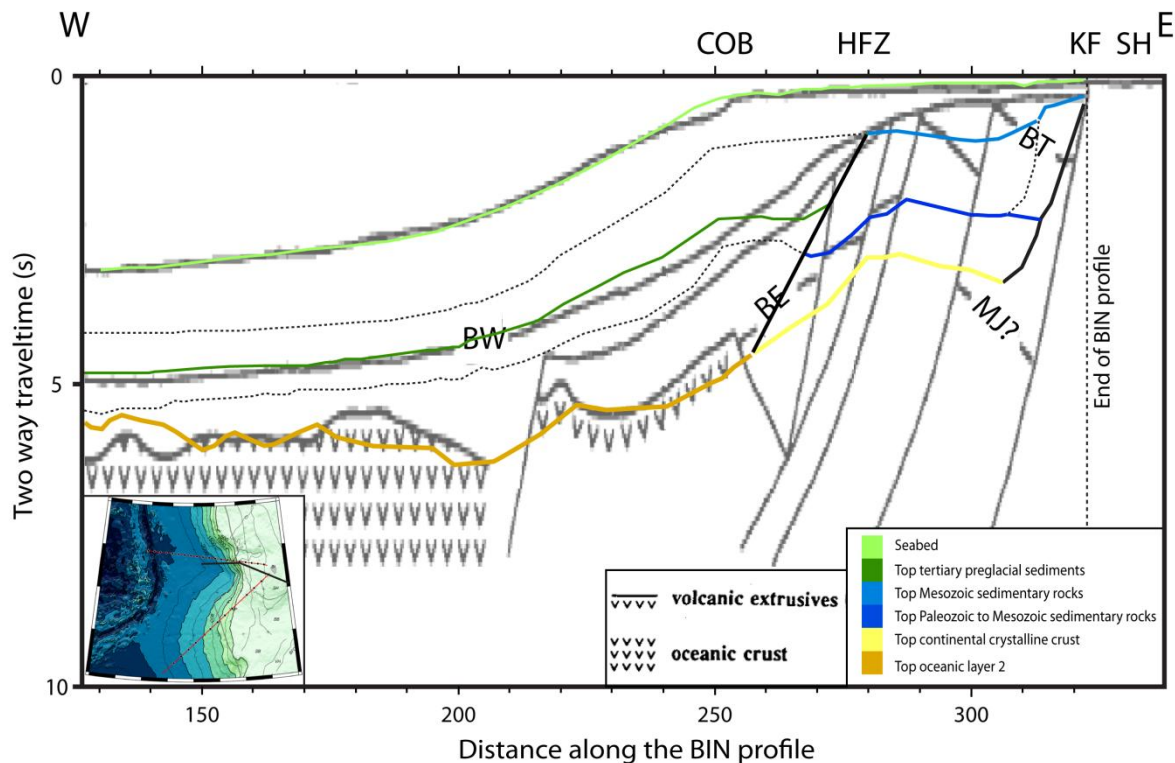
Figure 6.1: Boundaries from the OBS modeling transformed from depth to two way traveltime overlain an interpretation of the composite MCS line F-F' from Faleide et al., 1993. Locations of the lines are shown in the inset map, BIN and BIS lines (red), composite line from Faleide et al. 1993 (black). The distance between the lines is approximately 20 and 25 km in the east and west end, and 0 km at 250 km. Annotations on top of the figure are the location of structural elements from this study. COB, Continent-Ocean Boundary; HFZ, Hornsund Fault Zone; KF, Knølegga fault; SH, Stappen High. Annotations in the figure itself are from Faleide et al. (1993). BE, Base Eocene; BT, Base Tertiary; BW, Base Plio-Pleistocene Wedge; MJ?, possible top of Middle Jurassic seismic marker. Modified from Faleide et al. (1993).

6.1.2. Velocities in the sediments

The low velocities (1.7 km/s) near the seabed on the abyssal plain and continental slope are typical for shallow, unconsolidated sediments (e.g. Breivik et al., 2003). The somewhat elevated velocities (2.0 - 2.1 km/s) from the shelf edge to 300 km are

probably related to increased overburden and subsequent consolidation and possibly erosion due to glaciers reaching the shelf edge in the Plio-Pleistocene (e.g. Ottesen et al., 2005).

The significantly higher velocities (3 km/s) east of 300 km indicate that the sediments here are more consolidated, and probably represent tertiary sediments. Velocities of 3 km/s correspond to a depth of ca. 1.8 km using the proposed velocity-depth relationship for the eroded rocks in the Storfjorden fan drainage area suggested by Hjelstuen et al. (1996). This may indicate erosion in the order of 2 km in this area.

The thickness of the post-opening sediments on the oceanic crust reaches a thickness of 7 km between the shelf edge and the COB, which is in good agreement with the results from Hjelstuen et al. (1996). The base of the glacial sediments (GI-GIII) lies at a depth of 4.5 km from 100 to 200 km, also in accordance with Hjelstuen et al. (1996).

6.1.3. Tectonic constraints from the sediments

The chaotic unit identified from 120 km to the axial graben has been correlated to the chaotic sediments in the westernmost sedimentary pocket east of the axial graben (figure5.1d). The sediments in this pocket therefore probably belong to unit 4, and are therefore younger than R6 time, which corresponds to 1.3-1.5 Ma (Butt et al., 2000). If this is correct.

Bruvoll et al. (2009) reported that almost all tectonic activity after 1.3 Ma in their study area in the northern part of the Mohn-Knipovich spreading ridge bend happened on the western side. This is not the case on this profile, evidenced by the numerous faults and horst-and-graben-structures in the sediments on the eastern side of the axial graben, and the faults in the sediments in the east and west sides of the axial graben (Figure 5.1b). All these faults intersect the seabed, and must therefore have been active recently. West of the axial graben, no faults appear to cut through the upper two packages of unit 4, the chaotic package, and the upper laminated package.

The fold-structure observed in the east side of the axial graben (figure 5.1b) could be caused by compression due to developing rotation of a fault block overlain by the thick sediments in the eastern side of the axial graben.
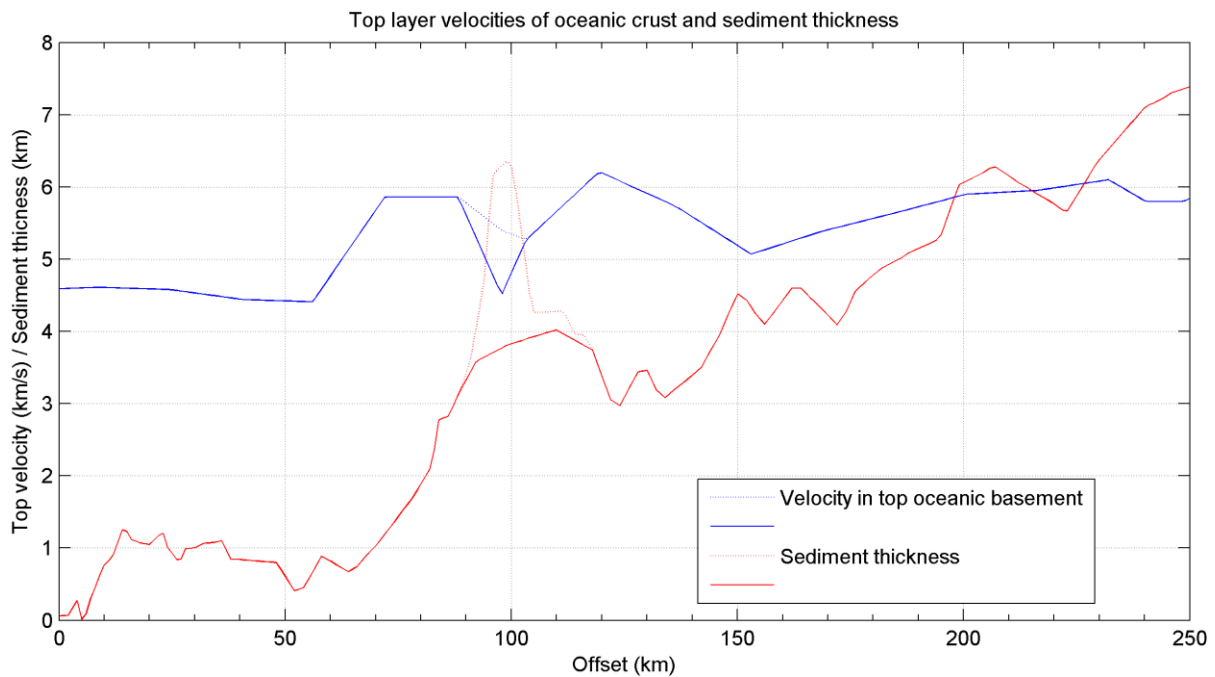
6.2. Oceanic crust

6.2.1. Near the ridge (0-60 km)

The modeled P-wave velocities in oceanic layer 2 are relatively low close to the ridge compared to the rest of the profile (Figure 5.2). The velocity is 4.4 km/s in top of the layer from 0 to 60 km, but increases to 5.8 km/s at 70 km. The increase in velocity in the bottom of the layer over the same distance is only 6.0 to 6.2 km/s, which means the gradient is much larger to the west.

An increase in the seismic velocity of oceanic layer 2 with increasing distance to the spreading axis is commonly observed on oceanic crust (Jacobson, 1992). This increase is attributed to a decrease in porosity of the extruded basalts due to the filling of cracks by hydrothermally generated minerals and by closing of microcracks due to increased sedimentary overburden (Jacobson, 1992). Because pores with low aspect ratio ("flattened" pores) have the dominant control on velocity, a small decrease in porosity can lead to a large increase in seismic velocities (Wilkens et al., 1991).

On this profile, the velocity in top of oceanic layer 2 close to the ridge axis (4.4 km/s) is higher than velocities found close to the axis on other profiles over the Knipovich Ridge. Kandilarov et al. (2008) reported a velocity of 2 km/s in top of the oceanic layer 2 close to the ride axis, and Ljones et al. (2004) found velocities of 3.55 km/s near the ridge axis. This difference is attributed to the thicker sedimentary cover over this part of the Knipovich Ridge. From the ridge axis to 70 km along the line, the thickness of the sedimentary overburden is approximately 1 km (figure 6.2).

To a certain degree, the velocities of the top oceanic basement seem to be correlated to the thickness of the sedimentary overburden (Figure 6.2). However, the decrease in velocity between 90 and 105 km, the peak at 125 km and the decrease from 125 to 155 km cannot be explained from the sedimentary thickness alone. Also the dramatic increase in velocities in top oceanic layer 2 from 55 to 70 km appears to happen west of the increase in sediment thickness. Since these changes seem to be correlated to changes in the crustal thickness, these velocity variations are probably caused by variations in the structure or composition of the oceanic crust (Figure 5.4).

Figure 6.2: Velocity in the top of the oceanic basement (blue), and thickness of sediments overlying the oceanic crust (red). Solid lines assume layer X as a part of the oceanic basement, and stippled lines assume layer X as sedimentary rocks.

6.2.2. Around the Knipovich Escarpment (60-125 km)

The oceanic crust from 60 km to the Knipovich Escarpment at 85 km is characterized by thick crust and high velocities in the top of oceanic layer 2. The oceanic crust directly east of the escarpment from 90 to 110 km has been modeled with three layers: an upper layer with an average velocity of 4.6 km/s, a thin (0.3 km) middle layer with an average velocity of 5.6 km/s, and an oceanic layer 3 thinner than in the rest of the profile (ca 1.5 km). From 110 km to 125 km, the upper layer is very thin, underlain by a layer that appears to be thin oceanic layer 2 and 3. The thin oceanic layer 3 here is accompanied by a shallowing of the Moho. The upper layer have been mentioned before in this thesis as layer x.

Two explanations are proposed to explain the Knipovich Escarpment, the low velocity layer and shallowing of the Moho east of the escarpment. In the first model the Knipovich Escarpment is explained to represent a detachment fault formed at a period of low magma supply and intense stretching on the Knipovich Ridge. It has been suggested by Cannat (1993) that oceanic crust generated at magma-poor spreading ridges may be composed of a thin basaltic upper crust and a lower layer made up of gabbroic intrusions within mantle peridotites which may be serpentinized. Ljones et al.

50

(2004) found elevated velocities in the oceanic crust assumed to be generated at amagmatic segments on the Knipovich Ridge, supporting the interpretation that the crust consists of mantle-derived rocks. However, results from Kandilarov et al. (2008) indicate that crust generated at amagmatic segments of the Knipovich Ridge can be variable, with variations between crust that appears to be of predominantly magmatic origin, and crust of amagmatic origin. This profile does not cross the traces of any prominent magmatic segments before 170 km (Okino et al, 2004).

The crust on both sides of the low velocity layer is characterized by high velocities in the top of the layer and a low velocity gradient (Figure 5.2), which is similar to the crust proposed to consist of mantle derived crust with gabbro intrusions by Ljones et al. (2004). The thin crust from 90 to 125 km can be a result of low magmatic activity and a large degree of stretching, both at the time of generation of the crust, and later. The shallowing of the Moho beneath this interval resembles the early stages of a developing oceanic core complex (Tucholke & Lin, 1994). Magmatic spreading was probably reestablished before an exposure of the Moho was achieved. It is possible that the low-velocity layer consists of highly faulted and fractured oceanic crust deformed by the devolpment of a detachment fault.

It is also possible that the Knipovich Escarpment marks a fully developed oceanic core complex, where serpentinized mantle rocks are present beneath the sediments from 70 to 90. The high velocities after east of 60 km can therefore be explained as exposures of exhumed oceanic layer 3 crust. However, the thickness of the modeled oceanic crust is difficult to explain from this hypothesis.

However, it is expected that faults on the eastern side of a spreading ridge should dip westwards (e.g. Tucholke and Lin, 1994), but the proposed detachment fault dips to the east. The detachment fault may also have developed after the spreading in a weak zone, due to the extension in the area. A similar, eastward-dipping fault was suggested on the western side of the Knipovich Ridge by Kandilarov et al. (2008), based on modeling of floating reflectors in the upper mantle. It is therefore possible that this zone.

Another explaination for the Knipovich Escarpment and surrounding crust is a ridge jump. Ridge jumps on the Knipovich Ridge have been suggested by several authors to explain the Knipovich Escarpment (e.g. Sundvor and Eldholm, 1979; Eldholm et al.,

1990; Breivik and Mjelde, 2001). The proposed jump occurred at anomaly 5 time (9.8 Ma), when an older axis located in the Boreas Basin went extinct, and the spreading jumped to the present ridge. However, this suggestion is speculative because of the poorly defined magnetic anomalies in the area and because no extinct axis has yet been located.

According to Sclater et al. (1971) the depth to the top oceanic basement is a function of age of the crust. The reason for this is that a newly generated portion of an oceanic crustal plate will be hot and thermally expanded. As the portion moves away from the spreading ridge, the crust and lithosphere will cool and therefore contract. Thus, an age discontinuity in oceanic crust will manifest itself as a basement escarpment.

The distance from the Knipocivh Ridge axis to the center of the Knipovich Escarpment is ca 70 km on this profile, which corresponds to an age of ca 10 Ma assuming constant spreading rate and correcting the spreading rate for the angle between the profile and the spreading direction. If a ridge jump leads to oceanic crust of an age of 10 Ma to be juxtaposed with oceanic crust of 20 Ma age, the resulting escarpment should be 400 m tall according to the calculations by Sclater et al. (1971). The Knipovich Escarpment marks a change in basement depth of almost 3 km on this profile, much more than what can be explained from any realistic age differences of oceanic crust in the Norwegian-Greenland Sea. Still, it is possible that an initial escarpment was created by a ridge jump, and the escarpment acted as a dam for sediments. As weight of sediments increased on the crust east of the escarpment, this crust subsided while the crust west of the escarpment did not. In order to decouple the crust east and west of the escarpment, a fault must be present. This fault probably developed at the junction between old and new crust.

The ridge jump model is also able to explain the low velocity layer and the shallowing of the Moho. In order to change the location of the spreading ridge, the existing oceanic crust is stretched until a rupture is created. This probably led to stretching and thinning of the crust, which was accommodated by a shallowing of the Moho. The low velocity interval is probably related to fracturing induced by the breakup of oceanic crust and subsequent faulting.

However, the oceanic crust at this profile does not appear to follow the age-depth relationship from Sclater (1971), as the basement from the ridge axis flank to the Knipovich Escarpment lies at an almost constant depth of 3.5 km for an interval of 55 km, corresponding to 10 Ma. This corresponds to 10 Ma using a spreading rate corrected for the obliquity of the profile.

It is difficult to choose between these two models from this dataset, and no such attempt has been made. Nevertheless, all of these models include a fault at the Knipovich Escarpment. It is likely that no displacement occurred on this fault after the deposition of the glacial sediments, because no faults are observed in the sediments in this area.

6.2.3. Thicker oceanic crust (125-250 km)

Plate tectonic reconstructions show that oceanic crust was generated in the releasing bend north of Bear Island even before the change in spreading direction of the Arctic Ridges at anomaly 13 time (35.5 ma) (Engen et al., 2008). Flowlines from Engen et al. (2008) are presented in figure 6.3. The kink in the flowlines related to the spreading direction change corresponds to approximately 160 km along this profile, indicating that crust east of 160 km was generated between breakup and anomaly 13. From this dataset it is not possible to determine if the spreading in this interval happened at the same ridge as today or if the change in spreading direction was accompanied by a ridge jump. However, the spreading direction would be highly oblique to the trend of the ridge if the ridge had the same orientation as today.

The oceanic crust generated at spreading ridges with a spreading rate lower than 20 mm/a should be thinner than 6 km because of reduced magma generation due to conductive cooling of the lithosphere (White et al., 1992). The thickness of oceanic crust from 130 to 250 km ranges from 6 to 8 km, which is thicker than expected for crust generated at a slow to ultraslow spreading ridge. It is possible that the ridge in this area was supplied more magma than usual because of the proximity to the Vestbakken Volcanic Province. Faleide et al (1988) identified two major volcanic episodes in the Vestbakken Volcanic Province, the first in the early Eocene, the latter in early Oligocene, corresponding to the start of seafloor spreading in the Norwegian-Greenland Sea and the change in spreading directions on the Arctic ridges. The oceanic crust from 220 to 250 km is especially thick, with a thickness of 8 km. The results from the OBS modeling performed in this thesis show that the crust in this interval most likely is oceanic crust,

as it has a typical oceanic layer 2 and 3 velocity structure (Figure 5.2). The increased thickness is most likely caused by increased magma supply due to the proximity to the Vestbakken Volcanic Province during its most active phase in early Eocene (Faleide et al., 1988).
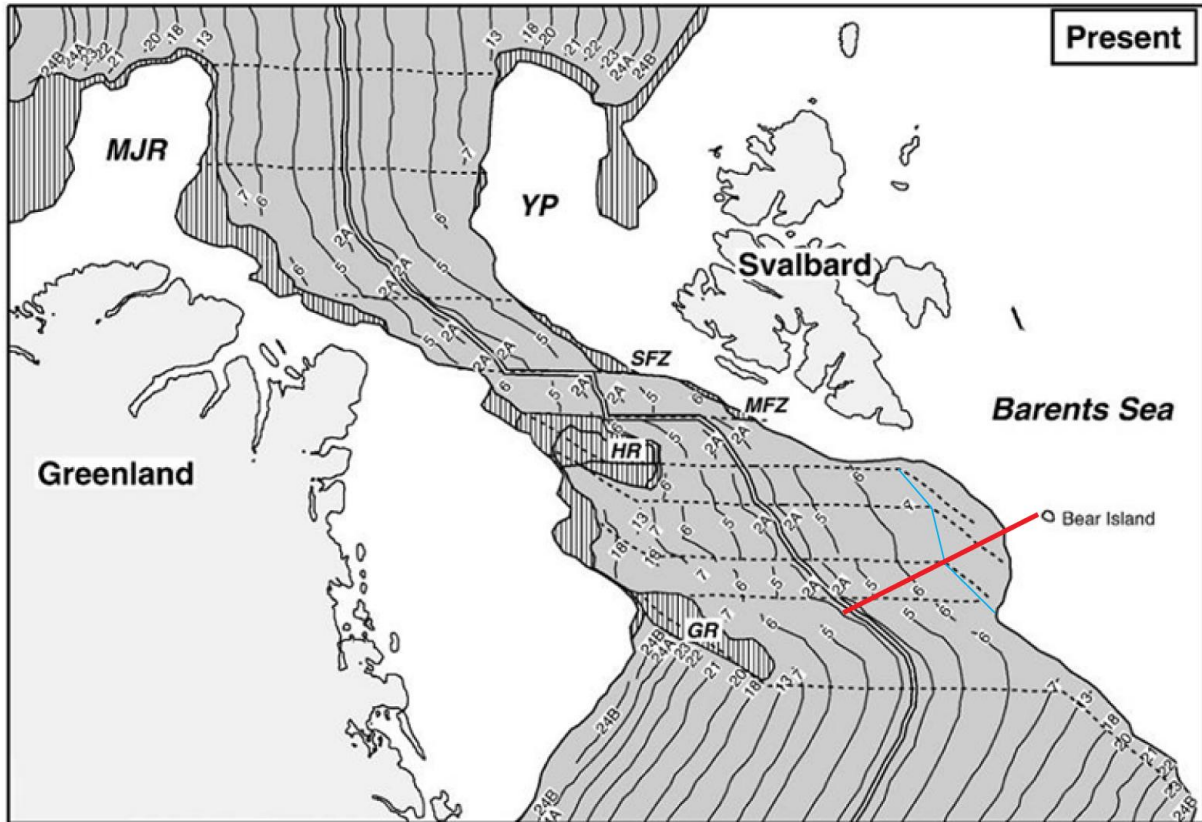
Figure 6.3: Interpreted magnetic anomalies and flowlines in the area between Svalbard and Greenland. Oceanic crust is shaded and magnetic seafloor anomalies are shown as annotated bold lines. COT and crustal provinces of unknown origin are hachured. Flowlines of relative plate motions shown by dashed lines. Approximate location of the BIN profile shown as a bold red line. Oceanic crust generated before the change in spreading direction is east of the thin blue line. GR, Greenland Ridge; HR, Hovgård Ridge; MFZ, Molloy Fracture Zone; MJR, Morris Jesup Rise; SFZ, Spitsbergen Fracture Zone; YP, Yermak Plateau. Modified from Engen et al. (2008).

The thickness decreases slightly away from the margin until 150 km, where the thickness increases to ca 7.5 km at 140 km (figure 5.4). This is probably related to increased magmatism when the spreading direction changed at anomaly 13 time (35 Ma). Rejuvenated magmatic activity at the Vestbakken Volcanic Margin is reported at this time (Faleide et al., 1988).

There is no change in the thickness of the sedimentary overburden to explain the low velocities in the oceanic crust (below 5.5 km/s) from 140 to 175 km (Figure 6.2). It is possible that the low velocities are caused by fractures related to stresses in the crust at the time of change of spreading direction.

6.3 Continent-ocean transition

The location of the continent-ocean boundary (COB) can be constrained to a narrow interval between 245 and 260 km from the velocity model (Figure 5.2). The modeled oceanic crystalline crust terminates against the continental crust from 250 to 258 km. The preferred location of the COB is therefore placed at The observed gravity also reaches a maximum value at about 255 km, and the decline in gravity east of this point is modeled as a deepening of the Moho (Figure 5.6). This location of the COT is in accordance with the position from Breivik et al. (1999), who placed the COT at about 250 km on this line, but does not fit too well with Ritzmann and Faleide (2007), who placed the COT at 235 km (Figure 6.4).

A new position of the COB is proposed at this line is proposed at 250 km (Figure 6.4). This is in accord with the results from the gravity modeling and the OBS modeling. It is likely that the shape of the gravity anomaly is caused by the same factors in the adjacent area, and the proposed COB therefore follows the maximum free air gravity anomaly 25 km north of the line. The proposed COB south of the line follows the COB from Breivik et al (1999) to the point where the position of the COB is largely in agreement between Ritzmann and Faleide (2007) and Breivik et al. (1999), ca 25 km south of the BIN line.

It is also worth noting that the profile F-F' from Faleide et al. (1993) show a basement high at the end of the layer interpreted as volcanic extrusives, corresponding to 220 km on this profile (Figure 6.1). A basement high here is also indicated in the OBS data by a protrusion observed at 225 km on OBS's 8, 9 and 10 (figure 6.5). Several attempts to model this protrusion with were made. Models with a tall and narrow basement high, models with an increase in P-wave velocity in the oceanic crust and models with a shallowing of the Moho were tested, but none of them succeeded in fully recreating the basement high and also introduced problems with tracing rays in the area. A simpler model was therefore settled upon (Figures 5.2 and 6.1). The technique of forward

modeling in this thesis is based on raytracing. Raytracing is not applicable when the medium parameters (P and S-wave velocities) changes significantly within distances of the order of the dominant wavelength (Krebes, 2004), and this can explain the difficulties encountered when modeling this feature.
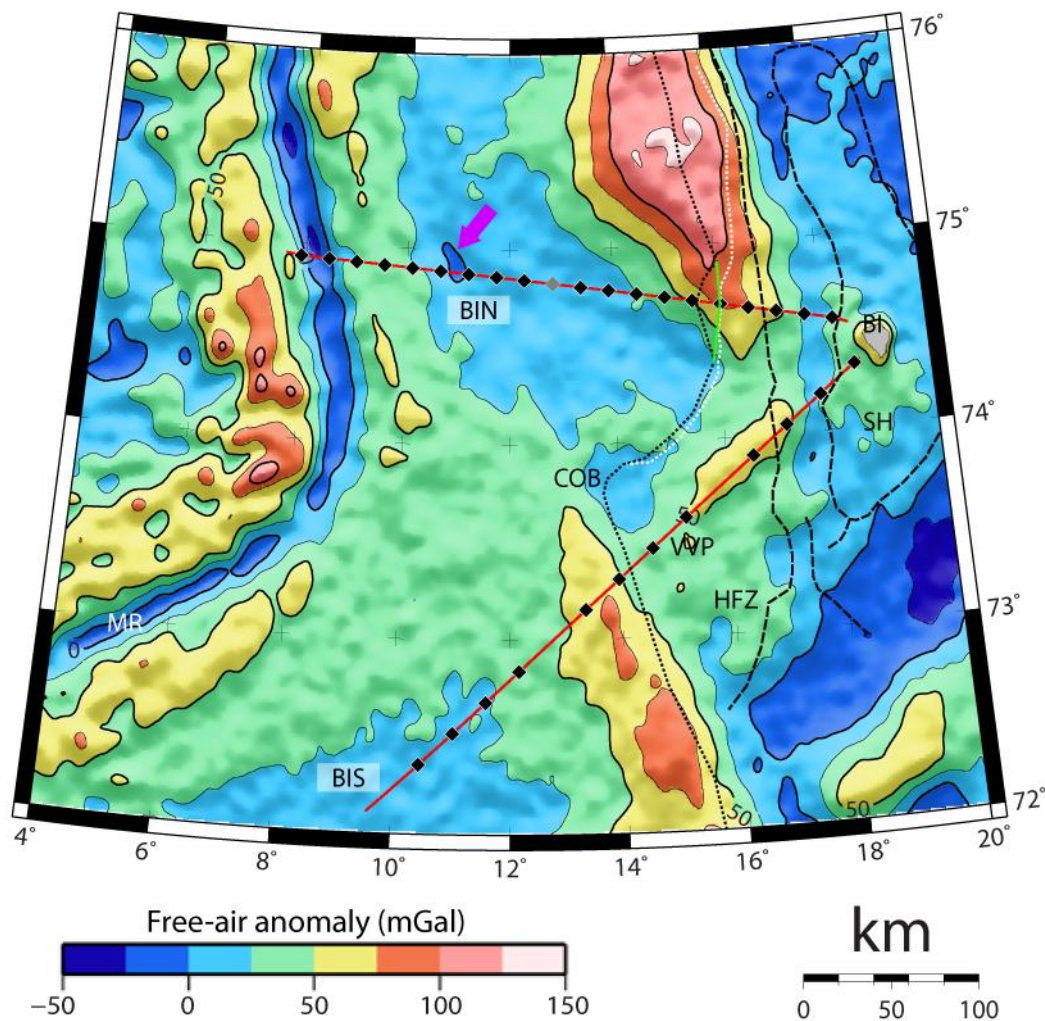
Figure 6.4: Free air anomalies in the study area. Continent-Ocean Boundaries (COB) from Ritzmann and Faleide (2007) (black dotted line), Breivik et al. (1999) (white dotted line) and proposed in this thesis (bright green line). Note the prominent gravity low marked with a purple arrow. BI, Bear Island; BIN, Bear Island North profile (this thesis), BIS, Bear Island South profile (Czuba et al., 2010); COB, Continent-Ocean boundary; KR, Knipovich Ridge; MR, Mohns Ridge; SH, Stappen High; VVP, Vestbakken Volcanic Province.
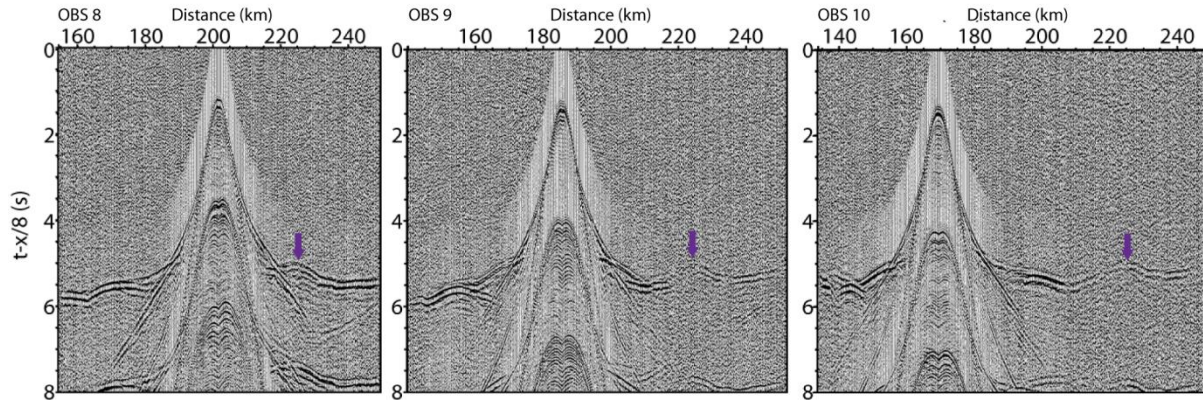
Figure 6.5: Protrusions in the traveltime curves around 225 km on seismograms from OBS's 8, 9 and 10 (Purple line).

A basement high with similar expression in the seismograms is identified on the BIS profile (Czuba et al., 2010). The high is modeled as the top of a 6 km thick and 30 km wide high velocity body with P-wave velocities of 7.2 to 7.4 km/s making up the entire crystalline crust. It has been interpreted to represent a ridge composed of serpentinized peridotites formed at a volcanic margin after slow extension and slow subsequent oceanic spreading, marking the location of the COB. Landward of this body, strongly thinned continental crust is interpreted.

It is possible that such a model could be valid on the BIN profile, especially if only the velocity model is consulted. It is difficult to distinguish between thick oceanic crust and thinned, intruded continental crust covered with lava flows based on P-wave velocities alone.

However, stretched continental crust would imply a gradual deepening Moho from the assumed peridotite ridge to normal continental crust. This contradicts the results from the gravity modeling, which requires a shallowing of the Moho over a relatively short interval from 260 to 290 km to explain the marginal gravity high. The peridotite ridge from Czuba et al. (2010) is coincident with a prominent free air gravity anomaly, and no such gravity anomaly is present at the location of the basement high on the BIN line. It is therefore suggested that the observed protrusions of the traveltime curves are caused by a smaller volcanic edifice at 220 km, possibly related to variations in the generation of magma at the Vestbakken Volcanic Province.

6.4. Continental crust

The sedimentary rocks between the Hornsund Fault Zone and the Knølegga Fault have been divided into two layers. The uppermost layer has an average velocity of 4.3 km/s. The layer has higher velocities than the pre-glacial sediments on the oceanic part of the profile, and is also located at a shallower level. A Mesozoic age is therefore suggested for this layer. The lower of these layers have an average velocity of 5.4 km/s. Rocks at the same level with similar velocities on the profile described by Breivik et al. (2003) have been interpreted to have a Paleozoic to Mesozoic age. A similar age is likely on this profile.

The P-wave velocity in top of the continental crystalline basement in the western Barents Sea is found to be around 6.2 km/s (Breivik et al., 2003). On this profile, the velocities in top of the layer interpreted as continental basement decreases from 6.3 km/s at the COB to 6.0 km/s near the Knølegga Fault at 310 km. The velocity in the top of the footwall of the Knølegga fault is modeled as 5.8 km/s. The profile shown in Brevik et al. (2003) shows ca 3 km thick layer interpreted as Devonian to Carboniferous rocks with velocities of in the range of 5.8 to 6.0 km/s overlying the basement. Such a layer is not required by the data in this study, but the continental crust is not well constrained in this model, and the model is constructed without MCS data in this area. The depth to the top crystalline basement in this area is therefore a minimum estimate.

The MCS line F-F' in Faleide et al. (1993) shows rotated fault blocks to be present between the HFZ and the KF (Figure 6.1). Rotated fault blocks are not observed in the OBS data, probably because of the limited lateral resolution in the regional OBS technique. The assumptions about age of sedimentary rocks also seem to comply with the results from the F-F'-line. However, the sediments beneath the Base Eocene (BE) reflector at 255 to 260 km are not observed in the OBS data, and this interval has been modeled as continental basement, albeit with slightly lower velocities in the top (5.8 km/s) (Figure 5.2).

A significant increase in velocities from east to west over the Knølegga fault has been modeled, which is expected as it has a large throw of at least 3-4 km and causes Jurassic and Triassic rocks to crop out on the seafloor of the upthrown side (Gabrielsen et al., 1990).

The location of the Hornsund fault zone is visible in the velocity model as a prominent lateral velocity discontinuity marking the boundary between Tertiary sediments and older sedimentary rocks. The location is in good agreement with the structural map from Ritzmann and Faleide (2007), where it was placed at ca 275 km along this line.

The Hornsund Fault Zone and the Knølegga fault have been modeled with dips of 15° and 20° respectively. The offset of the faults is difficult to estimate. It may be as high as 6 km on the Knølegga fault, but this is speculative due to the sparse illumination on the edge of the profile. The Hornsund Fault Zone does not appear to have a listric geometry. The eastern end of the of the profile is not resolved well enough to speculate if the Knølegga fault is listric or not.

6.5. Gravity modeling

Forward gravity modeling as performed in this thesis clearly has limitations. The Nafe-Drake relationship (Ludwig et al., 1970) between P-wave velocity and density have a relatively large interval in which densities for a single P-wave velocity value can be varied. For thick layers, large gravity anomalies can be accounted for, perhaps erroneously, by varying the density within the bounds of the Nafe-Drake curve (Barton, 1980). Another important factor is density variations in the upper mantle. Since the mantle blocks used in forward gravity modeling often have a large thickness, small variations in the mantle densities can satisfy large gravity anomalies. Breivik et al. (1999) demonstrated that the density of the mantle beneath oceanic crust is a function of the time since creation, since young oceanic crust are underlain by hotter and more thermally expanded lithosphere than older oceanic crust. By modeling the temperature state of the entire lithosphere and using the thermal expansion coefficient of mantle rock to find the density of the mantle, it is possible to tie the density of the mantle to an age model. This makes it possible to use gravity data to test test spreading history models, and to have greater constraints on the mantle. However, effects changing the density of the mantle not related to age, such as serpentinization, will not be detected using such an approach.

The compensation depth for this gravity model is 26 km. This is a simplification, since the actual compensation depth probably corresponds to the base of the lithosphere. In

such a shallow model, the contribution of each mantle block to the calculated gravity is not only a function of the density, but also the height of the block, which is defined by the compensation depth of the model. A model with a deeper compensation depth could give the same results with a lower density contrast between the blocks. The densities in the mantle blocks must not be taken as true values for the density in the mantle, but rather an indication of relative density in the mantle along the profile.

Realizing these weaknesses, the gravity modeling will still give qualitative controls on short-wavelength features of the profile. The largest misfits between the calculated and observed gravity are on the edges of the gravity model. The misfits are 18 mgal on the western end, and 10 mgal on the eastern end. An explanation for the poor fit here is that the model is extrapolated 300 km horizontally in each direction to avoid edge effects, and the extrapolated geology may not be representative for the real geology. The ray coverage is also poorest at the edges of the profile, which lead to a poorly constrained model in this area.

The large, negative anomaly at the ridge axis is caused by thick, low density rocks of sedimentary and volcanic origin. An especially low density mantle is also expected from the modeled velocities (7.25 km/s), but is not required to acquire a fit between the calculated and observed gravity.

The thick layer of low velocity rocks directly east of the Knipovich Escarpment at 90 km is indicated by the gravity data. The depression in the gravity field caused by this layer is visible as the largest negative anomaly between the Knipovich Ridge and the western Barents Sea margin (Figure 6.4). The gravity modeling show that the rise in gravity from 160 km to 250 km is caused primarily by decreasing water depth combined with little change in the Moho depth. This is consistent with the results from Breivik et al. (1999). The decrease in gravity from 260 to 290 km is associated with a deepening of the Moho. The relatively flat and low gravity anomaly from 290 to 310 is caused by relatively low rock densities in the downthrown block, a deep Moho and little little lateral variability in the crust in this area. The rise in gravity from 315 km is caused by the shallow, high density rocks of the Stappen High.
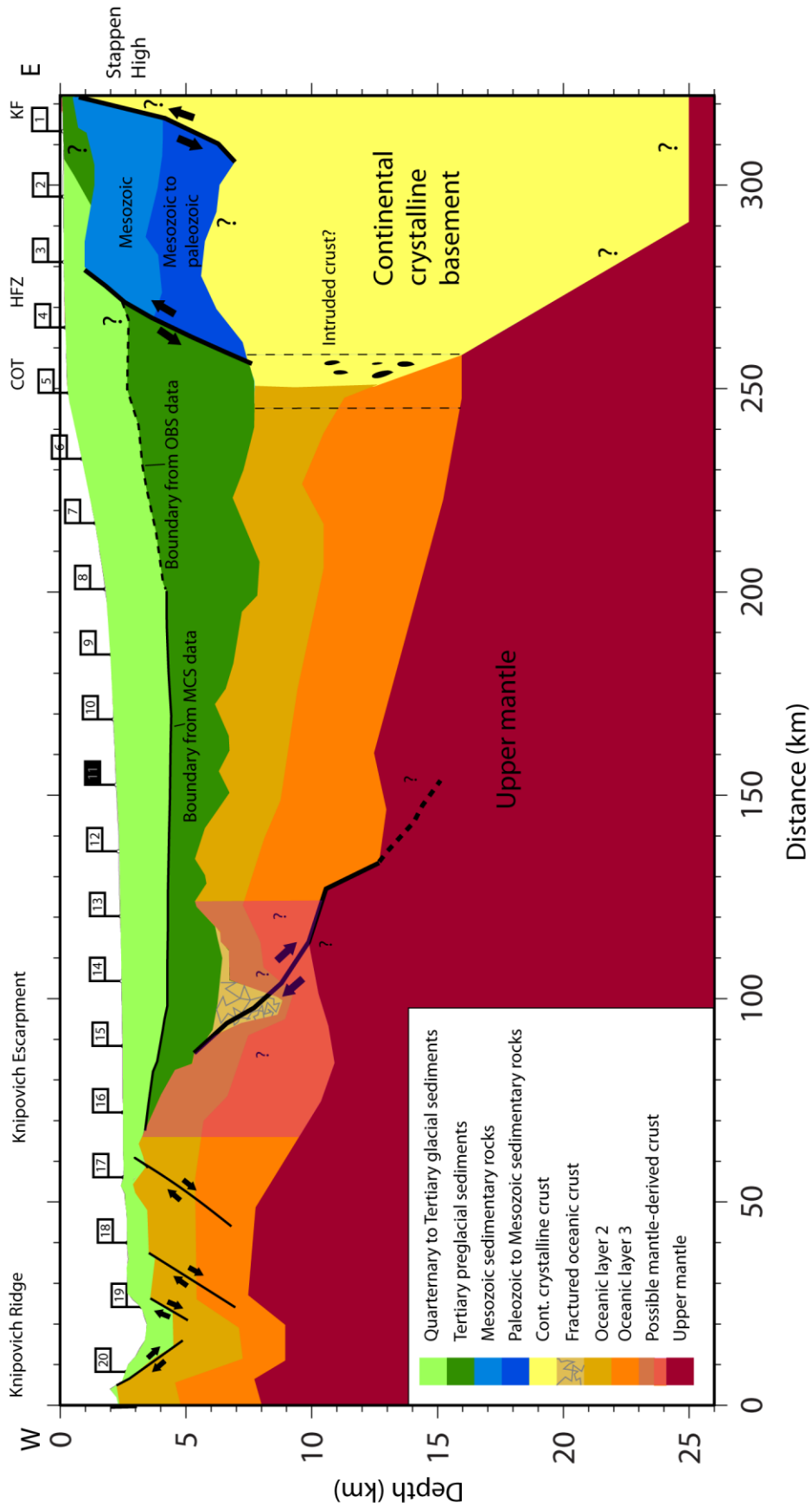
Figure 6.6: Geological model of the profile.

6.6. Geological model

A geological model summarizing the interpretations made in this thesis is presented in figure 6.6.

7. Summary and conclusions

During the fall of 2008 a survey was conducted, collecting OBS and gravity data along a line from the slow to ultraslow spreading Knipovich Ridge to Bear Island on the western Barents Sea margin. 20 OBSs were deployed, and 19 recorded useful data. The dataset is complemented by an almost coincident MCS line acquired in 2006. A P-wave model and a gravity model have been constructed from the data, and are presented in this thesis as figures 5.2 and 5.5.

A thick Cenozoic wedge of sediment lies on the oceanic crust. The thickness is 1 km over the axial graben, and increases to more than 7 km at the COB. The sediments terminate against the Hornsund Fault Zone. The velocities for the glacial package have been modeled to 1.7 to 3.1 km/s, while the velocities for the pre-glacial package have been modeled to 3.3 to 4.2 km/s. The velocities of the sediments appear to be primarily controlled by depth, not stratigraphy.

The oceanic crust show significant variations both in thickness and velocity along the line. The variations in thickness are mostly caused by thickness variations in the oceanic layer 3, and the variations in velocity happen in oceanic layer 2. 4 km thick crust, normal thickness for a slow to ultraslow spreading ridge, is found from the axial graben to 50 km along the profile. This interval is characterized by the lowest velocities found in the oceanic crust on this profile (4.4 km/s), which is attributed to high porosity and a relatively thin sedimentary overburden.

The oceanic crust is around 6 km thick and the velocities are 5.8 km/s in the top of the oceanic layer 2 from 70 to 90 km. The increase in velocities is probably caused by lower porosities due to age and increased sedimentary overburden, but it can also be caused by a change from basaltic crust to a crust composed of tectonically uplifted serpentinized peridotes. This interval is also marked by a decrease in basement depth of nearly 3 km. This escarpment is known as the Knipovich Escarpment, and it is probably caused by an eastward dipping detachment fault in the oceanic basement. However, it is difficult to determine if this fault is related to a ridge jump, generation of a core complex under seafloor spreading, or stretching of already generated oceanic crust.

From 90 to 110 km, directly east of the Knipovich Escarpment, the velocities of the top oceanic crust are 4.5 km/s, and the gradient is very low. This low-velocity zone is interpreted as a region of the oceanic crust deformed by the Knipovich Escarpment fault.

East of 125 km, the oceanic crust is thicker than 6 km, thicker than expected for a slow to ultra-slow spreading ridge. This is explained due to proximity to the Vestbakken Volcanic Province. The especially thick crust, near 8 km, is observed at 135 km and from 220 to 250 km. These intervals roughly correspond to the intervals with greatest magmatic activity in the Vestbakken Volcanic Province, the onset of seafloor spreading on the Arctic Ridges in the early Eocene, and the change in spreading direction in the early Oligocene. The velocities here are around 6 km/s, explained by lower porosities due to age and the thick sedimentary overburden.

In the continental part of the profile, four layers are modeled. The uppermost layer has an average velocity of 2.2 km/s in the west, and 3.2 km/s in the east. The layer is interpreted to represent compacted glacial sediments to the west, and uplifted and eroded preglacial sediments in the east. The two middle layers, with average P-wave velocities of 4.3 and 5.4 are interpreted to represent Mesozoic and Mesozoic to Paleozoic sedimentary rocks, respectively. The lower layer has been modeled with a velocity of around 6.2 km/s in the top and 6.6 km/s in the bottom. The top of this layer is a minimum estimate of the top of the continental basement.

The Hornsund Fault Zone and the Knølegga Fault are modeled, and their positions along the line match the positions of earlier work.

The depth to the Moho is 7.5 km around the ridge axis, and decreases to 11 km beneath the Knipovich Escarpment. East of this escarpment, a prominent shallowing to of the Moho to 10 km is modeled. A sudden increase to 13 km is observed at 125 km along the profile. From this point, the Moho depth increases steadily to 16 km at the COB. A deepening of the Moho to 26 km has been modeled in the interval from 260 to 290, and the depth is held constant from here to the end of the line.

A new position of the COB is proposed at 250 km along this profile.

References

Barton, P.J., 1986. The relationship between seismic velocity and density in the continental crust – a useful constraint?. Geophys. J. R. astr. Soc. 87, 195-208

Breivik, A.J., and Mjelde, R., 2001 (unpublished report). Institute of Solid Earth Physics, University of Bergen. 128 pp.

Breivik, A.J., Mjelde, R., Grogan, P., Shimamura, H., Murai, Y., and Nishimura, Y., 2003. Crustal structure and transforms margin development south of Svalbard Based on ocean bottom seismometer data. Tectonophysics, 369: 37-70.

Breivik, A.J., Verhoef, J. and Faleide, J.I., 1999. Effect of thermal contrasts on gravity modeling at passive margins: Results from the western Barents Sea. Journal of Geophysical Research, 104: 15293-15312.

Bruvoll, V., Breivik, A.J., Mjelde, R. and Pedersen, R., 2009. Burial of the Mohn-Knipovich seafloor spreading ridge by the Bear Island Fan: Time constraints on tectonic evolution from seismic stratigraphy. Tectonics, 28: DOI 10.1029/2008TC002396

Butt, F.A., Elverhøi, A., Solheim, A. and Forsberg C.F., 2000. Deciphering Late Cenozoic development of the western Svalbard Margin from ODP site 986 results. Geology, 169: 373-390.

Cannat, M., 1993. Emplacement of mantle rocks in the seafloor at mid-ocean ridges. Journal of Geophysical Research 98, 4163–4172.

Carlson, R.L., and Raskin, G.S., 1984. Density of the ocean crust. Nature, 311: 555 – 588

Crane, K., Sundvor, E., Buck, R. and Martinez, F., 1991. Rifting in the northern Norwegian-Greenland Sea: Thermal tests of asymmetric spreading. Journal of Geophysical Research, 96(B9): 14529-14550.

Czuba, W., Grad, M., Mjelde, R., Guterch, A., Libak, A., Krüger, F., Murai, Y., and Schweitzer, J., 2010. Continent-ocean-transition across a rifted shear-margin: off Bear Island, Barents Sea. Geophysical Journal International. (submitted)

Dick, H.J.B., Lin, J. and Schouten, H., 2003. An ultraslow-spreading class of ocean ridge. Nature, 426(6965): 405-412.

Dunkin, J. W., and Levin, F. K., 1973. Effect of normal moveout on a seismic pulse. Geophysics, 38: 635–642.

Ebbing, J., Braitenberg, C., and Wienecke. S., 2007. Insights into the lithospheric structure and tectonic setting of the Barents Sea region from isostatic considerations. Geophysical Journal International, 171: 1390-1430

Engen, Ø., Faleide, J.I., Dyreng, T.K., 2008. Opening of the Fram Strait gateway: A review of plate tectonic constraints. Tectonophysics 450 (2008) 51–69.

Eldholm, O., Faleide, J.I., and Myhre, A. M., 1987. Continent-ocean transition at the western Barents Sea / Svalbard continental margin. Geology 15, p: 1118-1122.

Eldholm, O., Skogseid, J., Sundvor, E. and Myhre, A.M., 1990. The Norwegian-Greenland Sea. In: A. Grantz, L. Johnson and J.F. Sweeney (Editors), The Geology of North America. Vol. L, The Arctic Ocean Region. The Geological Society of America, Boulder, CO, pp. 351–364.

Faleide, J.I., Gudlaugsson, S.T., Eldholm, O., Myhre, A.M., and Jackson, H.R., 1991. Deep seismic transects across the western Barents Sea continental margin. Tectonophysics, 189: 73–89.

Faleide, J.I., Myhre, A.M., and Eldholm, O., 1988. Early tertiary volcanism at the western Barents Sea margin, in Early Tertiary Volcanism and the Opening of the NE Atlantic, edited by A.C. Morton and L.M. Parson, Geol. Soc. Spec. Publ., 39:135-146

Faleide, J.I., Solheim, A., Fiedler, A., Hjelstuen, B.O., Andersen, E.S. and Vanneste, K., 1996. Late Cenozoic evolution of the western Barents Sea-Svalbard continental margin. Global and Planetary Change, 12: 53-74.

Faleide, J.I., Tsikalas, F., Breivik, A.J., Mjelde, R., Ritzmann, O., Engen, Ø., and Eldholm, O., 2008. Structure and evolution of the continental margin off Norway and the Barents Sea. Episodes, 31 (1): 82-91

Faleide, J.I., Vågnes, E., Gudlaugsson, S.T., 1993. Late Mesozoic–Cenozoic evolution of the southwestern Barents Sea. In: Parker, J.R. (Ed.), Petroleum Geology of Northwest Europe: Proceedings of the 4th Conference. Geological Society, London, pp. 933-950.

Fowler, C.M.R., 1990. The solid earth. Cambridge University Press, New York, 472 pp.

Gabrielsen, R.H., Færseth, R.B., Jensen, L., Riis, F., 1990. Structural elements of the Norwegian continental shelf: Part 1. The Barents Sea Region. NPD Bull., vol. 6. Nor. Petrol. Dir., Stavanger, Norway.

Glicken, M., 1962. Eötvös corrections for a moving gravity meter. Geophysics 27: 531-533

Harrison, C.G.A. and Bonatti, E., 1981. The oceanic lithosphere. In: C. Emiliano (Editor), The Sea. Vol. 7. Wiley, New York, pp. 21-48.

Hess, H.H., 1962. History of ocean basins. Petrologic Studies: 599-620.

Hjelstuen, B.O., Elverhøi, A. and Faleide, J.I., 1996. Cenozoic erosion and sediment yield in the drainage area of the Storfjorden Fan. Global and Planetary Change, 12: 95-117.

Jacobson, R. S., 1992. Impact of crustal evolution on changes of the seismic properties of the uppermost oceanic crust. Reviews of Geophysics, 30: 23–42

Johnsen, H., 2006. Cruise Report: Bjørnøya, by use of Håkon Mosby, University of Bergen

Kandilarov, A., and Mjelde, R., 2008. Cruise Report: PETROBAR 2008: OBS survey, Barents Sea by use of Håkon Mosby, University of Bergen

Kandilarov, A., Mjelde, R., Okino, K. and Murai, Y., 2008. Crustal structure of the ultra slow spreading Knipovich Ridge, North Atlantic, derived from OBS, MCS and gravity data, along a presumed amagmatic portion of oceanic crustal formation. Marine Geophysical Researches, 29(2): DOI 10.1007/s11001-008-9050-0

Kearey, P., Brooks, M. and Hill, I., 2002. An Introduction to Geophysical Exploration, Third edition. Blackwell Publishing, 262 pp.

Kearey, P. and Vine, F.J., 1996. Global Tectonics, 2nd edition. Blackwell Publishing, New York, 333 pp.

Krebes, E.S, 2004. Seismic Forward Modeling. CSEG Recorder, 29(4): 28-39

Kristoffersen, Y., and Talwanim M., 1977. Extinct tripple junction south of Greenland and the Tertiary motion of Greenland relative to North America. Geological Society of America Bulletin, 88: 1037-1049.

Ljones, F., Kuwano, A., Mjelde, R., Breivik, A., Shimamura, H., Murai, Y. and Nishimura, Y., 2004. Crustal transect from the North Atlantic Knipovich Ridge to the Svalbard Margin west of Hornsund. Tectonophysics, 378: 17-41.

Ludwig, W.J., Nafe, J.E. and Drake, C.L., 1970. Seismic refraction. In: A.E. Maxwell (Editor), The Sea. Vol. 4, Part 1. Wiley, New York, pp. 53-84.

Lundin, E. and Doré, A.G., 2002. Mid-Cenozoic post-breakup deformation in the 'passive'margins bordering the Norwegian–Greenland Sea. Marine and Petroleum Geology, 19(1): 79-93.

Macdonald, K.C., 1982. Mid-Ocean Ridges: Fine Scale Tectonic, Volcanic and Hydrothermal Processes Within the Plate Boundary Zone. Annual Reviews in Earth and Planetary Sciences, 10(1): 155-190.

Macdonald, K., Scheirer, D.S. and Carbotte, S.M., 1991. Mid-Ocean Ridges: Discontinuities, Segments and Giant Cracks. Science, 253(5023): 986-994.

Minakov, A., 2008. Ocean Bottom Seismometer survey in the western Barents Sea (PETROBAR/IPY 2008 projects), University of Bergen.

Mjelde, R., Breivik, A.J., Raum, T., Mittelstaedt, E., Ito, G. and Faleide, J.I., 2008. Magmatic and tectonic evolution of the North Atlantic. Journal of the Geological Society, 165(1): 31.

Okino, K., Curewitz, D., Asada, M., Tamaki, K., Vogt, P. and Crane, K., 2002. Preliminary analysis of the Knipovich Ridge segmentation: influence of focused magmatism and ridge obliquity on an ultraslow spreading system. Earth and Planetary Science Letters, 202(2): 275-288.

Ottesen D., Dowdeswell J.A., and Rise L., 2005. Submarine landforms and the reconstruction of fast-flowing ice streams within a large Quaternary ice sheet: the 2500-

km-long Norwegian–Svalbard margin (57°– 80° N). Geological Society of America Bulletin 117(7/8): 1033–1050.

Pedley, R.C., 1993. GRAVMAG User Manual-interactive 2.5 d gravity and magnetic modeling, British Geological survey, Technical Report WK/93/26/R.

Perry, R.K., Fleming, H.S., Cherkis, N.Z., Feden, R.H. and Vogt, P.R., 1980. Bathymetry of the Norwegian-Greenland and Western Barents Seas: Geological Society of America, Chart-No, MC-21, Washington, DC, Naval Research Laboratory.

Reid, I. and Jackson, H.R., 1981. Oceanic spreading rate and crustal thickness. Marine Geophysical Researches, 5(2): 165-172.

Ritzmann, O., and Faleide, J., I., 2007, Caledonian basement of the western Barents Sea. Tectonics, 26: TC5014, doi:10.1029/2006tc002059

Ritzmann, O., Jokat, W., Mjelde, R. and Shimamura, H., 2002. Crustal structure between the Knipovich Ridge and the Van Mijenfjorden (Svalbard). Marine Geophysical Researches, 23(5): 379-401.

Ritzmann, O., Maercklin, N., Faleide, J.I., Bungim, Mooney, W.D. and Detweiler, S.T., 2007. A three-dimensional geophysical model of the crust in the Barents Sea region: model construction and basement characterization. Geophysical Journal International, 170: 417–435.

Roest, W.R. and Srivastava S.P. 1989. Seafloor spreading in the Labrador Sea: a new reconstruction, Geology, 17 : 1000-1004.

Sclater, J.G, Anderson, R.N., and Bell, M.L., 1971. Elevation of Ridges and Evolution of the Central Eastern Pacific. J. Geophys. Res., 70(32): 7888-7915

Spudich, P. and Orcutt, J., 1980. A new look at the seismic velocity structure of the oceanic crust. Rev. Geophys. Space Phys., 18: 627-645.

Sundvor, E., and E. Eldholm, The western and northern margin off Svalbard, Tectonophysics, 59, 239–250, 1979.

Steel, R., Gjelberg, J., Nøttvedt, A., Helland-Hansen, W., Kleinspehn, K., and Rye-Larsen, M., 1985. The tertiary strike-slip basins and orogenic belt of Spitsbergen. Society of Economic Paleontologists and Mineralogists Special Publication, 37: 339-360.

Talwani, M. and Eldholm, O., 1977. Evolution of the Norwegian-Greenland Sea. Bulletin of the Geological Society of America, 88(7): 969-999.

Torsvik, T.H., Mosar, J. and Eide, E.A., 2001. Cretaceous-Tertiary geodynamics: a North Atlantic exercise. Geophysical Journal International, 146(3): 850-866.

Tucholke, B. E., and Lin, J. (1994). A geological model for the structure of ridge segments in slow spreading ocean crust. Journal of Geophysical Research, 99(B6), 11937-11958.

Vogt, P., L.C. Kovacs, L.C. Berneo, and S.P. Srivastava, 1982. Asymmetric geophysical signatures in the Greenland-Norwegian and southern Labrador seas and the Eurasia Basin. Tectonophysics, 89: 95–160

Wilkens, R. H., G. J. Fryer, and J. Karsten, Evolution of porosity and seismic structure of upper oceanic crust: Importance of aspect ratios, J. Geophys. Res., 96, 17,981–17,995, 1991.

White, R.S., McKenzie, D. and Onions, R.K., 1992. Oceanic crustal thickness from seismic measurements and rare earth element inversions. Journal of Geophysical Research, 97(B13): 19683 - 19715.

Zelt, C.A., 1999. Modelling strategies and model assessment for wide-angle seismic traveltime data. Geophys. J. Int., 139(1): 183-204.

Zelt, C.A. and Ellis, R.M., 1988. Practical and efficient ray tracing in two-dimensional media for rapid traveltime and amplitude forward modeling. Can. J. Explor. Geophys, 24(1): 16-31.

Zelt, C.A. and Forsyth, D.A., 1994. Modeling wide-angle seismic data for crustal structure: Southeastern Grenville Province. Journal of Geophysical Research, 99(11): 687–11

Zelt, C.A. and Smith, R.B., 1992. Seismic traveltime inversion for 2-D crustal velocity structure. Geophysical Journal International, 108(1): 16-34.

Appendix

Seismograms, calculated rays and traced rays

The following pages contain plots of the rays traced through the model for each OBS, and plots where calculated rays are overlain the picks. The seismogram for each OBS is also shown underneath the plots, allowing for easy comparison between the picks and the actual data. The seismograms shown are hydrophone components. The vertical components is not presented, because the only difference between these two components is that the vertical seismometer data had generally lower quality than the hydrophone data.

The seismograms are subjected to the following processing steps:

1. Traveltime reduction, with 8 km/s reduction velocity
2. Bandpass filtering with parameters 2, 5, 15, 20 Hz
3. Automatic gain control with 2 second window length
4. Debiasing
5. Spiking deconvolution with parameters mincorr=0, maxcorr=11

OBS 1
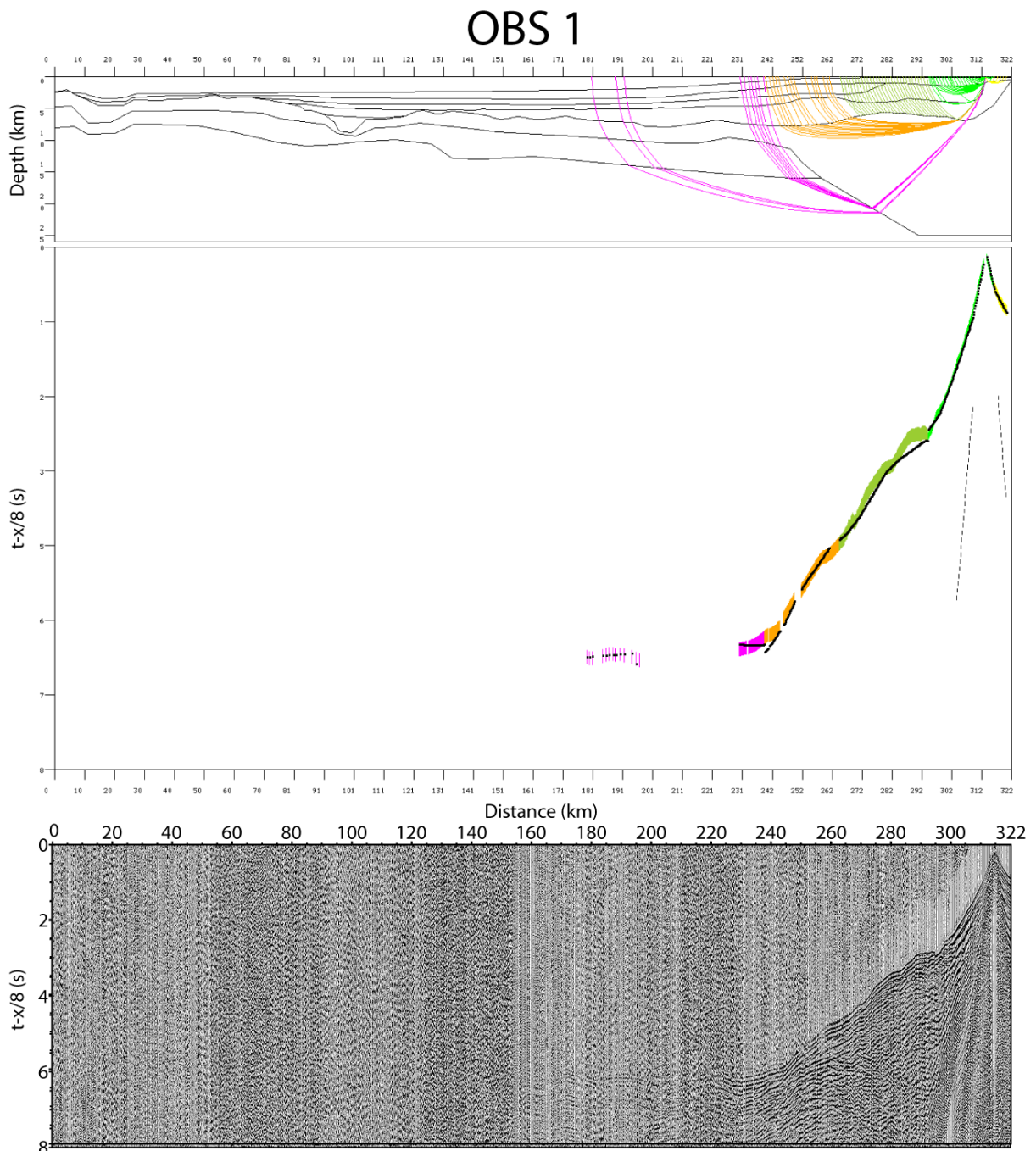
Figure A.1: Rays traced through the model (upper plot) and calculated rays (black lines) and picks (colored) from Rayinvr (middle plot), and OBS seismogram (lower plot).
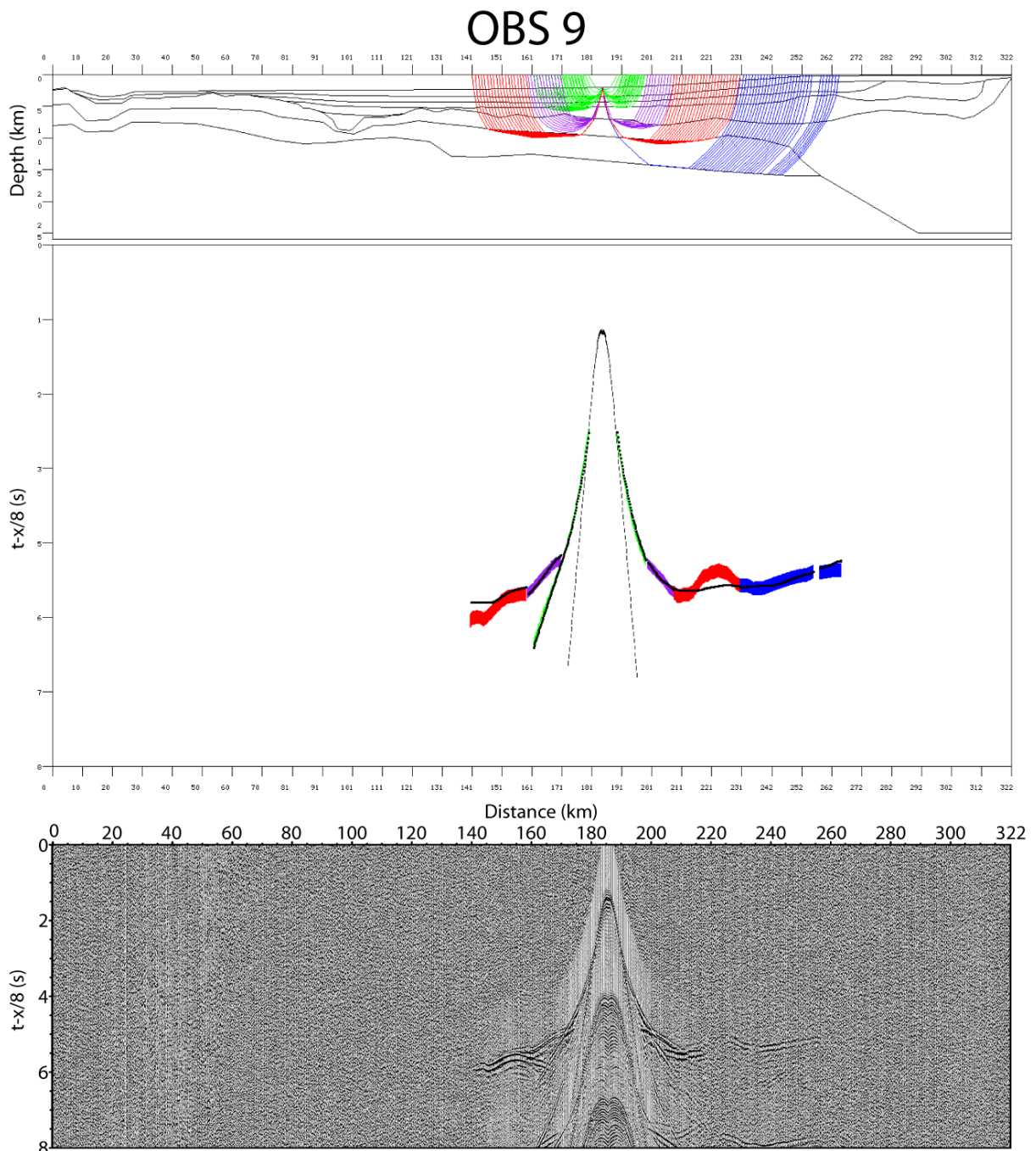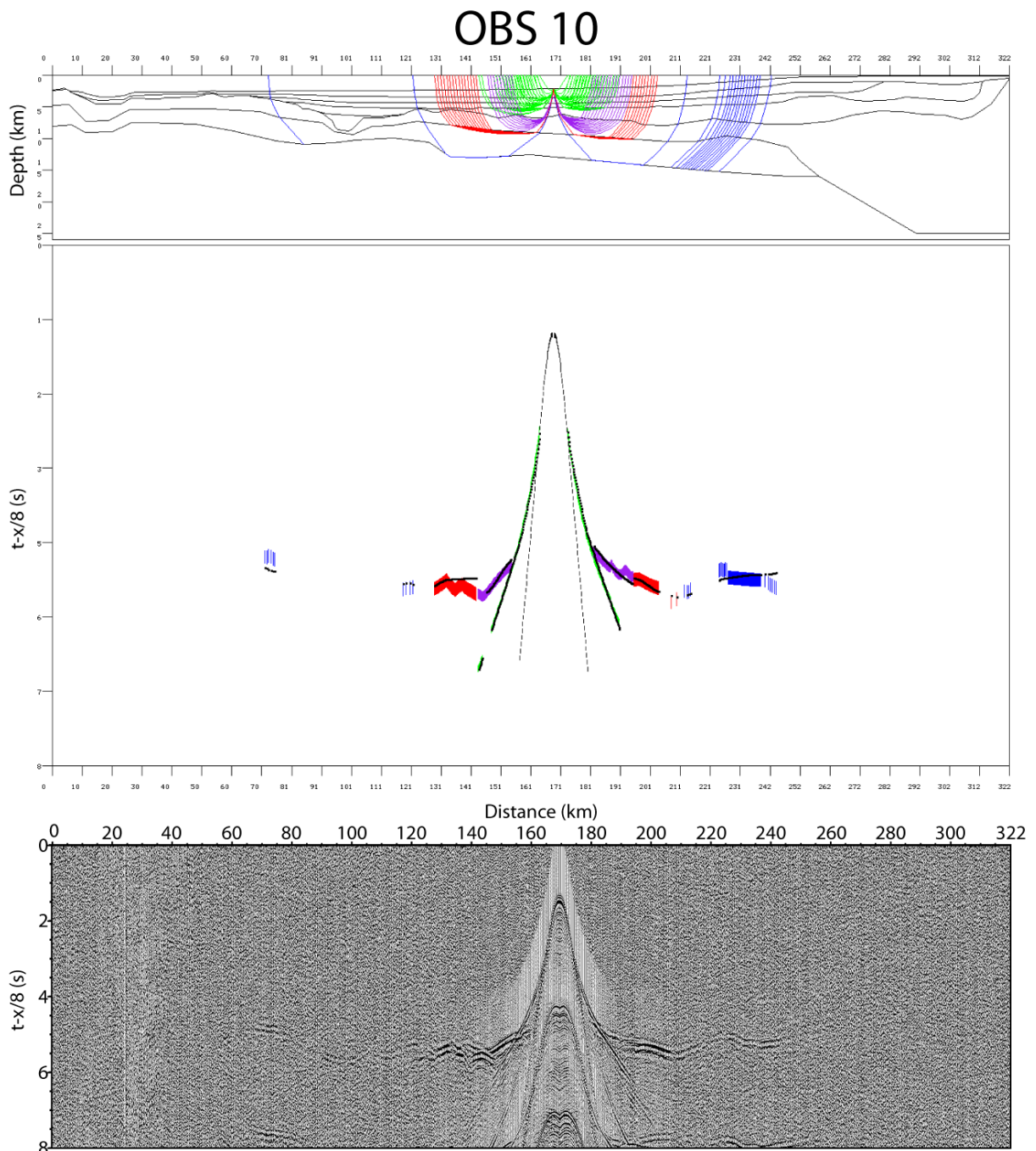
OBS 2
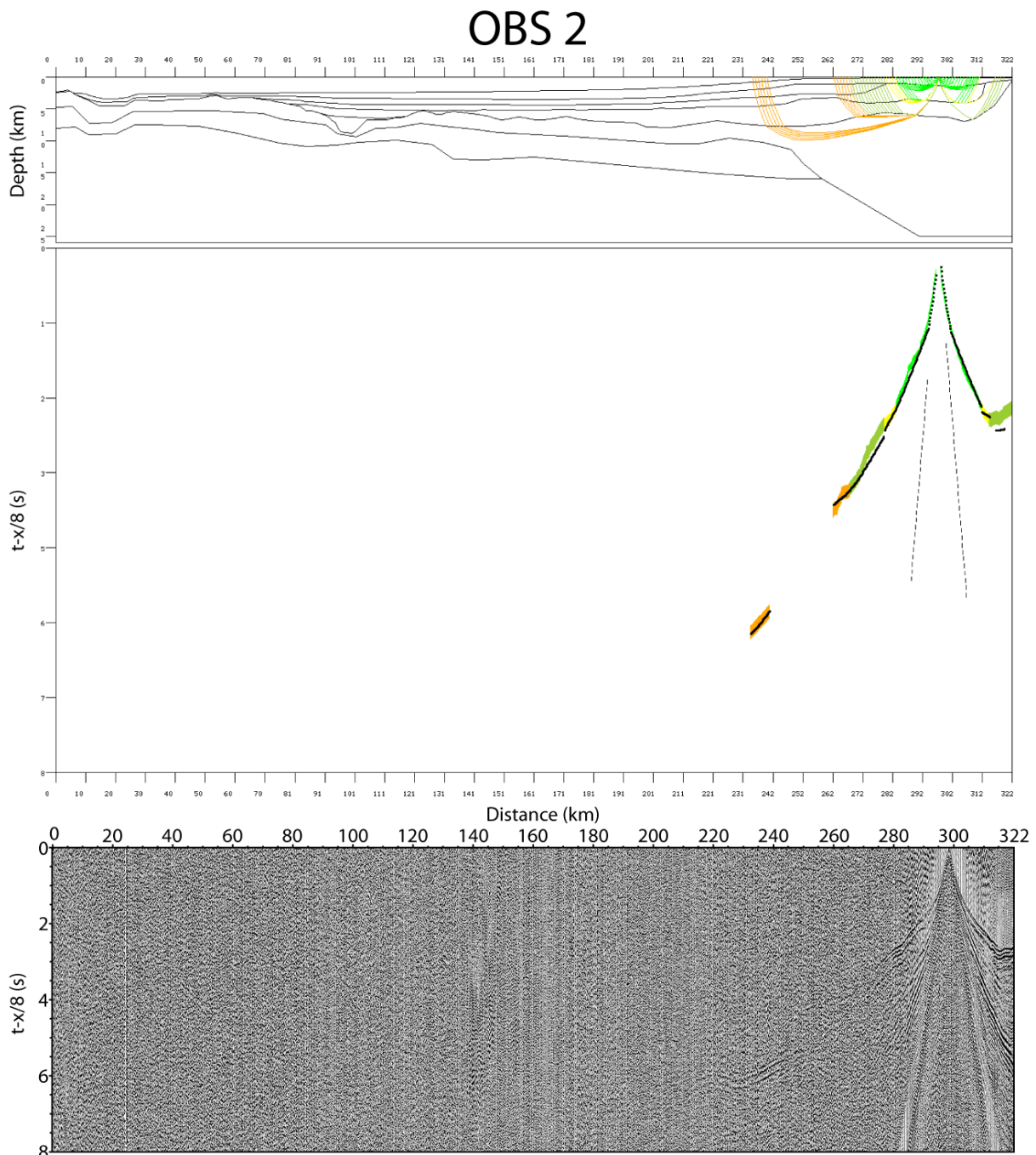
Figure A.2: Rays traced through the model (upper plot) and calculated rays (black lines) and picks (colored) from Rayinvr (middle plot), and OBS seismogram (lower plot).
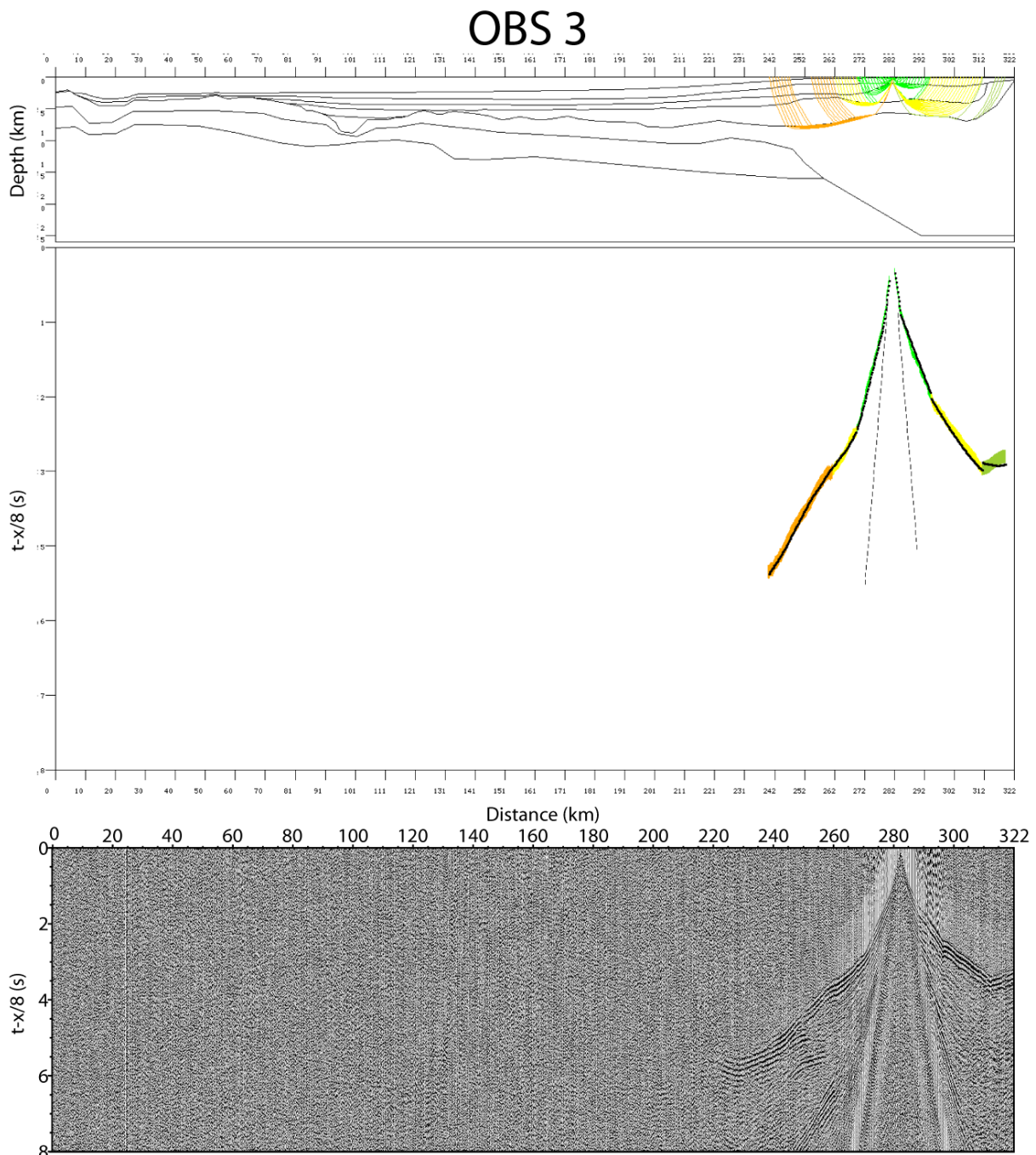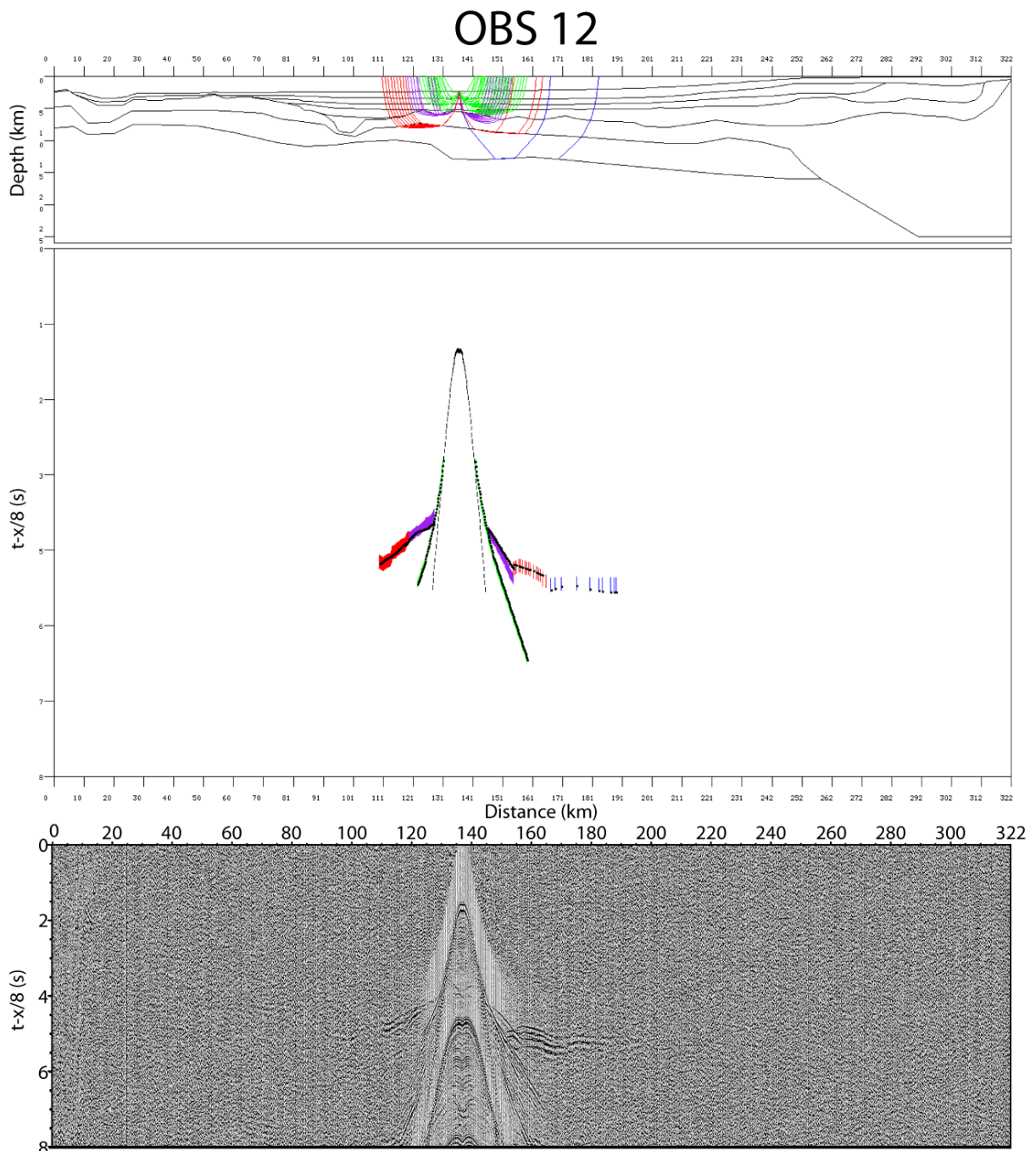
Figure A.3: Rays traced through the model (upper plot) and calculated rays (black lines) and picks (colored) from Rayinvr (middle plot), and OBS seismogram (lower plot).
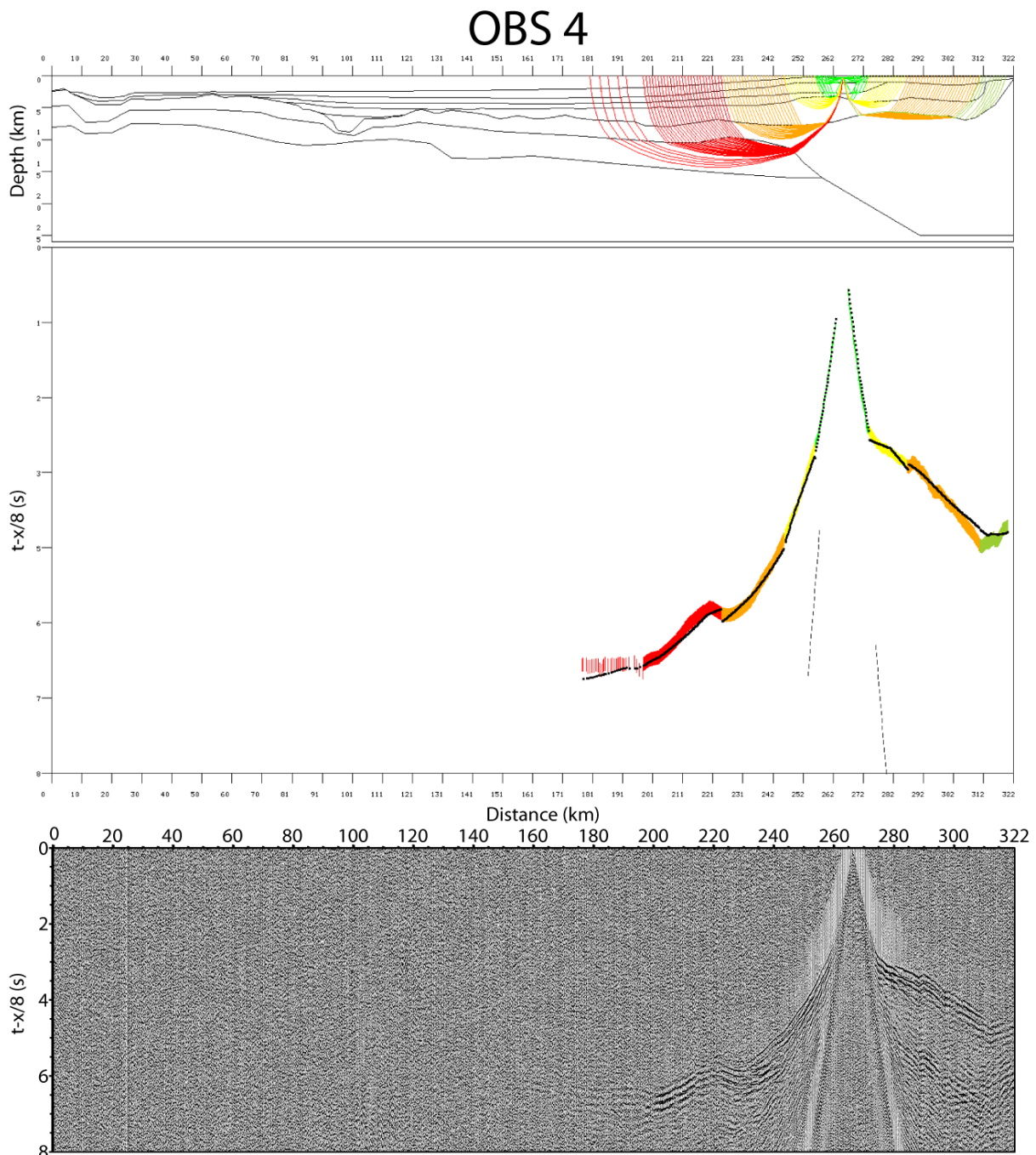
Figure A.4: Rays traced through the model (upper plot) and calculated rays (black lines) and picks (colored) from Rayinvr (middle plot), and OBS seismogram (lower plot).

OBS 5
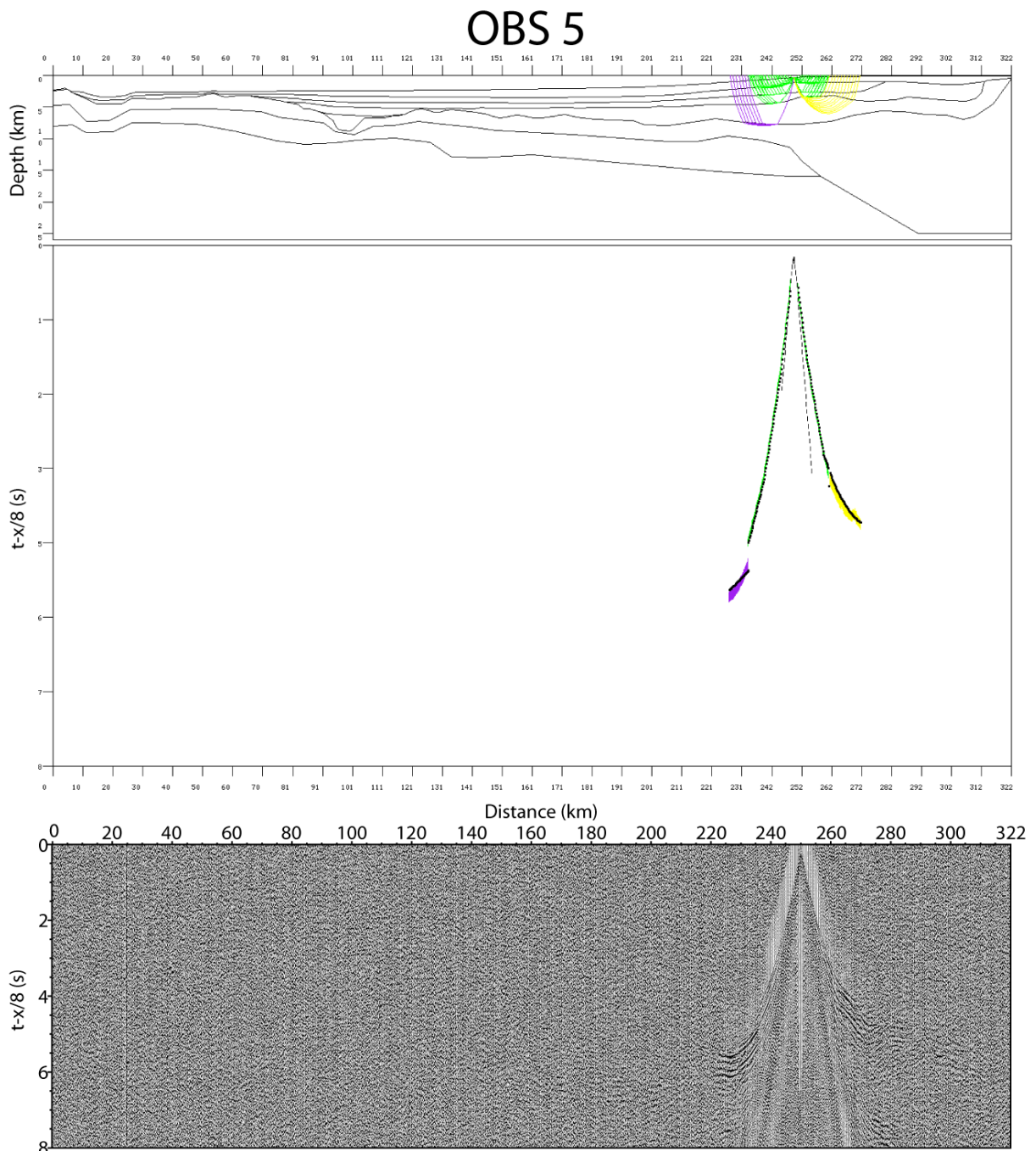
Figure A.5: Rays traced through the model (upper plot) and calculated rays (black lines) and picks (colored) from Rayinvr (middle plot), and OBS seismogram (lower plot).
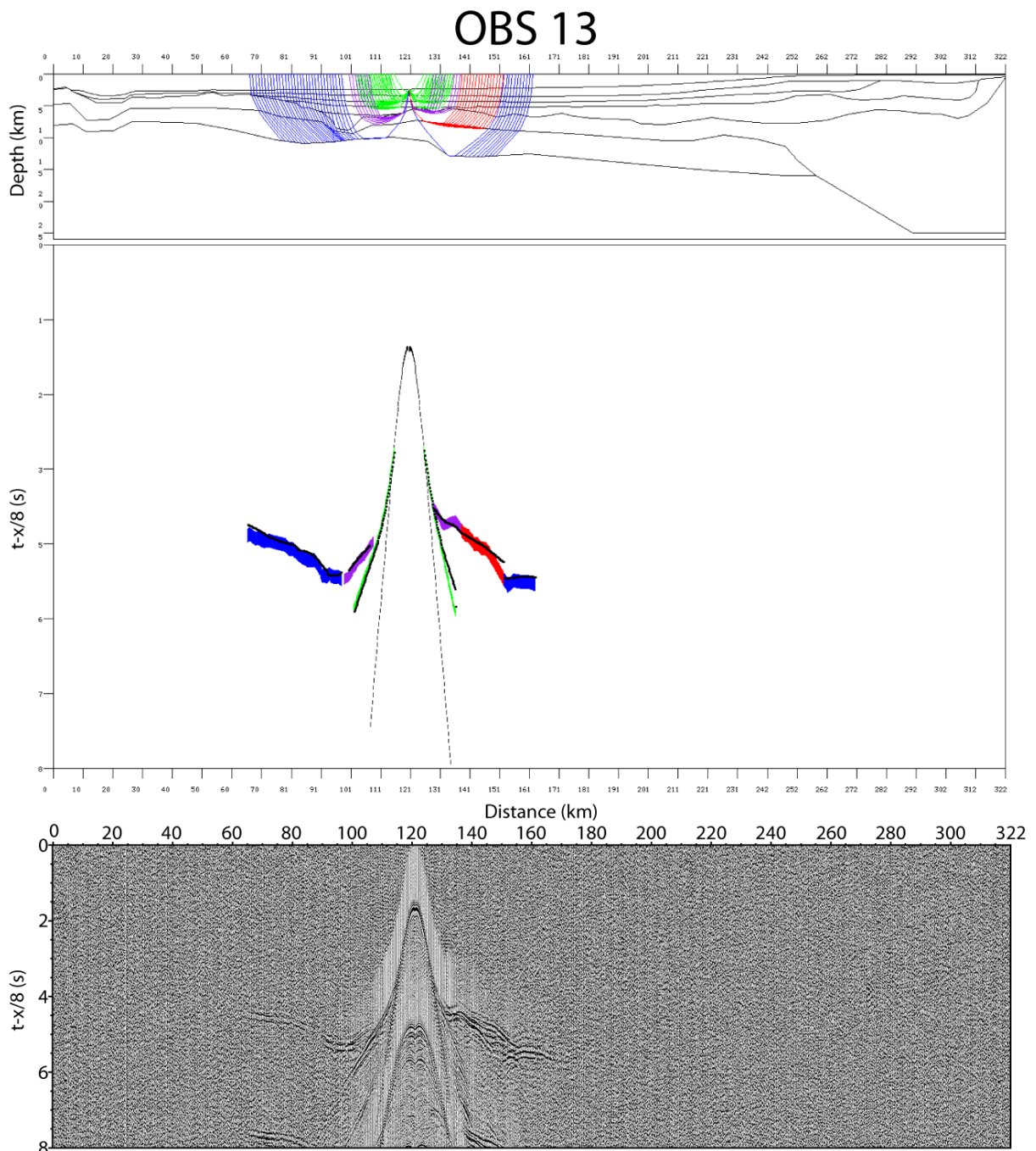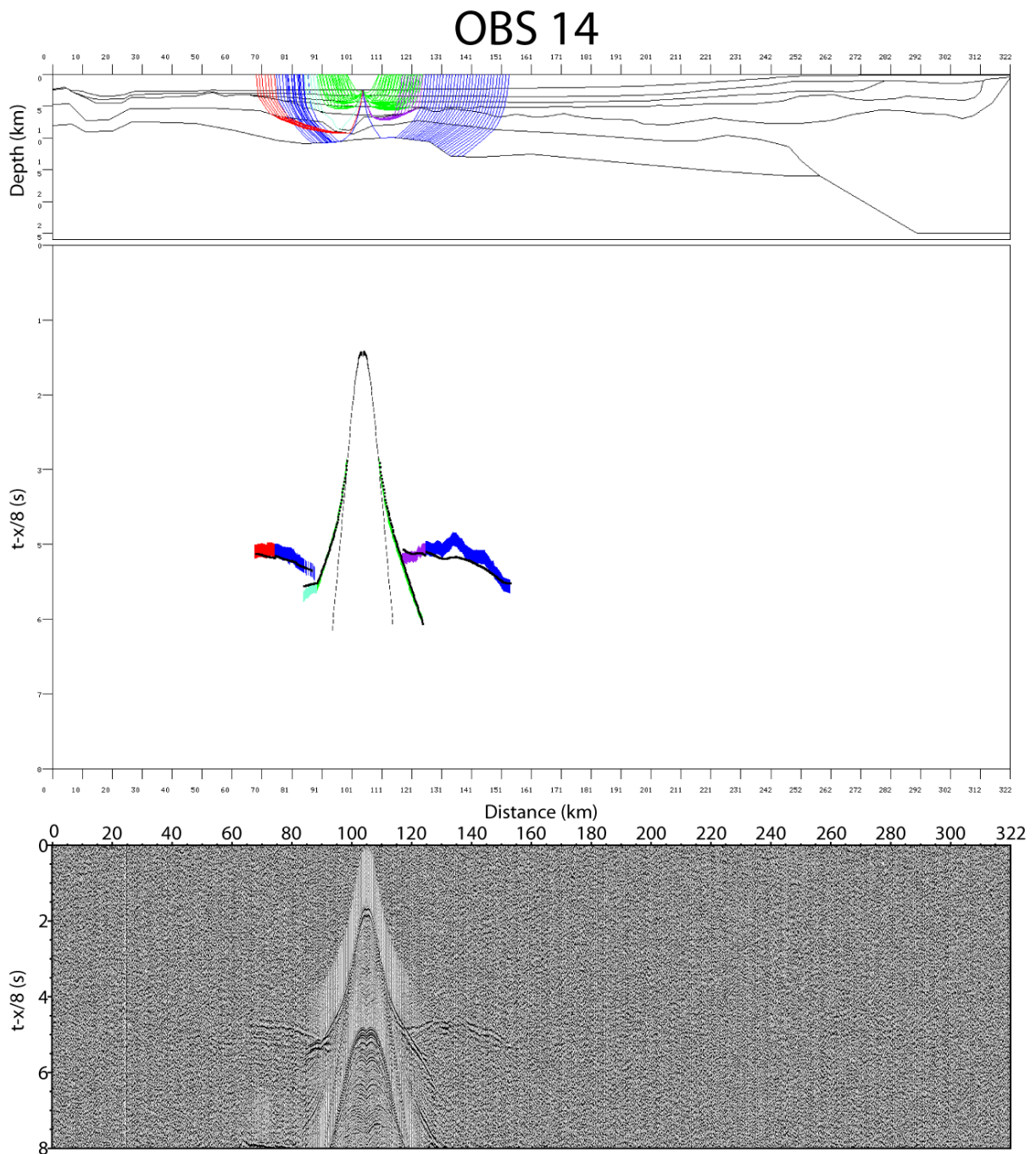
OBS 6
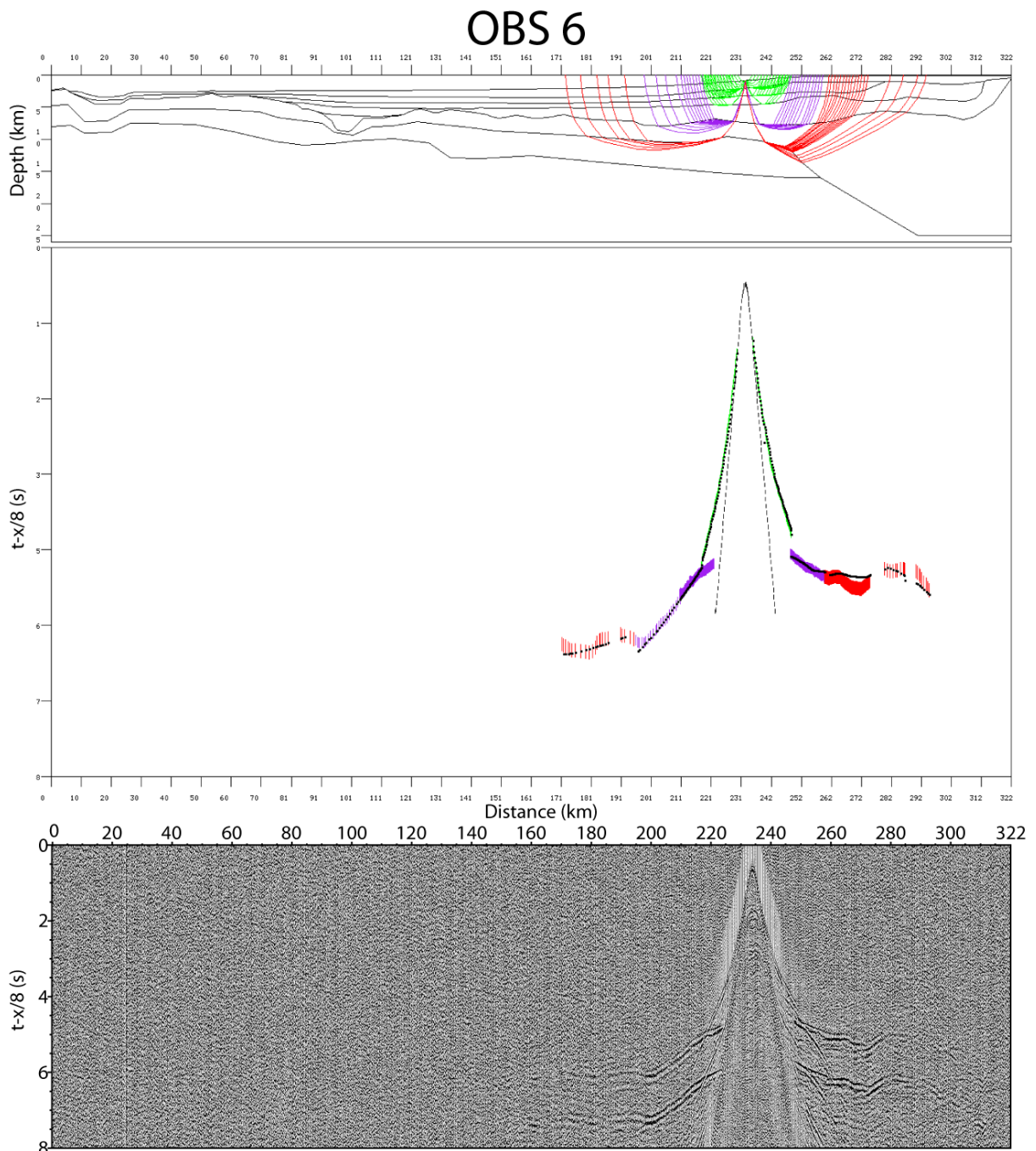
Figure A.6: Rays traced through the model (upper plot) and calculated rays (black lines) and picks (colored) from Rayinvr (middle plot), and OBS seismogram (lower plot).

OBS 7
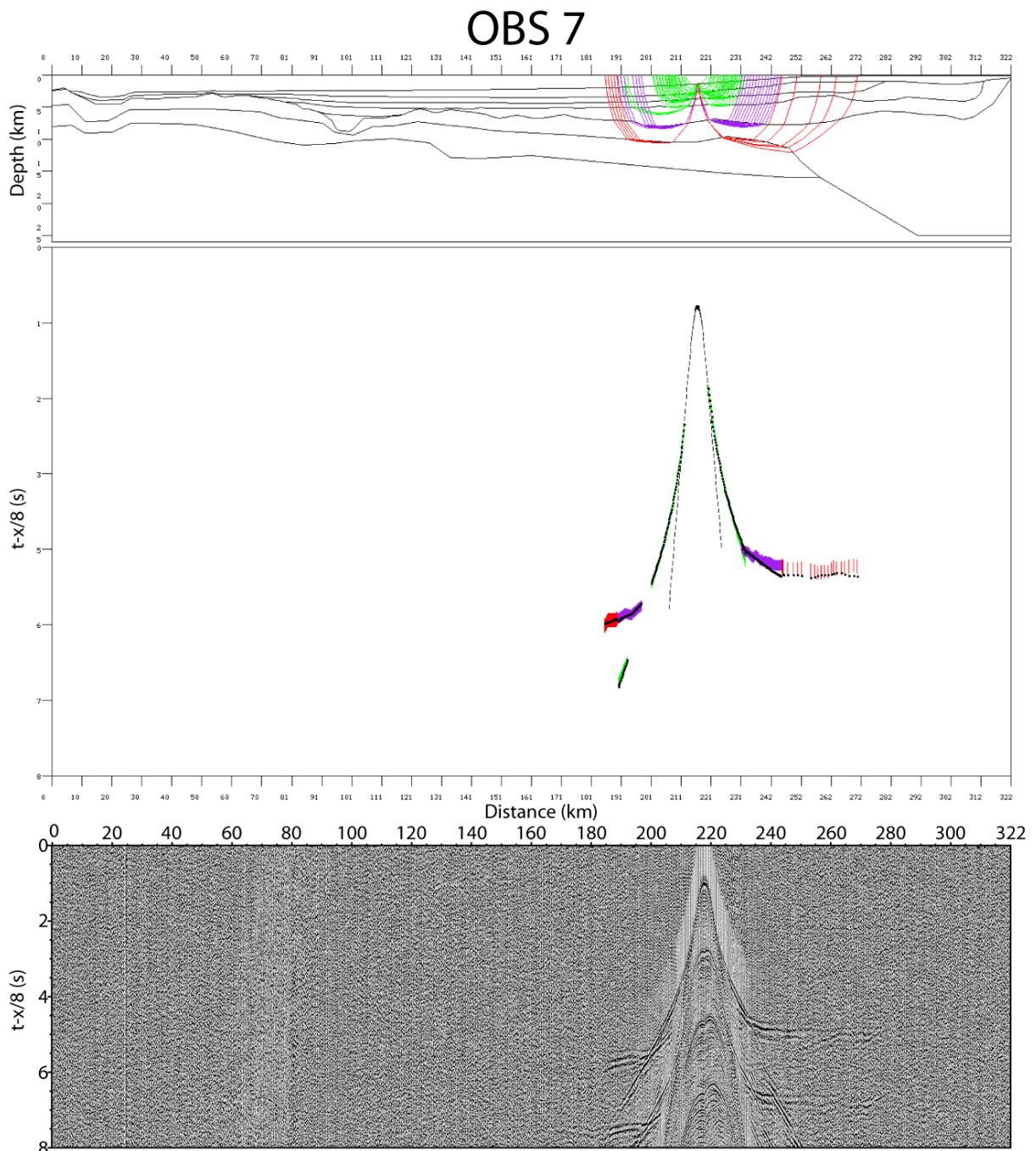
Figure A.7: Rays traced through the model (upper plot) and calculated rays (black lines) and picks (colored) from Rayinvr (middle plot), and OBS seismogram (lower plot).
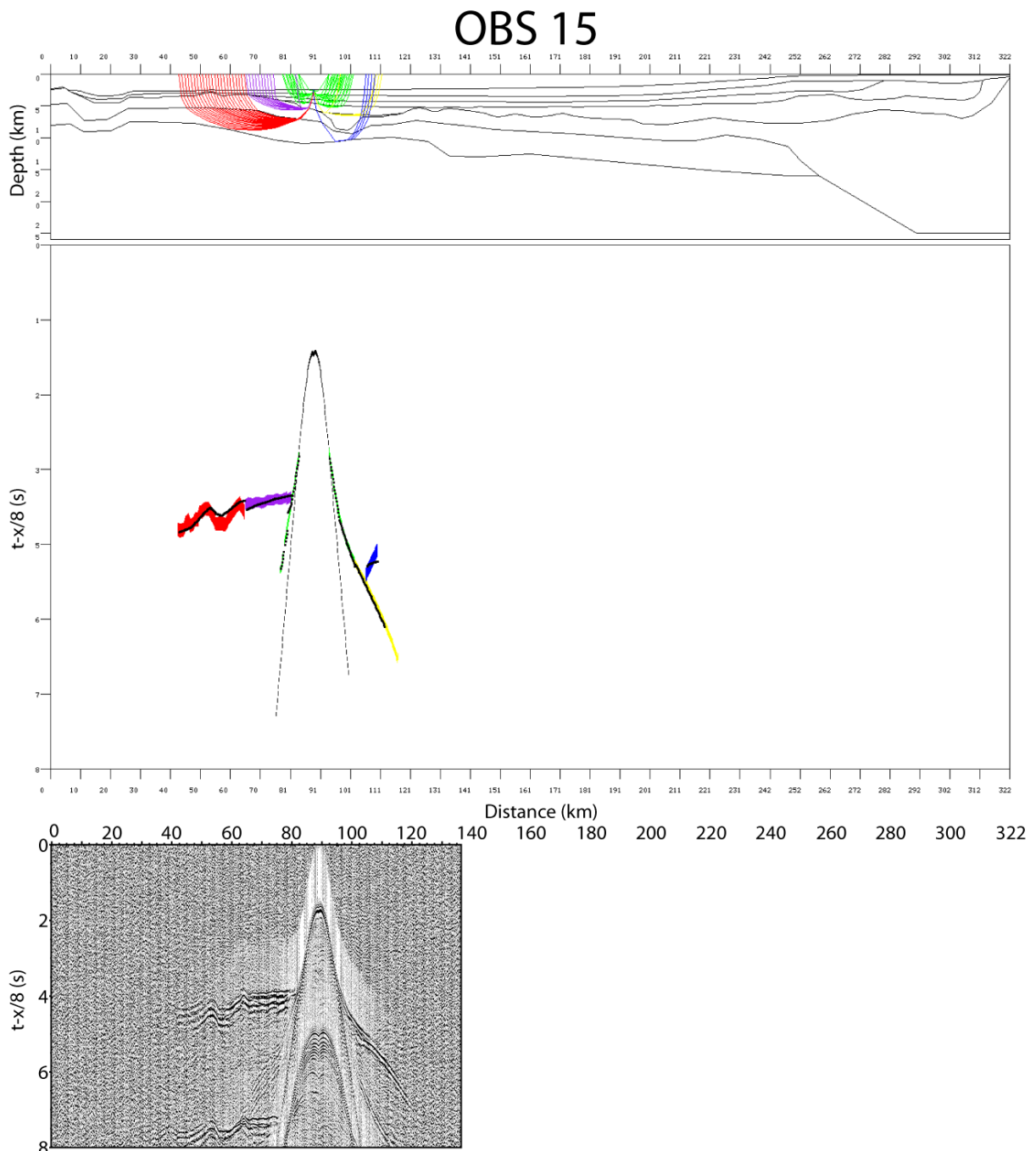
OBS 8
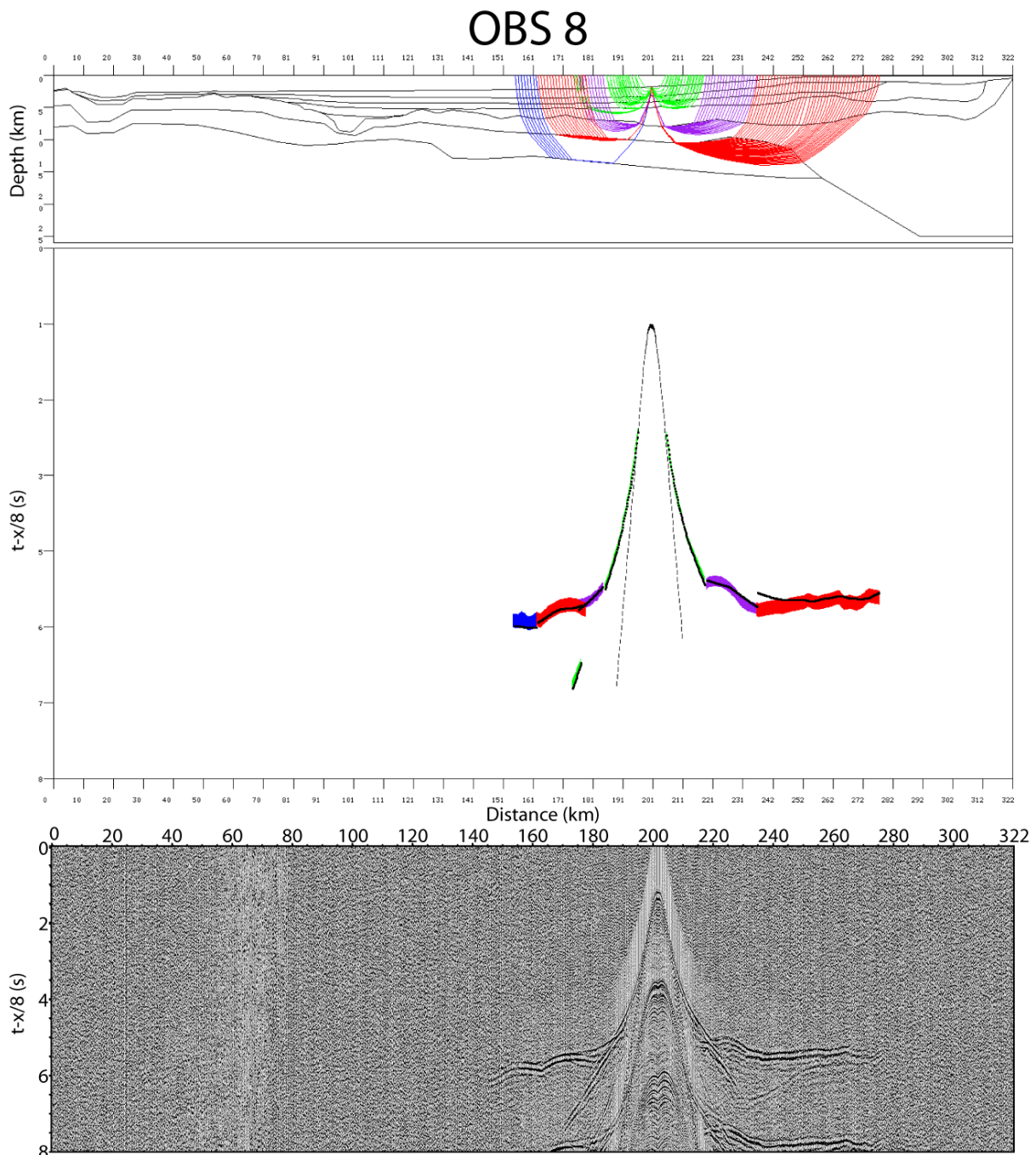
Figure A.8: Rays traced through the model (upper plot) and calculated rays (black lines) and picks (colored) from Rayinvr (middle plot), and OBS seismogram (lower plot).

Figure A.9: Rays traced through the model (upper plot) and calculated rays (black lines) and picks (colored) from Rayinvr (middle plot), and OBS seismogram (lower plot).
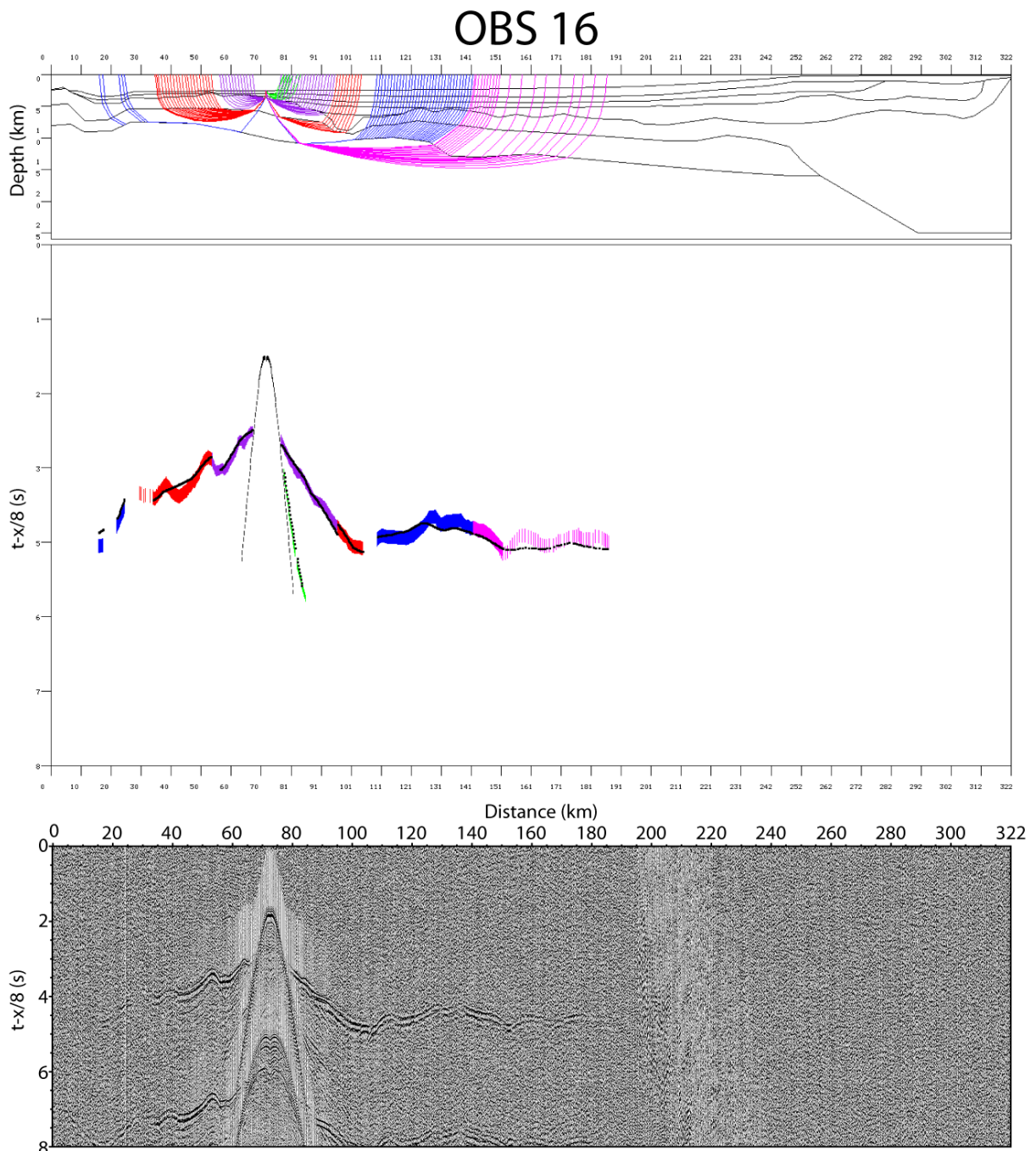
OBS 10

Figure A.10: Rays traced through the model (upper plot) and calculated rays (black lines) and picks (colored) from Rayinvr (middle plot), and OBS seismogram (lower plot).

OBS 12

Figure A.12: Rays traced through the model (upper plot) and calculated rays (black lines) and picks (colored) from Rayinvr (middle plot), and OBS seismogram (lower plot).
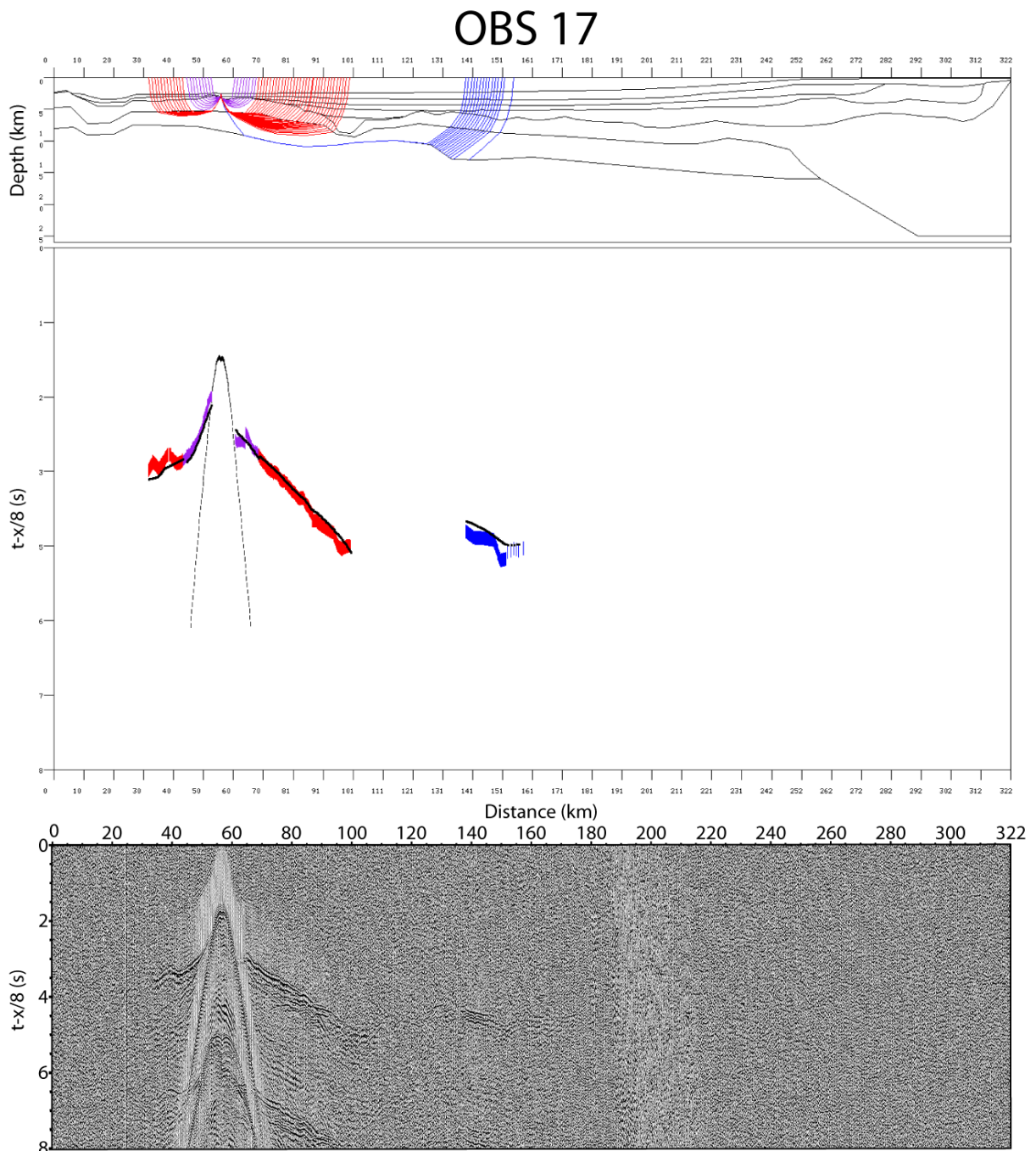
OBS 13

Figure A.13: Rays traced through the model (upper plot) and calculated rays (black lines) and picks (colored) from Rayinvr (middle plot), and OBS seismogram (lower plot).
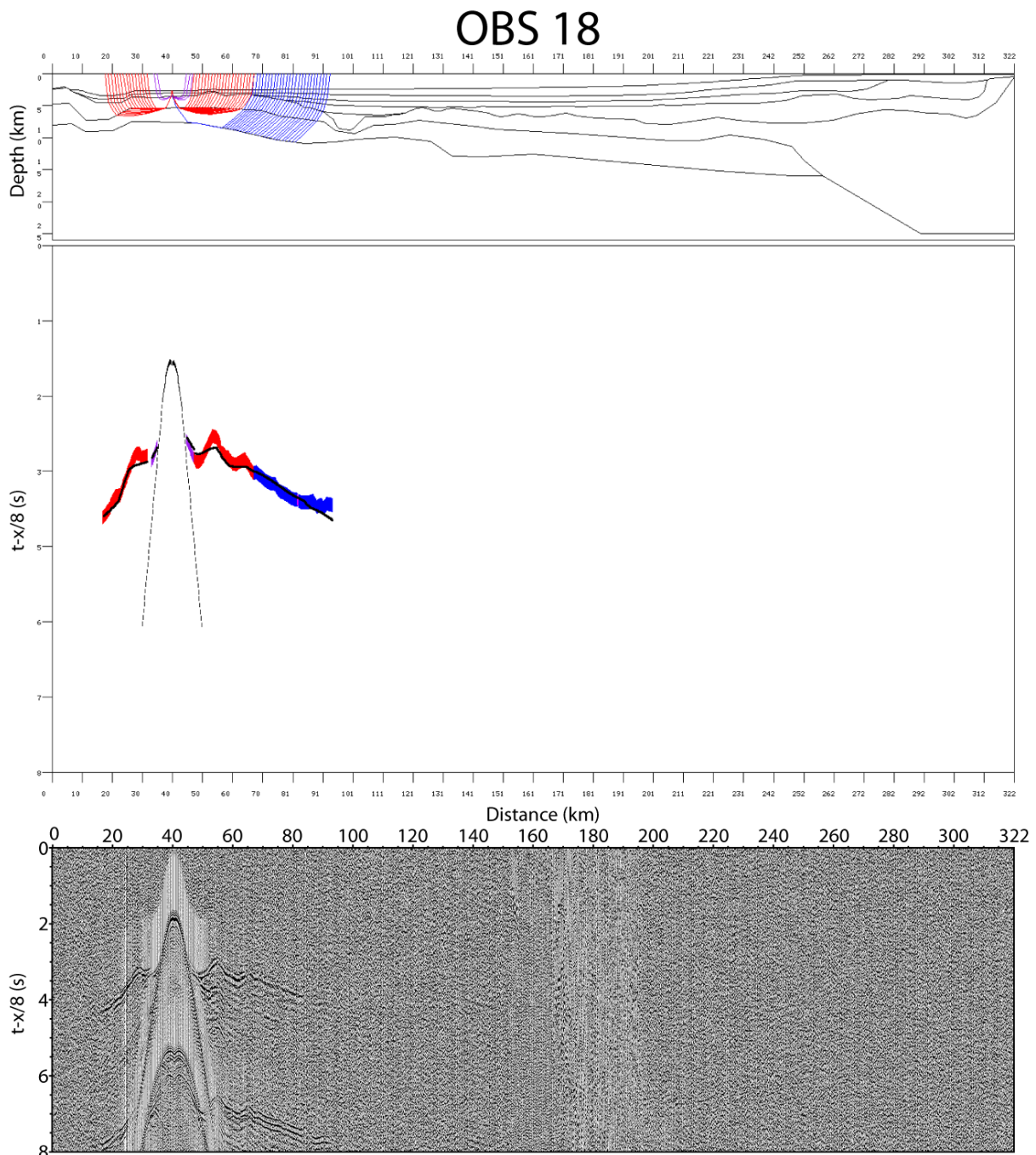
Figure A.14: Rays traced through the model (upper plot) and calculated rays (black lines) and picks (colored) from Rayinvr (middle plot), and OBS seismogram (lower plot).

OBS 15

Figure A.15: Rays traced through the model (upper plot) and calculated rays (black lines) and picks (colored) from Rayinvr (middle plot), and OBS seismogram (lower plot).

OBS 16

Figure A.16: Rays traced through the model (upper plot) and calculated rays (black lines) and picks (colored) from Rayinvr (middle plot), and OBS seismogram (lower plot).
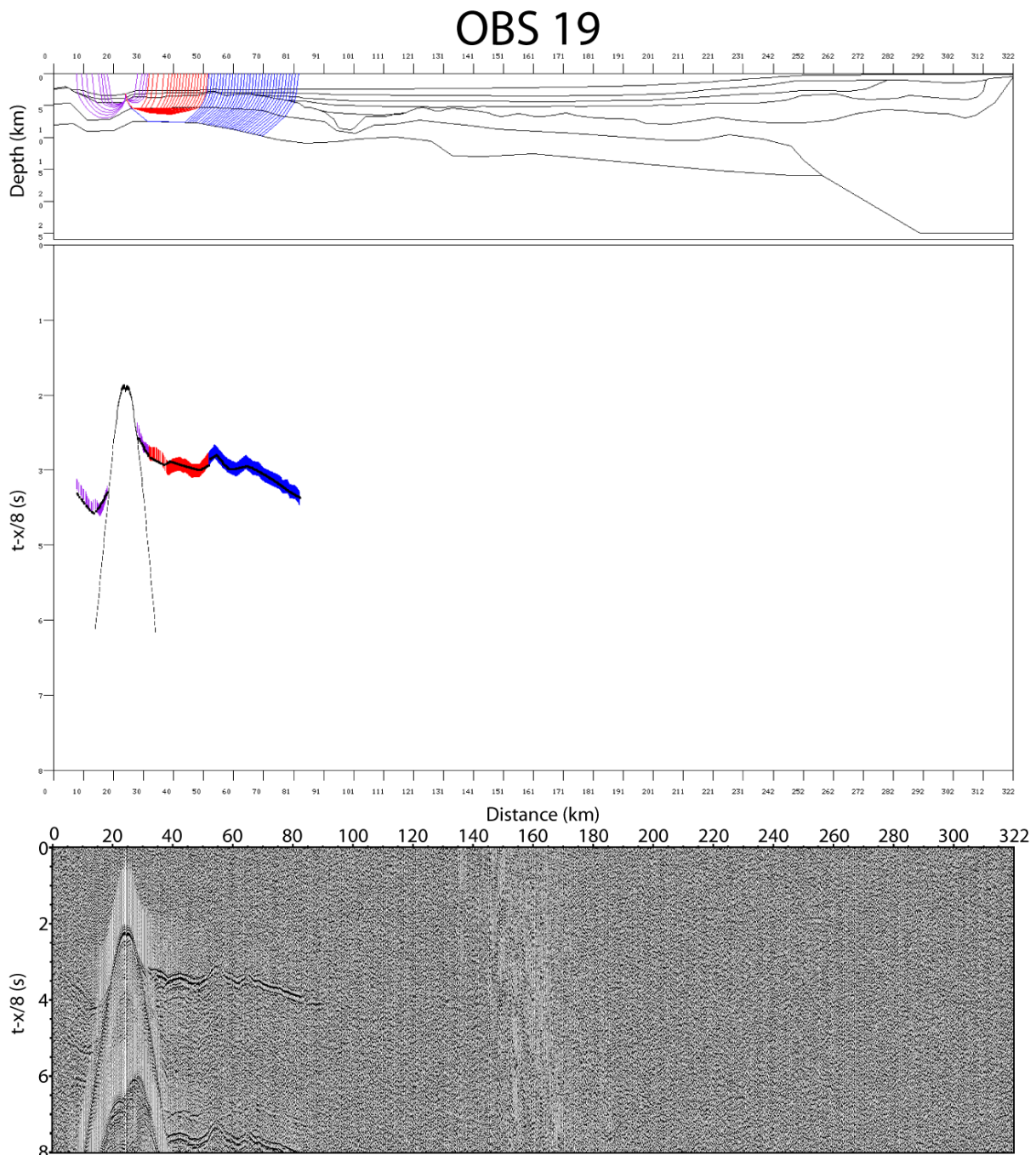
OBS 17

Figure A.17: Rays traced through the model (upper plot) and calculated rays (black lines) and picks (colored) from Rayinvr (middle plot), and OBS seismogram (lower plot).
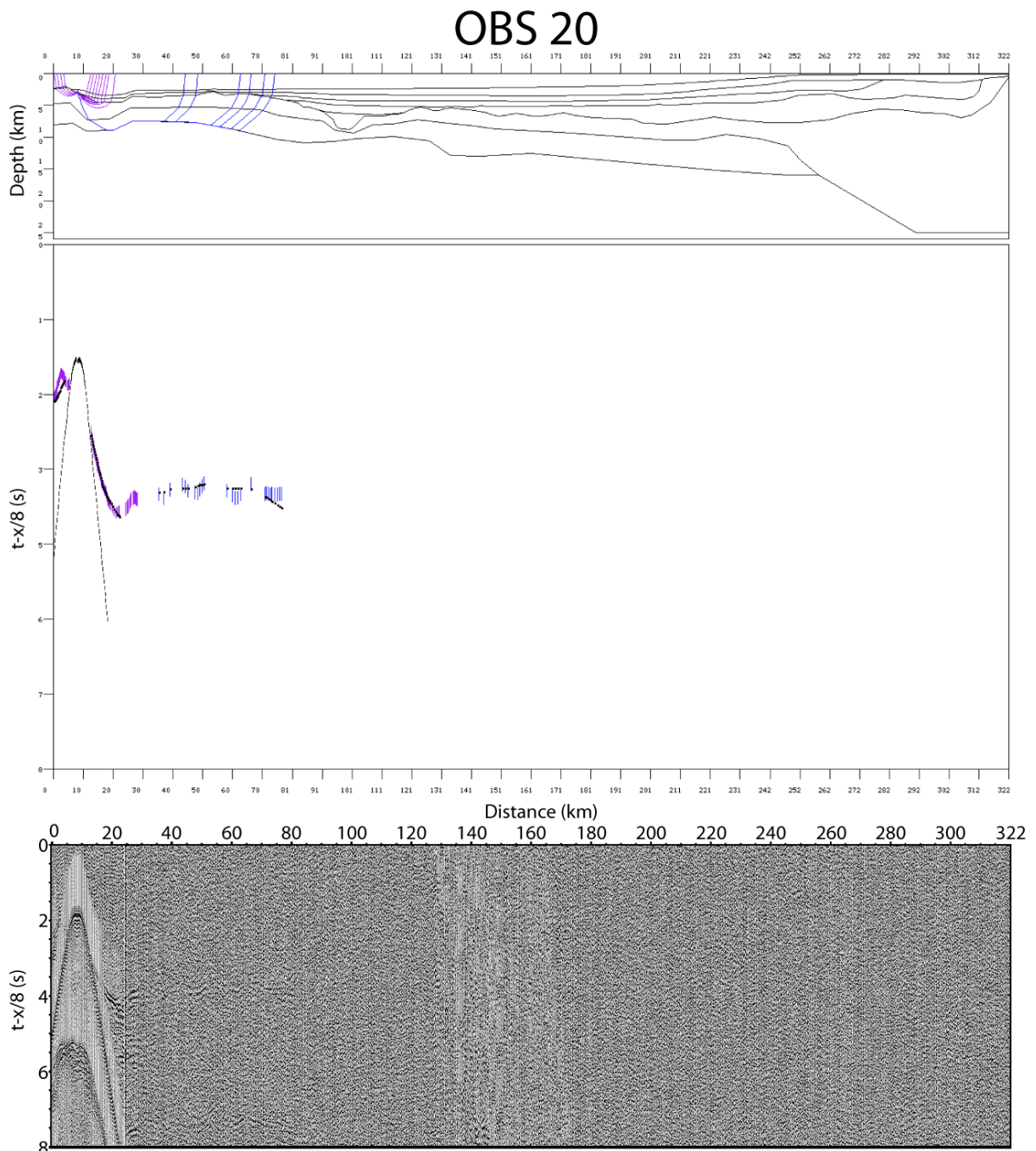
Figure A.18: Rays traced through the model (upper plot) and calculated rays (black lines) and picks (colored) from Rayinvr (middle plot), and OBS seismogram (lower plot).

OBS 19

Figure A.19: Rays traced through the model (upper plot) and calculated rays (black lines) and picks (colored) from Rayinvr (middle plot), and OBS seismogram (lower plot).

OBS 20

Figure A.20: Rays traced through the model (upper plot) and calculated rays (black lines) and picks (colored) from Rayinvr (middle plot), and OBS seismogram (lower plot).